

Title	Precise Determination of Aircraft Position and Attitude Using GPS Carrier Phase Measurement(Dissertation_全文)
Author(s)	Tsujii, Toshiaki
Citation	Kyoto University (京都大学)
Issue Date	1998-05-25
URL	http://dx.doi.org/10.11501/3138646
Right	
Type	Thesis or Dissertation
Textversion	author

**Precise Determination of Aircraft Position and Attitude
Using GPS Carrier Phase Measurement**

Toshiaki Tsujii

1998

Abstract

Precise positioning using GPS carrier phase measurement has been widely used in static applications, i.e., geodetic surveying. However, it can also be applied to the precise positioning of a moving platform if an ambiguity contained in the GPS carrier phase measurement is resolved during the motion. The technique to resolve the ambiguity on the way/fly, which is called the OTF (On-the-Fly), has been investigated by many authors. In this thesis, a new OTF algorithm is proposed and its feasibility for several kinds of applications is demonstrated.

The differential GPS positioning using carrier phase measurements is called Kinematic GPS (KGPS). We have developed our own Kinematic GPS Software, KINGS, in which the OTF is the most significant algorithm, and have evaluated its performance by conducting a lot of flight experiments using a research aircraft of the National Aerospace Laboratory (NAL). As a result, the correct ambiguity was resolved nearly instantaneously with more than 98% probability when the distance between the aircraft receiver and the ground reference receiver was less than 20km, and five or more satellites were observed. Once the ambiguity was resolved, the aircraft position was determined within 10cm (3σ).

KGPS can also be applied to determine the attitude of the platform if it has more than one antenna mounted aboard. We mounted four antennas on the aircraft to determine the aircraft pitch, roll, and yaw angle, and conducted flight experiments. Comparison between the GPS estimated attitude and inertial navigation unit (INS) attitude showed better than 0.1 degree agreements.

Acknowledgments

Special gratitude is expressed to Prof. Shin Yabushita, Applied Mathematics and Physics, Kyoto University, not only for serving as my supervising professor during all my studies, but also for professional guidance, advice, and encouragement. Thanks, also, are extended to Prof. Tohru Katayama and Prof. Norihiko Adachi for serving on the supervising committee.

I am especially grateful to Dr. Masaaki Murata, head of the planning office, National Aerospace Laboratory (NAL), Dr. Masatoshi Harigae, head of the Instrumentation section, Control Systems Division, NAL, and Dr. Masanori Okabe, former director of the Control Systems Division, NAL, for their professional guidance, advice and discussions.

Thanks are also due to Takatsugu Ono, Toshiharu Inagaki, Kazutoshi Ishikawa, and other staff members of Flight Research Division, NAL, for their warm guidance and advice during the flight experiments.

Toshiaki Tsujii
January 1998
Chofu, Tokyo

Table of Contents

Abstract	i
Acknowledgments	ii
Table of Contents	iii
List of Figures	v
List of Tables	ix
Table of Symbols	x
Abbreviations	xiv
CHAPTER 1 INTRODUCTION.....	1
CHAPTER 2 ALGORITHMS OF GPS PRECISE POSITIONING AND ATTITUDE DETERMINATION	7
2.1 Observation Equation.....	7
2.1.1 Pseudorange	7
2.1.2 Carrier Phase	13
2.1.3 Double Difference	15
2.1.4 Linear Combinations of GPS Measurements	17
2.2 Ambiguity Resolution On-the-Fly.....	19
2.3 Cycle Slip Detection.....	28
2.4 Positioning Algorithm.....	30
2.4.1 Least Squares Method	30
2.4.2 Extended Kalman Filter	32
2.5 Attitude Determination Algorithm.....	36
2.5.1 Attitude Determination.....	37
2.5.2 Structural Flexure Modeling	39
2.5.3 Least Squares Adjustment.....	39
2.5.4 Comparison with INS Attitude.....	43
CHAPTER 3 EVALUATION OF POSITIONING ACCURACY	45
3.1 Evaluation of Positioning Accuracy Using Static Data.....	45
3.1.1 Comparison with Static Positioning Solutions.....	45
3.1.2 Error Sources.....	52
3.1.3 Positioning Accuracy Dependent on Baseline length	68

3.2 OTF Limit in Baseline Length	74
3.3 Detection of Crustal Movement due to an Earthquake	76
CHAPTER 4 FLIGHT TESTS AND RESULTS	79
4.1 KGPS Positioning accuracy of aircraft in flight.....	79
4.1.1 Flight Test Configuration	80
4.1.2 GPS-Estimated Flight Trajectory	80
4.1.3 Comparison with Laser Tracked Trajectory.....	91
4.1.4 Comparison with DGPS/INS Trajectory	93
4.2 Evaluation of the OTF algorithm	96
4.3 Attitude Determination.....	107
4.3.1 Flight Test Configuration	107
4.3.2 GPS-Estimated Attitude	110
4.3.3 Comparison with INS Attitude.....	113
4.3.4 Structural Flexure.....	116
CHAPTER 5 SUMMARY AND CONCLUSIONS	121
5.1 Summary	121
5.2 Conclusions and Future Prospects.....	123
References	125
Vita	

List of Figures

Fig.1-1	Search cube in ambiguity space	3
Fig.1-2	Changes of positions calculated using the ambiguity candidates in search cube	3
Fig.2-1	GPS satellite	8
Fig.2-2	Structure of the GPS satellite signal.....	9
Fig.2-3	Horizontal positioning accuracy for SPS and PPS users.....	10
Fig.2-4	Single difference of GPS measurement.....	16
Fig.2-5	Double difference of GPS measurement	16
Fig.2-6	Flowchart of the OTF algorithm	21
Fig.2-7	Relationship among the correct ambiguity, initial estimate of ambiguity, and its error.....	24
Fig.2-8	Aircraft body frame defined by four GPS antennas	38
Fig.2-9	Structural flexure modeling.....	40
Fig.3-1	Map of Izu-Islands area	46
Fig.3-2a	KGPS positioning errors when ionospheric-free observable was used (Miyakeizu - Miyaketsubota, 7.951km)	48
Fig.3-2b	Errors of ionospheric-free KGPS solution (Niijima - Kozujima, 22.146km).....	48
Fig.3-2c	Errors of ionospheric-free KGPS solution (Miyakeizu - Kozujima, 35.182km).....	49
Fig.3-2d	Errors of ionospheric-free KGPS solution (Miyaketsubota - Kozujima, 41.173km)	49
Fig.3-2e	Errors of ionospheric-free KGPS solution (Minamiizu - Kozujima, 56.695km)	50
Fig.3-2f	Errors of ionospheric-free KGPS solution (Minamiizu - Miyakeizu, 84.029km)	50
Fig.3-3	Variation of RHDOP and RVDOP.....	51
Fig.3-4	Position error caused by estimation error of zenith delay	51
Fig.3-5	Horizontal and Vertical position errors assuming that the zenith delay for reference site is correct and that of estimation site contains 1, 2, 3, and 4cm errors.....	54

Fig.3-6	RMSs of the double differenced ionospheric errors for various baseline lengths	54
Fig.3-7a	Horizontal and vertical position error caused by ionospheric delay (Miyakeizu – Miyaketsubota, 7.951km)	55
Fig.3-7b	Horizontal and vertical position error caused by ionospheric delay (Niijima - Kozujima, 22.146km).....	55
Fig.3-7c	Horizontal and vertical position error caused by ionospheric delay (Miyakeizu – Kozujima, 35.182km)	56
Fig.3-7d	Horizontal and vertical position error caused by ionospheric delay (Miyaketsubota - Kozujima, 41.173km)	56
Fig.3-7e	Horizontal and vertical position error caused by ionospheric delay (Minamiizu – Kozujima, 56.695km).....	57
Fig.3-7f	Horizontal and vertical position error caused by ionospheric delay (Minamiizu – Miyakeizu, 84.029km).....	57
Fig.3-8	RMSs of the horizontal and vertical position errors caused by ionospheric delay	58
Fig.3-9a	Multipath errors on L1 carrier phase for various damping factors.....	61
Fig.3-9b	Multipath errors on L2 carrier phase for various damping factors.....	61
Fig.3-10	Amplitude of superposed signal for the damping factor same with Fig.3-9	62
Fig.3-11a	Multipath errors on widelane observable	62
Fig.3-11b	Multipath errors on narrowlane observable.....	63
Fig.3-11c	Multipath errors on ionospheric-free observable	63
Fig.3-12	Differences between broadcast and precise ephemeris	65
Fig.3-13	Time variation of double difference of the orbit difference (Baseline No.1-8)	65
Fig.3-14	RMSs of the double differenced orbit errors depending on the baseline length.....	65
Fig.3-15	Position error caused by broadcast ephemeris error (Baseline No.1-8)	66
Fig.3-16	RMSs of the horizontal and vertical position errors caused by broadcast ephemeris error (Baseline No.1-8)	66
Fig.3-17a	RMSs of the horizontal and vertical position errors when ionospheric-free observable was used (Baseline No. 1-6).....	69
Fig.3-17b	RMSs of the horizontal and vertical position errors when L1 carrier observable was used (Baseline No. 1-6).....	69
Fig.3-17c	RMSs of the horizontal and vertical position errors when narrowlane observable was used (Baseline No. 1-6).....	70

Fig.3-17d	RMSs of the horizontal and vertical position errors when widelane observable was used (Baseline No. 1-6).....	70
Fig.3-18a	Position error in the baseline Miyakeizu - Kozujima (35.182km) when L1 carrier observable is used	72
Fig.3-18b	Position error in the baseline Miyakeizu - Kozujima (35.182km) when narrowlane observable is used	72
Fig.3-18c	Position error in the baseline Miyakeizu - Kozujima (35.182km) when widelane observable is used.....	73
Fig.3-19a	Position of Kozujima estimated by kinematic GPS before and after an earthquake (Niijima - Kozujima, 22.146km)	77
Fig.3-19b	Position of Kozujima estimated by kinematic GPS before and after an earthquake (Miyakeizu - Kozujima, 35.182km).....	77
Fig.3-19c	Position of Kozujima estimated by kinematic GPS before and after an earthquake (Miyaketsubota - Kozujima, 41.173km).....	78
Fig.3-19d	Position of Kozujima estimated by kinematic GPS before and after an earthquake (Minamiizu - Kozujima, 56.695km).....	78
Fig.4-1	Research aircraft Do-228 and the laser tracker	81
Fig.4-2	Ground monitor site, on which a Trimble Geodetic L1/L2 antenna was mounted, and the antenna of transmitter	82
Fig.4-3	GPS receiver and the transmitter installed in the monitor site	82
Fig.4-4	Dual frequency GPS antenna mounted on the roof of Do-228.....	83
Fig.4-5	Flight test configuration and the RCS coordinate system	84
Fig.4-6	Horizontal trajectory of the aircraft.....	86
Fig.4-7	Height profile of the aircraft.....	86
Fig.4-8	Measurement residuals of primary satellites for case 2.....	88
Fig.4-9	Position differences (Case1 – Case 2) in RCS coordinate	89
Fig.4-10	Measurement residuals with the tropospheric delay modeling	89
Fig.4-11	Position difference with/without tropospheric delay modeling.....	90
Fig.4-12	Position difference between case 3 and 4.....	90
Fig.4-13	Laser reflector mounted under the nose of Do-228.....	92
Fig.4-14	Difference between the laser and KGPS trajectory of the Do-228.....	92
Fig.4-15	Position difference between the DGPS/INS and KGPS.....	95
Fig.4-16	Velocity difference between the DGPS/INS and KGPS	95
Fig.4-17	Horizontal trajectory of the aircraft.....	97
Fig.4-18	Height profile of the aircraft.....	98
Fig.4-19	Separation between the reference receiver and the aircraft.....	98

Fig.4-20	Number of satellites observed during the flight test.....	99
Fig.4-21	Variation of RDOP during the flight test	99
Fig.4-22	Elevations of observed satellites	100
Fig.4-23	(Sum of squared residuals / degree of freedom) of each L1 phase ambiguity candidate.....	102
Fig.4-24	Residuals of double differenced L1 phase measurement with correct ambiguities (PRN16-6, 16-24, 16-26, 16-27).....	105
Fig.4-25	Residuals of double differenced L1 phase measurement with incorrect ambiguities (PRN16-6, 16-24, 16-26, 16-27).....	105
Fig.4-26	Horizontal position of the receiver using smoothed pseudorange, widelane ambiguity candidates, and L1 phase ambiguity candidates.....	106
Fig.4-27	Difference between the position calculated using the correct widelane ambiguity and those using each candidate of L1 phase ambiguity.....	106
Fig.4-28	GPS L1 antennas mounted on the fuselage	108
Fig.4-29	Left wing antenna	108
Fig.4-30	Block diagram of the experimental system	109
Fig.4-31	Flight trajectory during the experiment of attitude determination	109
Fig.4-32	Residuals of three antenna baseline lengths during the flight	111
Fig.4-33	GPS-estimated attitude of the aircraft	111
Fig.4-34	GPS-estimated flexures of wing and fuselage.....	112
Fig.4-35	Difference between GPS and INS attitude angles	114
Fig.4-36	GPS estimated attitude and flexure	115
Fig.4-37	Change of yaw angle and the corresponding lateral flexure of fuselage during the yaw reversals.....	117
Fig.4-38	Root-Sum-Squares (RSS) of residuals in the estimation process for Case 1 and Case 2	117
Fig.4-39	Pitch, pitch rate, and the corresponding wing flexure when the aircraft pitch is held at 0, 5, -5, 10, 15 degrees	118
Fig.4-40	Change of wing flexure, pitch, and pitch rate during pitch reversals.....	118
Fig.4-41	Change of wing flexure, roll, and roll rate during roll reversals	119

List of Tables

Table 2-1	GPS satellite signals	9
Table 2-2	Summary of measurement errors and corresponding position errors.....	19
Table 2-3	Body frame coordinates of antenna vectors	38
Table 3-1	Summary of baselines and their lengths	46
Table 3-2	Summary of multipath for various observable against the dumping factor ..	60
Table 3-3	Kinematic GPS error budget	67
Table 3-4	Relative effect of GPS error sources on various observables.....	67
Table 3-5	Accuracy of horizontal and vertical position estimated by KGPS (RMS) ...	68
Table 3-6	Limit of the ambiguity resolution on-the-fly in baseline length.....	75
Table 4-1	Models for the carrier phase observable.....	85
Table 4-2	Differences between KGPS and laser trajectory when the distance was shorter than 3 km.....	93
Table 4-3a	Summary of widelane OTF using the test in measurement domain only...	101
Table 4-3b	Summary of L1 OTF using the test in measurement domain only.....	101
Table 4-4a	Summary of widelane OTF using the tests in both measurement and positioning domains	101
Table 4-4b	Summary of L1 OTF using the tests in both measurement and positioning domains	101
Table 4-5	Summary of attitude difference between GPS and INS	114

Table of Symbols

PR	pseudorange	DD_i	double differenced observable between the first and (i+1)-th satellite
ϕ	carrier phase	ρ_u^{*i}	distance from user receiver to i-th satellite
c	light speed	σ_m	double differenced measurement error
t, t_{SV}	time of signal reception by the receiver, and the signal transmitting time from the satellite	σ_p	double differenced positioning error
T, T_{SV}	the reception and transmission time in GPS time	C	measurement error covariance matrix (for double difference)
$\mathbf{R}, \mathbf{R}_{SV}$	position of receiver and satellite in the inertial space	C_{PR}	measurement error covariance matrix of smoothed pseudorange
$\mathbf{r}, \mathbf{r}_{SV}$	position of receiver and satellite in WGS 84	C_W	measurement error covariance matrix of widelane
\mathbf{r}_{SV}^*	the satellite position calculated using the adopted ephemeris	C_N^W	covariance matrix of initially estimated widelane ambiguity
ρ	geometrical distance from the receiver to the satellite	C_N^{L1}	covariance matrix of initially estimated L1 ambiguity
ρ^*	geometrical distance calculated using the adopted ephemeris	σ_N^W	standard deviation of the initial estimate of double differenced widelane ambiguity
b, b_{SV}	clock bias of receiver and satellite	σ_N^{L1}	standard deviation of the initial estimate of double differenced L1 ambiguity
d_{ion}	ionospheric propagation delay (for L1 pseudorange)	σ_m^{PR}	standard deviation of double differenced smoothed pseudorange measurement error
d_{trop}	tropospheric propagation delay	σ_m^W	standard deviation of double differenced widelane measurement error
d_{sag}	sagnac effect	σ_m^{L1}	standard deviation of double differenced L1 carrier measurement error
d_{eph}	ephemeris error	$\sigma_p^{PR}, \sigma_H^{PR}, \sigma_v^{PR}$	standard deviation of 3-dimensional, horizontal, and vertical positioning error when using the smoothed pseudorange
I	parameter concerning the ionospheric delay	$\sigma_p^W, \sigma_H^W, \sigma_v^W$	standard deviation of 3-dimensional, horizontal, and vertical positioning error when using the widelane
d_m	multipath error	$\sigma_p^{L1}, \sigma_H^{L1}, \sigma_v^{L1}$	standard deviation of 3-dimensional, horizontal, and vertical positioning error when using the L1 carrier
$d_{m,phase}$	multipath error of carrier phase	σ_H^{PR-W}	standard deviation of the difference between the pseudorange-position and widelane-position in horizontal direction
N	integer ambiguity	σ_H^{W-L1}	standard deviation of the difference between the widelane - position and L1-position in horizontal direction
ϵ	measurement noise of carrier phase	σ_H^{PR-L1}	standard deviation of the difference between the pseudorange - position and L1-position in horizontal direction
ϵ_{PR}	measurement noise of pseudorange	$\mathbf{r}^{PR}, \mathbf{r}^W, \mathbf{r}^{L1}$	position calculated using smoothed pseudorange, widelane, and L1 carrier
f	frequency of carrier phase	$SLIP$	index for the detection of cycle slip
λ	wavelength of carrier phase		
Δ	operator to take single difference of observable		
$\nabla\Delta$	operator to take double difference of observable		
H	measurement matrix		

\mathbf{y}	measurement vector	$\bar{\mathbf{x}}_a$	a priori state vector
$\bar{\mathbf{y}}$	computed measurement vector	$\bar{\mathbf{y}}_a$	computed measurement vector
$\bar{\mathbf{r}}$	a priori position of the receiver	$\delta\mathbf{y}_a$	residual vector
$\delta\mathbf{y}$	measurement residual vector	H_a	measurement matrix for the attitude determination
\mathbf{e}	measurement error vector	$\overline{\nabla\Delta I}$	estimate of the double differenced ionospheric parameter
J	cost function	$\delta h_{ion,wide}$	estimate of horizontal positioning error due to the ionospheric delay when the widelane is used
$\delta\hat{\mathbf{r}}$	weighted least squares estimate of the receiver position correction	$\delta v_{ion,wide}$	estimate of vertical positioning error due to the ionospheric delay when the widelane is used
\mathbf{x}	state vector in the Kalman filter	A_D, A_R	amplitude of direct and reflected signals
$\mathbf{r}, \mathbf{v}, \mathbf{a}$	position, velocity and acceleration of the receiver in WGS84	φ_D	phase of direct signal
τ, \mathbf{u}	time constant and white noise in a Gauss-Markov process	φ	phase shift of reflected signal
F, B, Q	system dynamics matrix, driving matrix, and process noise matrix in the continuous Kalman filter	Θ	multipath error
Φ, G, Q'	system transition matrix, driving matrix, and process noise matrix in the discrete Kalman filter	α	damping factor of the reflection
\mathbf{r}_j^B	antenna vector of j-th antenna in the body frame	$\overline{\nabla\Delta d}_{eph}$	estimate of double differenced broadcast ephemeris error
\mathbf{r}_j^L	antenna vector of j-th antenna in the local level frame	δh_{eph}	estimate of horizontal positioning error due to the broadcast ephemeris error
\mathbf{r}^B	antenna vector matrix in the body frame	δv_{eph}	estimate of vertical positioning error due to the broadcast ephemeris error
\mathbf{r}^{B0}	antenna vector matrix in the body frame without the structural flexure	l	baseline length
\mathbf{r}^L	antenna vector matrix in the local level frame		
\mathbf{r}^I	antenna vector matrix in the INS frame		
R_L^B	rotation matrix from the local level to the body frame		
R_L^I	rotation matrix from the local level to the INS frame		
R_I^B	rotation matrix from the INS to the body frame		
R_I^L	rotation matrix from the INS to the local level frame		
φ, θ, ψ	roll, pitch, and yaw angle		
$\varphi_I, \theta_I, \psi_I$	attitude angles measured by the INS		
$\varphi_I', \theta_I', \psi_I'$	calibrated INS attitude		
\mathbf{x}_a	state vector for the attitude determination		
\mathbf{y}_a	measurement vector for the attitude determination		

Abbreviations

A/L	Approach and Landing
A-S	Anti-Spoofing
C/A-code	Coarse/Acquisition-code
CEP	Circular Error Probable
DGPS	Differential GPS
DME	Distance Measurement Equipment
DoD	Department of Defense
DRMS	Distance Root Mean Square
ECEF	Earth Centered Earth Fixed
ENRI	Electric Navigation Research Institute
FDAS	Flight Data Acquisition System
GPS	Global Positioning system
INS	Inertial Navigation System
KGPS	Kinematic GPS
MLS	Microwave Landing System
NAL	National Aerospace Laboratory
OTF	On the Fly
P-code	Precise-code
PPS	Precise Positioning Service
PRN	Pseudo Random Noise
RCS	Runway Coordinate System
RDOP	Relative Dilution of Precision
SA	Selective Availability
SPS	Standard Positioning Service
VLBI	Very Long Baseline Interferometry
WGS84	World Geodetic System 1984

Chapter 1

Introduction

The NAVSTAR GPS (NAVigation System with Time and Ranging Global Positioning System) is a satellite-based radio navigation system providing precise position and time information. At present (Apr. 1997), 26 satellites are operating, and usually 4 to 9 satellites can be observed from any spot on earth at one time. Moreover, it has the advantage of independence from meteorological conditions. Thus, GPS civil users have been rapidly increasing with the spread of low cost GPS receivers. GPS is most commonly used for navigation of all kinds of vehicle such as cars, ships, and aircraft. The accuracy is approximately 100m horizontally, and 150m vertically (3σ) if the GPS receiver is used stand alone. However, if GPS measurements from one or more reference receivers are used, the accuracy will be 2-5 m horizontally and 4-10m vertically, although it depends on the hardware and other conditions (See Chapter 2.1.1). This technique is called differential GPS (DGPS). In the stand-alone GPS and DGPS navigation, the code phase measurement is used. Code phase, which is commonly called pseudorange, is an unambiguous range between satellite and receiver with precision of from some tens of centimeters to a few meters depending on the hardware. We evaluated the performance of DGPS for aircraft or spacecraft positioning using real flight data (Tsuji et. al., 1992, 1993b, 1995a; Harigae et. al., 1996; Matsumoto et. al., 1996; Murata et. al., 1996).

On the other hand, one can measure carrier phase in addition to the code phase by receiving the transmitted navigation satellite signal. Carrier phase is an ambiguous range with precision of several millimeters. Carrier phase after ambiguities are resolved is

called carrier range. The use of carrier range enables us to conduct highly precise positioning. This ability has already been demonstrated in surveying, and today this technique is known as interferometric surveying after Very Long Baseline Interferometry (VLBI). In interferometric surveying, the ambiguity in carrier phase is resolved in batch process using the whole measurement data at once. Two major methods of ambiguity resolution have been investigated, i.e., the least squares searching method (Hatch 1991), and the ambiguity function method (Remondi, 1991). However, these methods were proved to be equivalent (Lachapelle, et. al., 1992a). In the search algorithm, the initial vector between the user and reference receiver is determined first, and then the carrier phase ambiguities are determined by choosing the best fit to the measurements from a number of candidates. Fig.1-1 shows the so-called search cube in the ambiguity space (see Chapter 2.2). In the static survey, the ambiguity is resolved by making use of the change of satellite constellation with time. Fig.1-2 shows the changes of positions corresponding to each ambiguity candidate according to the change of satellite constellation. Since the position solution corresponding to the correct ambiguity does not change with time, the ambiguity will be resolved after a considerable change of satellite constellation. Therefore, it is necessary to record the GPS measurement data until the constellation changes sufficiently. The time required for the resolution depends on the baseline length or other environmental conditions such as the ionospheric disturbance and multiple propagation effect. Typically, 15 to 30 minutes are necessary for 10km or shorter baselines while several hours are necessary for a few hundred baselines (Seeber 1993).

In addition to the geodetic survey, the precise (centimeter-level accuracy) carrier phase positioning has a wide area of application in aerospace technology such as precision approach, taxi guidance, and rendezvous docking. The carrier phase positioning of moving platforms with one or more reference GPS receivers is called Kinematic GPS (KGPS). Since the ambiguity is integer constant as long as the receiver maintains the lock of satellites, one can obtain the carrier range after the initial ambiguity resolution. Therefore, if the ambiguity is resolved by batch process in static mode before moving, which is called “static initialization”, the KGPS can be conducted until the receiver tracks four or more satellites continuously (Talbot, 1991).

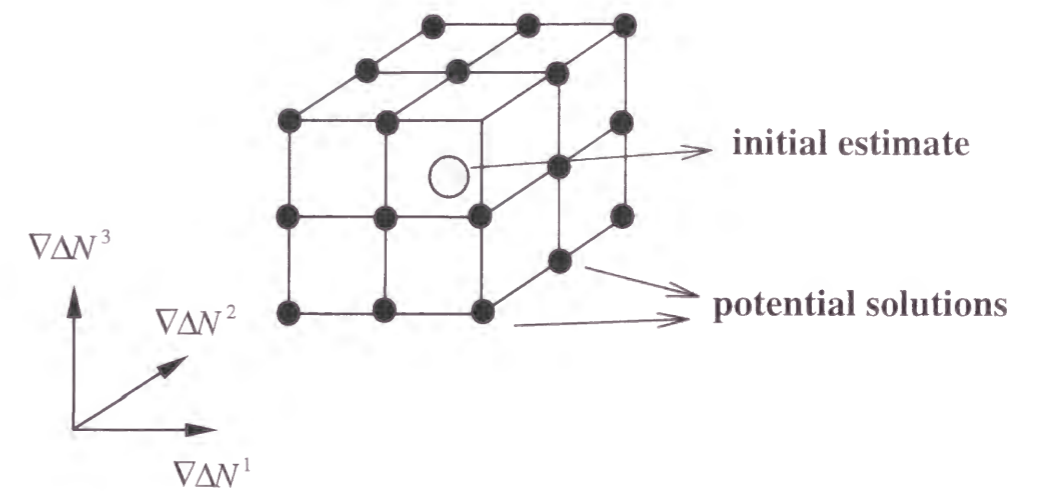


Fig.1-1 Search cube in ambiguity space

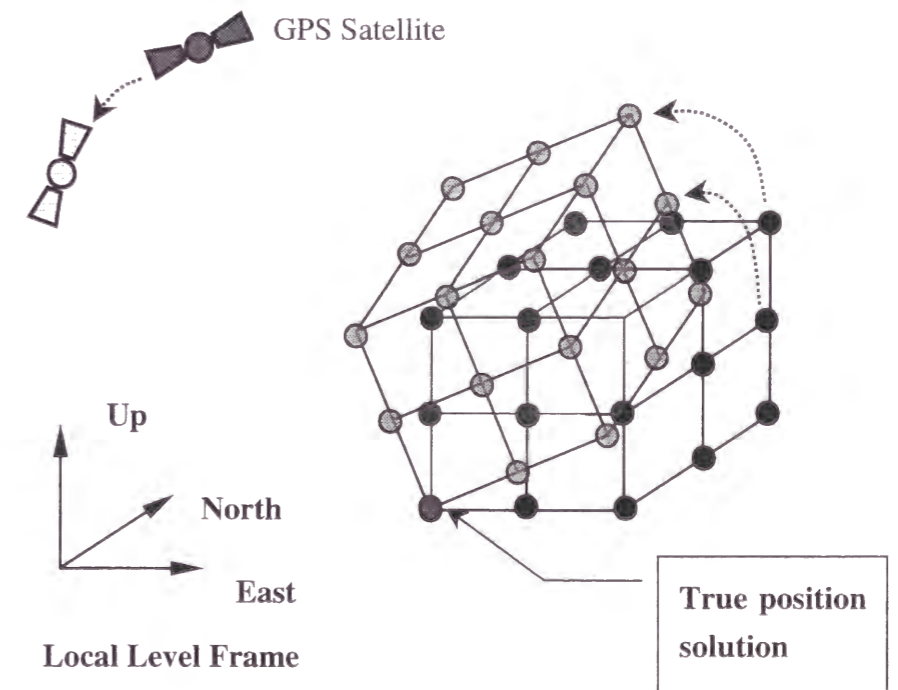


Fig.1-2 Changes of positions calculated using the ambiguity candidates in search cube

However, if some losses of locks (cycle slip) occur, or some satellites go out of sight, we cannot continue to perform the KGPS. So, in these applications the ambiguity resolution “on-the-fly” (OTF), i.e., without static initialization, is the key factor for precise positioning. A lot of authors have been investigating the OTF algorithm.

On the other hand, other kinds of positioning algorithms that make use of the carrier phase have been developed. For example, some authors treat the ambiguity as the real number and estimate the position by the Kalman filter, which is the so-called “Floating solution” (Ford, 1994), while the ambiguity is fixed as an integer in the OTF and the estimated solution is called “Fixed Solution”. However, its positioning accuracy (< 20cm) is inferior to the fixed solution by the OTF. Kleusberg (1986) developed a robust algorithm combining the pseudorange and the carrier doppler in which the integer ambiguity was not resolved. The positioning accuracy was better than one meter, which was similar to the carrier smoothed solution. Nowadays, the fixed solution by the OTF is the most accurate kinematic solution.

When the P-code (Precision code, see Chapter 2.1.1) measurement was available and the baseline length was a few kilometers, the ambiguities in two frequencies were resolved by the so-called “extra-widelaning” (Seeber and Wübbena, 1989). However, once the A-S (Anti-Spoofing, see Chapter 2.1.1) was active, the searching method was applied more or less to the entire OTF algorithm. Most of the proposed OTF algorithms adopt the root sum squares as a statistical criterion in the search algorithm (Hofmann-Wellenhof, 1992; Lachapelle, et. al., 1992a, 1992b; Hatch, 1994). This is called “test in the measurement domain”. On the other hand, another kind of criteria can be used, i.e., the position difference between the pseudorange-position (position solution estimated by using the pseudorange) and the position calculated by using each ambiguity candidate. This is called “test in the positioning domain”. Abidin et. al. (1991) proposed an OTF algorithm which adopted both criteria, and he considered the three dimensional position in the positioning domain test. However, the vertical positioning accuracy is generally worse than the horizontal accuracy, and is affected by some error sources, especially ionospheric propagation delay. Therefore, we propose to use the horizontal position difference as a criterion in the positioning domain test. This method is very effective for dual frequency GPS receivers.

If the ambiguity can be resolved by the proposed OTF algorithm, several kinds of real time applications will be possible, such as precision navigation of vehicles and monitoring crustal movement during earthquakes. The attitude determination is also a probable application, in which more than one antenna are necessary onboard, but no ground reference receiver is required. Moreover, if we mounted some GPS antennas on a non-rigid platform, such as a space station, we could estimate not only its attitude but also the structural flexures. The objective of this thesis is to evaluate the performance of the proposed OTF algorithm by flight experiments and to test the feasibility of its applications, i.e., aircraft precise positioning and attitude determination. In chapter 2, the OTF algorithm and attitude determination algorithms are described in detail. In chapter 3, the accuracy of carrier phase positioning is evaluated by analyzing static survey data in the Izu-Islands area. In order to estimate the dependence of accuracy on the distance between stations (baseline length), seven different baselines are used for analyses. Moreover, we estimate the limit baseline length at which the OTF performs successfully. Finally in that chapter, we demonstrate that crustal movement of a few centimeters during an earthquake can be detected by KGPS. In chapter 4, flight test configurations of KGPS and attitude determination are described and analytical results are reported. In these experiments, we used a research aircraft, Dornier 228-200 (Do-228), which belongs to the National Aerospace Laboratory (NAL) of Japan. Finally we conclude this study and describe some future works.

Chapter 2

Algorithms of GPS Precise Positioning and Attitude Determination

In this chapter, the explicit forms of GPS observation equations are shown firstly, and the OTF algorithm is given next. Then the methods of cycle slip detection are described. And finally, the algorithms of KGPS positioning and the attitude determination are shown, in which the OTF plays the most significant role. The analytical results using the real experimental data will be shown in Chapters 3 and 4.

2.1 Observation Equation

2.1.1 Pseudorange

The GPS satellite (Fig.2-1) transmits microwave signals in two frequencies, i.e., L1 (1575.42MHz) and L2 (1227.60MHz). The L1 carrier phase is modulated by two kinds of Pseudo Random Noise (PRN), which are called Coarse/Acquisition (C/A) code and Precision (P) code, while the L2 carrier phase is modulated by P code. The L1 carrier phase is also modulated by the navigation message that contains the satellite orbit parameter (broadcast ephemeris). The main features of all three signals are given in Table 2-1, and Fig.2-2 shows how code and carrier are combined.

Since GPS is a military navigation system under primary responsibility of the U.S. Department of Defense (DoD), only limited access to the total system accuracy would be available to the civil user community. The service available to the civil community is

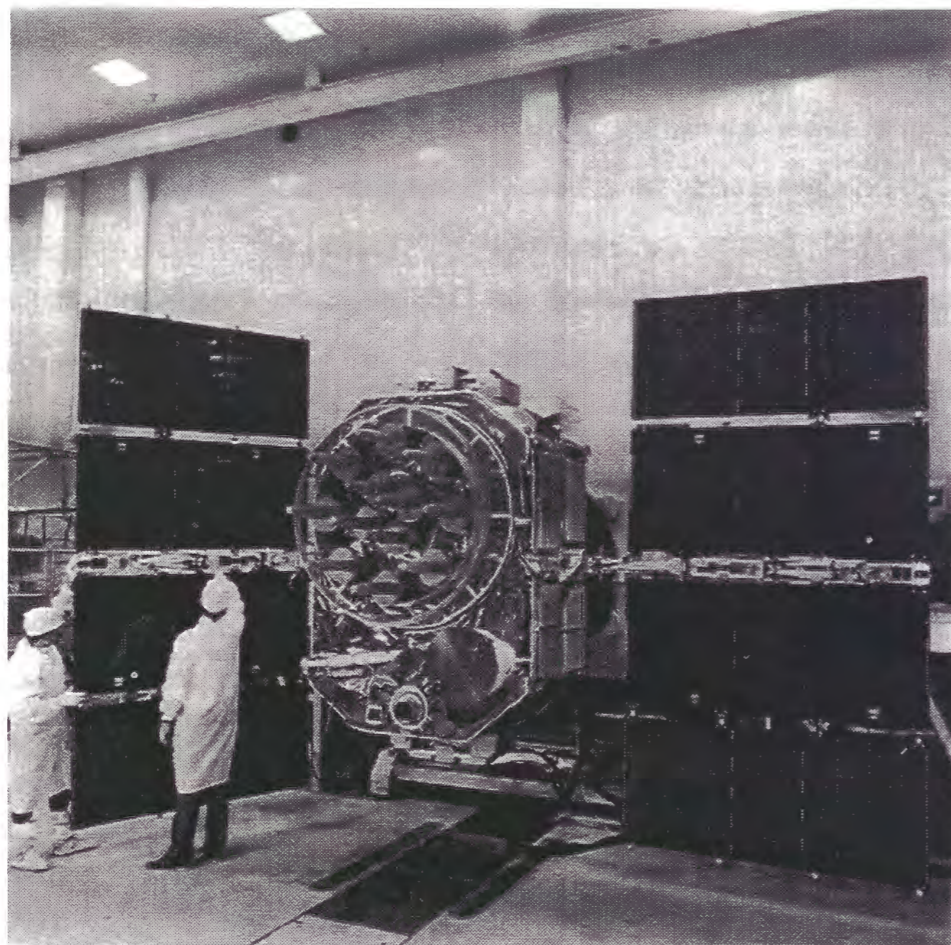


Fig.2-1 GPS satellite

Table 2-1 GPS satellite signals (bps = bits per second)

Atomic clock (Cs, Rb) fundamental frequency	10.23 MHz
L1 carrier signal	154 x 10.23 MHz
L1 frequency	1575.42 MHz
L1 wavelength	19.05 cm
L2 carrier signal	120 x 10.23 MHz
L2 frequency	1227.60 MHz
L2 wavelength	24.45 cm
P-code frequency (chipping rate)	10.23 MHz (Mbps)
P-code wavelength	29.31 m
P-code period	266 days; 7 days/satellite
C/A-code frequency (chipping rate)	1.023 MHz (Mbps)
C/A-code wavelength	293.1 m
C/A-code period	1 millisecond
data signal frequency	50 bps
data signal cycle length	30 seconds

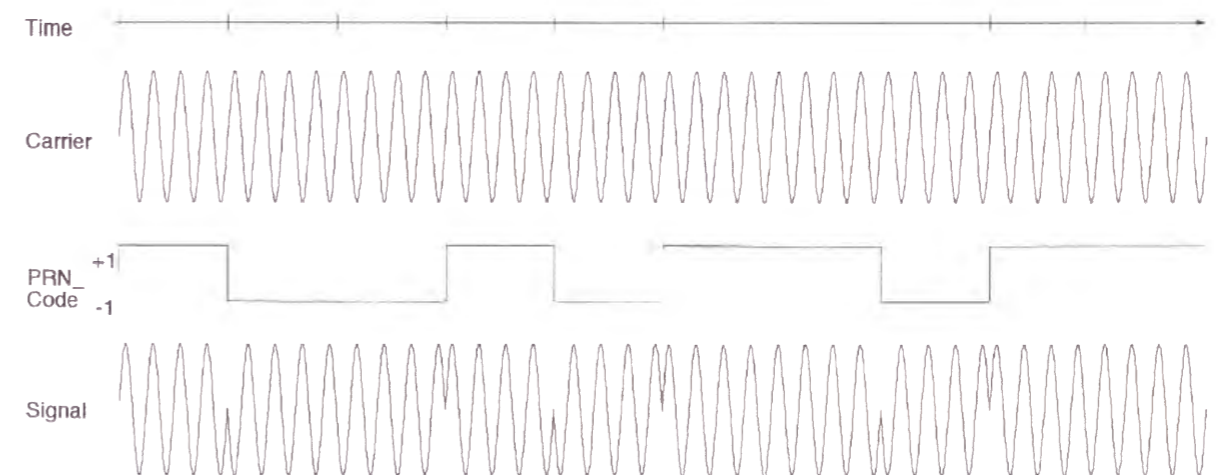


Fig.2-2 Structure of the GPS satellite signal

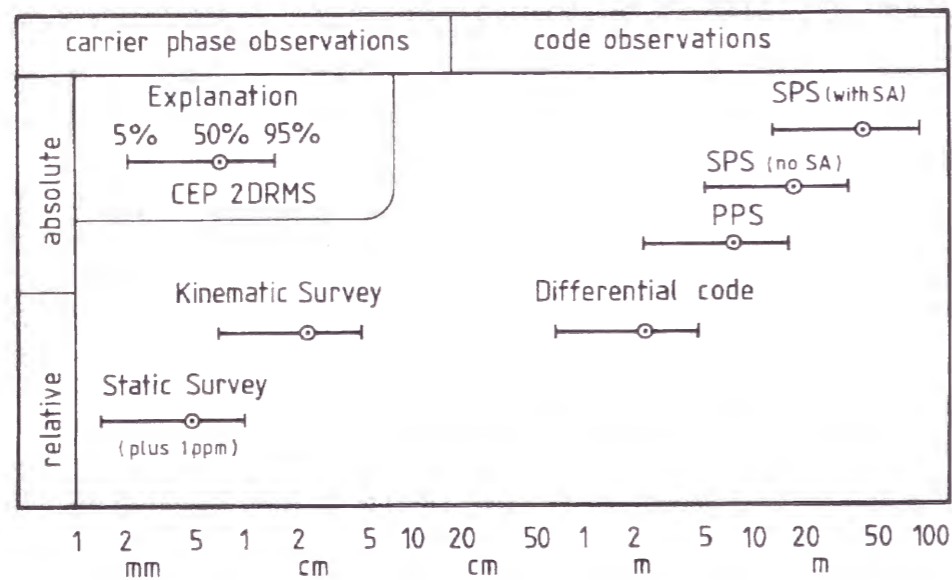


Fig.2-3 Horizontal positioning accuracy for SPS and PPS users

called Standard Positioning Service (SPS), while the service available to authorized (mainly military) users is called the Precise Positioning Service (PPS). Though C/A code is available for SPS users, the positioning accuracy will be degraded if the DoD operates the selective availability (SA). At present, SA is always active. In addition, when the Anti-Spoofing (A-S) is active, P code is changed to Y code that SPS users cannot access. The horizontal positioning accuracy for SPS and PPS users are given in Fig.2-3 (Seeber, 1993), in which the CEP (Circular Error Probable) for 50% probability and the 2DRMS (Distance Root Mean Square) for 95% probability are shown (Seeber, 1993,p295).

GPS receivers for navigation measure the propagation time from satellites to receivers using PRN codes and output the value of propagation time multiplied by the light speed 'c' as a distance information between satellites and receivers. Since this value includes errors such as satellite and receiver clock, it is called "pseudorange". The pseudorange (PR) is given as follows

$$PR = c(t - t_{SV}) + \epsilon_{PR} \quad (2.1-1)$$

where t is the time of signal reception by the receiver, t_{SV} is the signal transmitting time from the satellite, and ϵ_{PR} is the measurement noise. Since t and t_{SV} are measured by the receiver clock and the satellite clock respectively, they have their own clock-derived error, called "clock bias". Denoting the reception and transmission time in GPS time by T and T_{SV} , the clock biases of the receiver and satellite are

$$\begin{aligned} b &= c(t - T) \\ b_{SV} &= c(t_{SV} - T_{SV}) \end{aligned} \quad (2.1-2)$$

Then, Eq. (2.1-1) is rewritten as

$$\begin{aligned} PR &= c(t - T + T - T_{SV} + T_{SV} - t_{SV}) + \epsilon_{PR} \\ &= c(t - T) + c(T - T_{SV}) - c(t_{SV} - T_{SV}) + \epsilon_{PR} \\ &= c(T - T_{SV}) + b - b_{SV} + \epsilon_{PR} \end{aligned} \quad (2.1-3)$$

Denoting the position of receiver and satellite in the inertial space by $\mathbf{R}(T)$ and $\mathbf{R}_{SV}(T_{SV})$, the first term becomes

$$\begin{aligned} c(T - T_{SV}) &= \rho + d_{ion} + d_{trop} \\ \rho &= |\mathbf{R}(T) - \mathbf{R}_{SV}(T_{SV})| \end{aligned} \quad (2.1-4)$$

where ρ is the geometrical distance from the receiver to the satellite, d_{ion} and d_{trop} are delays when the signal propagates through ionosphere and troposphere. Since the ionospheric delay depends on the total electron involved in the ionosphere, the delay for L1 pseudorange is written as

$$d_{ion} = \frac{f_2}{f_1} I$$

$$I = 40.3 \frac{\int N_e(s) ds}{f_1 f_2} \quad (2.1-5)$$

where N_e is the density of electron, and f_1 , f_2 are L1, L2 frequency. The electron density is integrated along the signal propagation path and higher orders are neglected. Though Eq. (2.1-4) is expressed in the inertial coordinates, the position and velocity of GPS receivers and satellites should be expressed in an ECEF (Earth Centered Earth Fixed) coordinate system, called "WGS84" (World Geodetic System 1984). Denoting the position of receiver and satellite in WGS 84 by $\mathbf{r}(T)$ and $\mathbf{r}_{SV}(T_{SV})$ respectively, the geometrical distance becomes

$$\rho = |\mathbf{r}(T) - \mathbf{r}_{SV}(T_{SV})| + d_{sag} \quad (2.1-6)$$

d_{sag} shows a kind of special relativity effect, called "sagnac effect", where the propagation distance changes according to the earth rotation during the propagation. Sagnac effect is completely calculated using a mathematical equation (Murata and Harigae, 1992a). Although $\mathbf{r}_{SV}(T_{SV})$ in Eq. (2.1-6) is the true position of a satellite, we can only estimate the position in WGS 84 using the broadcast ephemeris or precise ephemeris calculated by some organizations. Denoting the error of the ephemeris by d_{eph} , Eq. (2.1-4) is transformed to

$$\rho = |\mathbf{r}(T) - \mathbf{r}_{SV}^*(T_{SV})| + d_{sag} + d_{eph}$$

$$= \rho^* + d_{sag} + d_{eph} \quad (2.1-7)$$

where \mathbf{r}_{SV}^* , ρ^* are the satellite position and geometrical distance calculated using the adopted ephemeris. From Eq. (2.1-3,4,7), the measurement equation of L1 pseudorange is written as follows

$$PR = \rho^* + \frac{f_2}{f_1} I + d_{trop} + b - b_{SV} + d_{eph} + d_{sag} + \varepsilon_{PR} \quad (2.1-8)$$

When SA is active, errors of satellite clock and broadcast ephemeris will be increased. Degrading the accuracy of broadcast ephemeris is called the ε -process and dithering of the satellite clock is called the δ -process (Murata and Harigae, 1992a). These errors will be included in d_{eph} and b_{SV} . When there are some reflecting surfaces near the receiver such as streets, buildings, waterways, and vehicles, the measurement accuracy of pseudorange is affected by reflected signals. The effect caused by these indirect signals is called "multipath". Multipath error, denoted by d_m , is very sensitive to the environment and sometimes reaches a few tens of meters for pseudorange. Adding the multipath error to Eq. (2.1-8) and removing the sagnac effect because it can be calculated exactly by a theoretical equation, the measurement equation of pseudorange is given as

$$PR = \rho^* + \frac{f_2}{f_1} I + d_{trop} + b - b_{SV} + d_{eph} + d_m + \varepsilon_{PR} \quad (2.1-9)$$

2.1.2 Carrier Phase

In the geodetic survey, carrier phase measurements are mainly used instead of the code phase measurements. This is because the measurement noise of the carrier phase is typically a few millimeters, while that of the code phase is a few meters generally. The carrier phase measured by the GPS receiver is the difference between the phase from the satellite at transmission time ($\theta_{SV}(t_{SV})$) and the phase generated by the receiver at reception time ($\theta(t)$). These phases are defined by the following equations (Remondi, 1985; Mader, 1986)

$$\theta_{SV}(t_{SV}) = f t_{SV} \quad (2.1-10)$$

$$\theta(t) = f t \quad (2.1-11)$$

where f is the frequency of the carrier and units are in cycles. In the above equations, the phases are defined to be zeros when the times are zeros in satellite and receiver

clocks, respectively. Thus, the carrier phase φ is described by

$$\varphi(t) = f(t - t_{sv}) + \varepsilon \quad (2.1-12)$$

where ε is the measurement noise. However, the observed carrier phase at the start time of measurement t_0 is only a fraction of the full wave. So, the observed carrier phase φ_m is written as follows at the initial time:

$$\varphi_m(t_0) = fr(\varphi(t_0)) \quad (2.1-13)$$

$fr(\cdot)$ means that the fractional part of a wave is taken. Hence, the real carrier phase which contains unmeasured integer cycle, N , is written as follows

$$\varphi(t_0) = \varphi_m(t_0) - N \quad (2.1-14)$$

Since the carrier phase is integrated continuously unless a cycle slip occurs, the measured carrier phase at time t is given by

$$\varphi_m(t) = \varphi(t) - \varphi(t_0) + \varphi_m(t_0) \quad (2.1-15)$$

Substituting Eq. (2.1-14) for Eq. (2.1-15), the measured carrier phase is

$$\varphi_m(t) = \varphi(t) + N \quad (2.1-16)$$

Since $\varphi(t)$ can be transformed like the pseudorange in Eq. (2.1-9), the measurement equation of the carrier phase is given by multiplying the wavelength λ by Eq. (2.1-16) and rewriting $\lambda\varphi_m(t)$ to ϕ as follows

$$\phi = \rho^* - \frac{f_2}{f_1} I + d_{trop} + b - b_{sv} + d_{eph} + d_{m,phase} + \lambda N + \varepsilon \quad (2.1-17)$$

In the above equations, the integer unknown ‘N’ is called “ambiguity”. $d_{m,phase}$ is the multipath error of the carrier phase, which is smaller than a few centimeters. Note that the sign of ionospheric delay is negative, while that for the pseudorange is positive.

In order to calculate the receiver position using these observables, it is important to reduce various kinds of errors in them. At first, the pseudorange should be smoothed using the carrier phase because the raw pseudorange is very noisy. In case of relative positioning with two or more receivers, a certain amount of these errors can be canceled by composing some kinds of linear combinations of the GPS data measured by the reference and user receivers.

2.1.3 Double Difference

At first, we compose the “single difference”. When two receivers and one satellite are considered, the single difference of carrier phase for the satellite- i is defined as the difference between measurements by receiver-1 and receiver-2 (Fig.2-4):

$$\Delta\phi_{1,2}^i = \phi_1^i - \phi_2^i \quad (2.1-18)$$

where subscripts denote the number of the receiver. Substituting Eq. (2.1-17) for Eq. (2.1-18), the result is

$$\Delta\phi = \Delta\rho^* - \frac{f_2}{f_1} \Delta I + \Delta d_{trop} + \Delta b + \Delta d_{eph} + \Delta d_{m,phase} + \lambda \Delta N + \Delta\varepsilon \quad (2.1-19)$$

The subscripts and superscript are omitted for simplicity.

The single difference of satellite clock bias is

$$b_{sv}(T_{sv1}) - b_{sv}(T_{sv2}) \cong \dot{b}_{sv}(T_{sv2}) \cdot (T_{sv1} - T_{sv2}) \quad (2.1-20)$$

Since the satellite clock drift, \dot{b}_{sv} , is nominally smaller than 10^{-3} and the difference of transmitting time is negligibly small, the satellite clock biases cancel each other. If the baseline length between two receivers is small (up to some 20km), the signal propagation paths for both receivers are similar, then the ionospheric and tropospheric delays almost cancel and also the ephemeris error almost cancels. The effect of propagation delay depending on baseline length will be evaluated in Chapter 3.

Assuming two receivers 1,2, and two satellites, i, j , to be involved, two single differences for satellite- i and satellite- j are formed. The “double difference” is defined as the difference between these single differences (Fig. 2-5). Denoting an operator to take the double difference by $\nabla\Delta$,

$$\nabla\Delta(\cdot) = (\cdot)_1^i - (\cdot)_2^i - (\cdot)_1^j + (\cdot)_2^j \quad (2.1-21)$$

the double difference of the carrier phase is given as follows

$$\nabla\Delta\phi = \nabla\Delta\rho^* - \frac{f_2}{f_1} \nabla\Delta I + \nabla\Delta d_{trop} + \nabla\Delta d_{eph} + \nabla\Delta d_{m,phase} + \lambda \nabla\Delta N + \nabla\Delta\varepsilon \quad (2.1-22)$$

The receiver clock biases cancel because the reception time of satellite- i and j signals are the same, so clock biases are also the same.

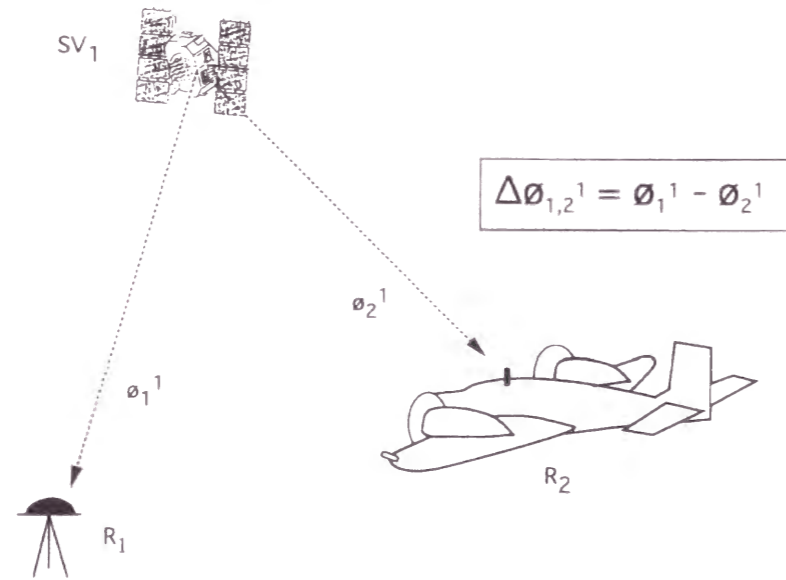


Fig.2-4 Single difference of GPS measurement

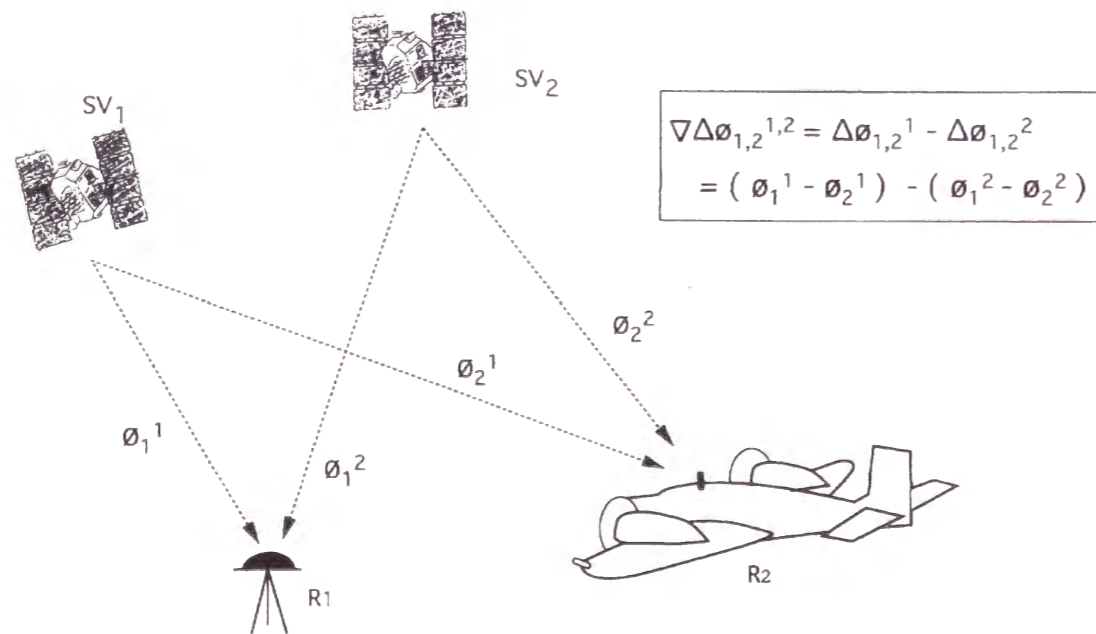


Fig.2-5 Double difference of GPS measurement

Moreover, taking the time difference between the double differences, the ambiguity is also canceled because it is a constant. This observable is called “triple difference”:

$$\delta \nabla \Delta \phi = \delta \nabla \Delta \rho^* - \frac{f_2}{f_1} \delta \nabla \Delta I + \delta \nabla \Delta d_{trop} + \delta \nabla \Delta d_{epi} + \delta \nabla \Delta d_{m,phase} + \delta \nabla \Delta \epsilon. \quad (2.1-23)$$

When the observation rate is high and the ionosphere and troposphere are stable, the propagation delays may be negligible. If the initial position of a vehicle is known, positioning with triple difference is very easily carried out because it is not necessary to resolve ambiguities, i.e., the initialization can be omitted. However, the positioning accuracy will be degraded gradually because the estimated position at an epoch depends on the position at the previous epoch, so the positioning error will be accumulated. Furthermore, once a cycle slip occurs and the number of visible satellites becomes less than 4, the positioning cannot be performed anymore.

2.1.4 Linear Combinations of GPS Measurements

When a dual frequency GPS receiver is used, some kinds of linear combinations of GPS measurements can be formed which are useful for the OTF and cycle slip detection (Blewitt, 1990). A linear combination of L1 and L2 carrier phases, which is called “widelane”, is formed as follows

$$\phi_w = \left(\frac{\phi_1}{\lambda_1} - \frac{\phi_2}{\lambda_2} \right) \frac{c}{f_1 - f_2}, \quad \begin{cases} \lambda_w = \frac{c}{f_1 - f_2} \cong 86.2 \text{ cm} \\ N_w = N_1 - N_2 \end{cases} \quad (2.1-24)$$

Subscript 1, 2, W denote L1, L2, and widelane observable. The double differenced widelane is

$$\nabla \Delta \phi_w = \nabla \Delta \rho + \nabla \Delta I + \nabla \Delta d_{trop} + \nabla \Delta d_{epi} + \nabla \Delta d_{m,w} + \lambda_w \nabla \Delta N_w + \nabla \Delta \epsilon_w. \quad (2.1-25)$$

Since the effective wavelength of widelane is about four times as large as L1 wavelength, to resolve widelane ambiguity is easier than for L1 ambiguity. However, the measurement noise becomes about three times as large as L1 noise and ionospheric delay error is enlarged by a factor of about 1.3 due to a coefficient $f_2/f_1 = 60/77 \cong 0.78$; therefore, the widelane is not suited to the final positioning solution.

From the L1 and L2 carrier phases, a so-called “narrowlane” observable is also formed as

$$\phi_N = \left(\frac{\phi_1}{\lambda_1} + \frac{\phi_2}{\lambda_2} \right) \frac{c}{f_1 + f_2}, \quad \begin{cases} \lambda_N = \frac{c}{f_1 + f_2} \cong 10.7 \text{ cm} \\ N_N = N_1 + N_2 \end{cases} \quad (2.1-26)$$

The double differenced narrowlane is

$$\nabla\Delta\phi_N = \nabla\Delta\rho - \nabla\Delta I + \nabla\Delta d_{trop} + \nabla\Delta d_{eph} + \nabla\Delta d_{m,N} + \lambda_N \nabla\Delta N_N + \nabla\Delta\epsilon_N. \quad (2.1-27)$$

Since the effective wavelength is about half of the L1 wavelength, to resolve ambiguity is difficult. However, the measurement noise is about half of the L1 noise, so the narrowlane solution may be a final solution for short baseline applications when the enlarged ionospheric delay error is sufficiently small.

From the widelane and narrowlane observable, the ionospheric delay free (ion-free) observable is formed as follows

$$\phi_{ion} = \frac{1}{2}(\phi_W + \phi_N) \quad (2.1-28)$$

The double differenced ion-free observable is

$$\nabla\Delta\phi_{ion} = \nabla\Delta\rho + \nabla\Delta d_{trop} + \nabla\Delta d_{eph} + \nabla\Delta d_{m,ion} + \frac{1}{2}(\lambda_W \nabla\Delta N_W + \lambda_N \nabla\Delta N_N) + \nabla\Delta\epsilon_{ion}. \quad (2.1-29)$$

Since the ionospheric delay cancels, this observable is suited to a long baseline application though the measurement noise is enlarged by a factor of about 3.

Finally, we introduce the so-called “ionospheric signal” as follows:

$$\begin{aligned} \phi_I &= \phi_N - \phi_W \\ &= -2I + \lambda_N N_N - \lambda_W N_W + (d_{m,N} - d_{m,W}) + (\epsilon_N - \epsilon_W) \end{aligned} \quad (2.1-30)$$

When the ambiguities of widelane and narrowlane, i.e., L1 and L2 carrier phase, and multipath errors are sufficiently small, the amount of ionospheric delay can be evaluated using this ionospheric signal. Results of evaluation will be discussed in Chapter 3. Also, this is useful for the cycle slip detection (Chapter 2.3).

2.2 Ambiguity Resolution On-the-Fly

The goal of ambiguity resolution is to determine the L1 ambiguity. However, the widelane ambiguity should be resolved beforehand because the position information calculated using widelane is used to determine the initial value of L1 ambiguity. Furthermore, the carrier-smoothed pseudorange is also used to determine the initial value of widelane ambiguity. Here, we give the observation equations of measurement data used in the OTF algorithm:

$$\nabla\Delta PR_1 = \nabla\Delta\rho^* + \nabla\Delta \frac{f_2}{f_1} I + \nabla\Delta d_{trop} + \nabla\Delta d_{eph} + \nabla\Delta d_{m1} + \nabla\Delta\epsilon_{PR_1}, \quad (2.2-1)$$

$$\nabla\Delta\phi_1 = \nabla\Delta\rho^* - \nabla\Delta \frac{f_1}{f_2} I + \nabla\Delta d_{trop} + \nabla\Delta d_{eph} + \nabla\Delta d_{m,phase} + \lambda_1 \nabla\Delta N_1 + \nabla\Delta\epsilon_1, \quad (2.2-2)$$

$$\nabla\Delta\phi_W = \nabla\Delta\rho^* + \nabla\Delta I + \nabla\Delta d_{trop} + \nabla\Delta d_{eph} + \nabla\Delta d_{m,W} + \lambda_W \nabla\Delta N_W + \nabla\Delta\epsilon_W. \quad (2.2-3)$$

where subscripts in Eq. (2.2-1) and (2.2-2) denote that the terms are for L1 frequency. Using these data step by step, we finally resolve the L1 ambiguity, and obtain the positioning solution. Measurement errors of three observables are different, which are listed in Table 2-2.

Table 2-2 Summary of measurement errors and corresponding position errors assuming RDOP=3. Values are for Trimble 4000sse receiver and include multipath error.

Observable	Measurement error (cm)	position error (cm)
DD of carrier smoothed pseudorange	65	195
DD of widelane carrier phase	4	12
DD of L1 carrier phase	1	3

These values are calculated using the accumulated data in our flight test configuration where two Trimble 4000SSE receivers were used. The reference receiver was connected to a Trimble Geodetic L1/L2 antenna with groundplane which mitigate the multipath error, while the onboard receiver was connected to a Tecom MIL-E-5400 antenna mounted on the roof of the Do-228 cockpit (see Chapter 4.1.1). Since the aircraft was on the ground about 200m away from the reference receiver, the propagation delays canceled and the ephemeris error was also negligible. However, the measurement error in Table 2-2 contains multipath error and measurement noise. We adopt these values as typical measurement errors in the OTF algorithm although they may slightly change with the circumstances; for example, when the aircraft banks deeply, their wings may become the reflecting surfaces and cause the multipath error. If we assumed the ideal condition such that there was no multipath effect, the measurement error would be the measurement noise. And if the measurement noise of the L1 carrier phase (~3mm for double differences) is almost the same as the L2 phase, the widelane measurement noise is about six times as large as the L1 measurement noise (Wübbena, 1989). However, the widelane measurement noise is worse at the present because the L2 carrier phase measurement is noisier than the L1 carrier phase when the A-S is active.

The flowchart of OTF algorithm is shown in Fig.2-6. The details are described step by step as follows (Tsuji et. al. 1995c, 1997b).

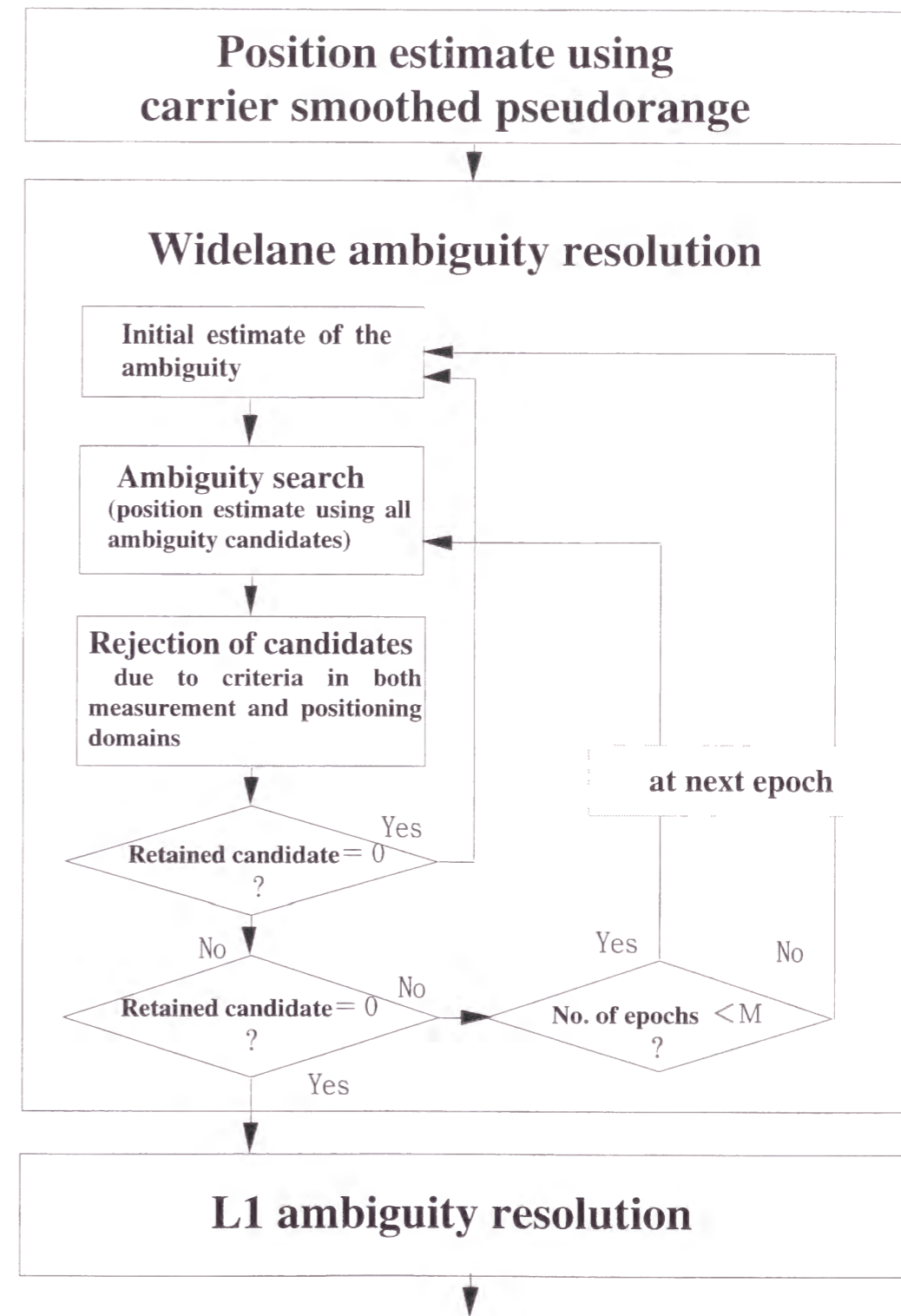


Fig.2-6 Flowchart of the OTF algorithm

(1) The initial estimate of widelane ambiguities are determined by Eq. (2.2-4) using the position of the receiver which is calculated using the double differences of carrier smoothed L1 pseudoranges.

$$\nabla\Delta N_{W0} = \text{idnint} \left(\frac{\nabla\Delta\phi_W - \nabla\Delta\rho^* - \nabla\Delta d_{trop}}{\lambda_W} \right) \quad (2.2-4)$$

The double differenced geometrical distances from the receiver to satellites, $\nabla\Delta\rho^*$, are calculated using pseudorange-position, and the tropospheric propagation delays are calculated using the Saastamoinen's zenith delay model with CfA2.2 mapping function (Chapter 3.1.2). The notation "idnint" means to make nearest integer. The correct integer ambiguity should be in a domain centered to the initial value shown in the following equation:

$$\nabla\Delta N_{W0}^i - k\sigma_N^W \leq \nabla\Delta N_{W0}^i \leq \nabla\Delta N_{W0}^i + k\sigma_N^W \quad (i=1,2,\dots,nsv-1) \quad (2.2-5)$$

where nsv denotes number of observed satellites, and σ_N^W denotes the standard deviation of initially estimated widelane ambiguity (see Fig.1-1). We set the integer k to 2 or 3, which correspond to the significant level of 95% or 99%, respectively. Although some authors (Abidin, 1993; Chen et. al., 1994; Knight, 1994) developed new methods to reduce the search number, we search the whole cube for the simplicity of the algorithm.

Now, we choose four satellites that have the minimum RDOP (Relative Dilution of Precision) as primary satellites among all of the observed satellites. The RDOP is a factor that is defined by the distribution of observed satellites in the sky, and given by the following equations:

$$RDOP = \sqrt{\text{trace}(H^T H)^{-1}} \quad (2.2-6)$$

$$H = \begin{pmatrix} \frac{\partial DD_1}{\partial \mathbf{r}} & \dots & \frac{\partial DD_{nsv-1}}{\partial \mathbf{r}} \end{pmatrix}^T = \begin{pmatrix} \frac{\mathbf{r}^T - \mathbf{r}_{SV1}^{*T}}{\rho_u^{*1}} & \dots & \frac{\mathbf{r}^T - \mathbf{r}_{SV2}^{*T}}{\rho_u^{*2}} \\ \vdots & & \vdots \\ \frac{\mathbf{r}^T - \mathbf{r}_{SV1}^{*T}}{\rho_u^{*1}} & \dots & \frac{\mathbf{r}^T - \mathbf{r}_{SVnsv}^{*T}}{\rho_u^{*nsv}} \end{pmatrix} \quad (2.2-7)$$

where H is the measurement matrix. ρ_u^{*i} is the distance from user receiver to i -th satellite. DD_i is the double differenced observable between the first and $i+1$ -th satellite, in which the smoothed pseudorange, widelane, or L1 carrier phase should be inserted. Using the RDOP, the standard deviation of double differenced measurement error σ_m and positioning error σ_p satisfy the following relation:

$$\sigma_p = RDOP \cdot \sigma_m \quad (2.2-8)$$

If three ambiguities of primary satellites are resolved, the position of the user receiver is obtained. Therefore, the ambiguities of secondary satellites can be computed by inserting the position calculated using ambiguities of primary satellites instead of the pseudorange-position into $\nabla\Delta\rho^*$ of the right side of Eq. (2.2-4). Therefore, we firstly resolve the ambiguities of primary satellites by the least squares searching method, and the ambiguities of the secondary satellites are resolved next. The covariance matrix of widelane ambiguity estimated using Eq. (2.2-4) is given by the following equation:

$$C_N^W = H(H^T C_{PR}^{-1} H)^{-1} H^T + C_W \quad (2.2-9)$$

where C_{PR} and C_W are the measurement error covariance matrix of smoothed pseudorange and widelane. When four primary satellites are used for positioning, there exists the inverse matrix, H^{-1} . Eq. (2.2-9) is then simplified as

$$C_N^W = C_{PR} + C_W \quad (2.2-10)$$

Hence, the standard deviation of the initially estimated ambiguity σ_N^W is

$$\sigma_N^W = \sqrt{\sigma_m^{PR2} + \sigma_m^{W2}} \cong 65 \text{ cm} \quad (2.2-11)$$

where $\sigma_m^{PR} = \sqrt{E\{(\nabla\Delta\varepsilon_{PR})^2\}}$ and $\sigma_m^W = \sqrt{E\{(\nabla\Delta\varepsilon_W)^2\}}$ are the standard deviations of smoothed pseudorange and widelane measurements, and the value right side is for a Trimble 4000SSE receiver. Fig.2-7 shows the relationship between the initial value of ambiguity and the candidate of ambiguity solution. Since the wavelength of widelane is about 86cm, the solution is in a range of initial value ± 2 cycles with

a significant level of 99%. Assuming that a range of initial value $\pm j$ cycles is to be searched, the number of ambiguity candidate becomes $(2j+1)^3$. In this case, the search number is $5^3=125$.

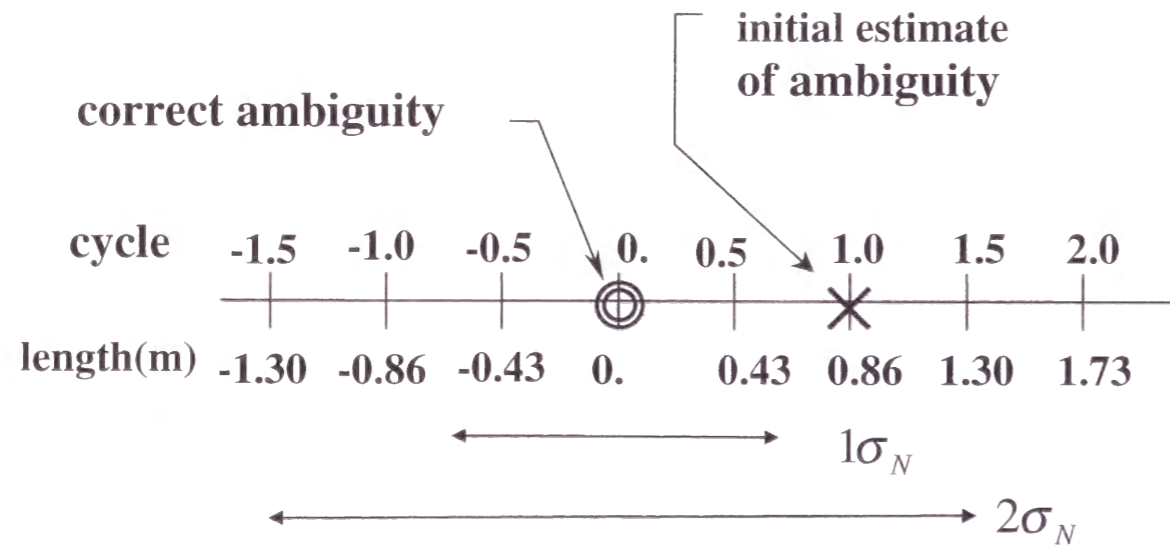


Fig.2-7 Relationship among the correct ambiguity, initial estimate of ambiguity, and its error

(2) Receiver position is computed with each ambiguity candidate, and the statistical tests are performed in the measurement domain and positioning domain.

(2a) Test in the measurement domain

The χ^2 test is performed using the sum of measurement residuals. The candidates satisfying the following condition are rejected:

$$\frac{\mathbf{v}^T \mathbf{C}_w^{-1} \mathbf{v}}{df} > \frac{\chi_{df, 1-\alpha}^2}{df} k_1^w \quad (2.2-12)$$

where \mathbf{v} , α , and df denote the residual vector, the significant level of the χ^2 test, and the degree of freedom ($= nsv-1$), respectively. k_1^w is an empirical parameter of tolerance, which is set to 1~2 in the experiments considered in this thesis.

(2b) Test in the positioning domain

Taking the differences between the horizontal position computed using smoothed pseudorange and those using each ambiguity candidate, the candidates satisfy the following condition are rejected:

$$\left| \mathbf{r}^{PR} - \mathbf{r}^W \right|_H > k_2^w \sigma_H^{PR-W} \quad (2.2-13)$$

where \mathbf{r}^{PR} and \mathbf{r}^W denote the position vectors of antenna calculated using smoothed pseudorange and wide lane, respectively, and $|\cdot|_H$ means to take the horizontal norm. σ_H^{PR-W} shows the standard deviation of the difference between the pseudorange-position and the widelane-position in the horizontal direction. k_2^w is an empirical parameter of tolerance, which is set to 2 or 3 in the experiments considered in this paper. Theoretically, $k_2^w = 1, 2, 3$ corresponds to the significant level of 68, 95, and 99%.

The standard deviation of position error when the pseudoranges are used is written as follows

$$\sigma_p^{PR} = RDOP \cdot \sigma_m^{PR} \quad (2.2-14)$$

where σ_m^{PR} is the standard deviation of pseudorange measurement error. This equation can be divided into horizontal and vertical directions:

$$\begin{cases} \sigma_H^{PR} = RHDOP \cdot \sigma_m^{PR} \\ \sigma_V^{PR} = RVDOP \cdot \sigma_m^{PR} \end{cases} \quad (2.2-15)$$

$$RDOP = \sqrt{RHDOP^2 + RVDOP^2}$$

The $RHDOP$ and $RVDOP$ indicate the dilution of relative positioning precision in the horizontal and vertical directions. The standard deviation of positioning error for widelane is written in a similar form. Therefore, the standard deviation of the difference between the pseudorange-position and widelane-position is given as follows

$$\sigma_H^{PR-W} = RHDOP \sqrt{\sigma_m^{PR2} + \sigma_m^{W2}} \quad (2.2-16)$$

If the considered ambiguity candidate is correct, the standard deviation will be

$$\sigma_H^{PR-W} = RHDOP\sqrt{65^2 + 4^2} \cong 65 \cdot RHDOP \text{ (cm)} \quad (2.2-17)$$

However, if there are 1-cycle errors, for example, in each ambiguity, the difference between the pseudorange-position and widelane-position will be increased as follows

$$\left| \mathbf{r}^{PR} - \mathbf{r}^W \right|_H \cong RHDOP\sqrt{65^2 + 86^2} \cong 108 \cdot RHDOP \text{ (cm)}; (2.2-18)$$

therefore the candidate may be rejected according to Inequality (2.2-13).

Although the horizontal position difference is evaluated in the above equations, the same result will be expected theoretically even if the vertical or three dimensional position difference is evaluated. The expectation is based on the assumption that the measurement errors are gaussian noises. However in reality, it is very difficult to completely remove the systematic errors from the measurements by theoretical models or by taking the double difference. The unremoved errors are propagation delay, ephemeris error, and multipath error, which degrade mainly the vertical positioning accuracy. Namely, since the vertical position scatters widely due to the unremoved errors, the usage of vertical position for the test causes an increase in the number of candidates that cannot be rejected. Therefore, it is better to evaluate the horizontal position in the positioning domain test.

(3) If only one ambiguity candidate set is retained, that is considered as the solution. And if more than one candidate are retained, similar statistical tests will be performed at the next epoch.

The tests shown in Eq. (2.2-12,13) are called local tests because measurement data of a single epoch are used. In addition to the local tests, the global tests that use the data of multiple epochs are performed.

(4) Procedure (2) and (3) are repeated until only one candidate is retained. If the number of total epochs exceed a threshold number, M, the process is back to (1).

(5) The initial values of L1 ambiguity are calculated from the widelane-position.

The standard deviation of initially estimated L1 ambiguity, σ_N^{L1} , is calculated by a similar equation with (2.2-11) as follows

$$\sigma_N^{L1} = \sqrt{\sigma_m^{W2} + \sigma_m^{L12}} \cong 4 \text{ cm} \quad (2.2-19)$$

Since the L1 wavelength is 19cm, the solution will be in a range of initial ambiguity ± 1 cycle (99%), and the search number is $3^3 = 27$.

(6) Procedures similar to (2) and (3) are repeated until only one candidate is retained. If the number of total epochs exceed a threshold number, M, the process is back to (5).

In the case of L1 ambiguity resolution, the test in positioning domain is very powerful. The standard deviation of the difference between the widelane-position and the L1-position is given by the next equation

$$\sigma_H^{W-L1} = RHDOP\sqrt{\sigma_m^{W2} + \sigma_m^{L12}} \quad (2.2-20)$$

If the ambiguities are correct, it will be

$$\sigma_H^{W-L1} = RHDOP\sqrt{4^2 + 1^2} \cong 4 \cdot RHDOP \text{ (cm)} \quad (2.2-21)$$

However, if the ambiguities are with 1-cycle errors, it will be approximately

$$\left| \mathbf{r}^W - \mathbf{r}^{L1} \right|_H \cong RHDOP\sqrt{4^2 + 19^2} \cong 19.4 \cdot RHDOP \text{ (cm)}. \quad (2.2-22)$$

Therefore, the considered candidate can be rejected easily. In Eq. (2.2-22), the horizontal position difference is evaluated as well as in the case of widelane ambiguity resolution.

There are two advantages in our OTF algorithm as follows:

A) The number of ambiguity candidate sets can be reduced effectively by resolving the widelane ambiguity before resolving the L1 ambiguity.

In our experimental configuration, the number of ambiguity candidates with a significant level of 99% are 125 and 27 for widelane and L1 ambiguity resolution, respectively; therefore, the total number of searches is $125+27=152$. On the other hand, if we resolve the L1 ambiguity set directly from the pseudorange-position, the number of searches can be calculated from the equations below,

$$\sigma_N^{L1} = \sqrt{\sigma_m^{PR2} + \sigma_m^{L12}} \cong 65 \text{ cm}, \quad \frac{3\sigma_N^{L1}}{\lambda_1} \cong 10 \text{ cycle} \quad (2.2-23)$$

namely, $(2 \times 10 + 1)^3 = 9261$, which is approximately 60 times as large as in the former case.

B) The ambiguity of the L1 carrier phase is resolved quickly and reliably by conducting the test in the positioning domain, which can be adopted if the widelane observable is used intermediately.

Assuming that the widelane observable is not used, the standard deviation of the difference between the pseudorange-position and the L1-position will become as follows when the ambiguities are correct:

$$\begin{aligned}\sigma_H^{PR-L1} &= RHDOP \sqrt{\sigma_m^{PR2} + \sigma_m^{L12}} \\ &= RHDOP \sqrt{65^2 + 1^2} \cong 65 \cdot RHDOP\end{aligned}\quad (\text{cm}). \quad (2.2-24)$$

Also, when the ambiguities are with 1-cycle errors, the position difference will be

$$\left| \mathbf{r}^{PR} - \mathbf{r}^{L1} \right|_H \cong RHDOP \sqrt{65^2 + 19^2} \cong 68 \cdot RHDOP \quad (\text{cm}), \quad (2.2-25)$$

which is not so different from the former case. This means the statistical test in the positioning domain has no effect in this case.

2.3 Cycle Slip Detection

The cycle slip occurs if the receiver loses phase lock of the satellite signal. The most frequent reason is signal obstruction due to trees, buildings, or vehicles themselves. Another reason is a low SNR due to bad ionospheric conditions, multipath, high receiver dynamics, or low satellite elevation. When a cycle slip occurs, the carrier phase jumps by an integer cycle while the fractional part of the phase remains unchanged. The cycle slip may be as small as a few cycles, or exceed millions of cycles. Cycle slips have to be detected because the corresponding measurements are not available for positioning until the new ambiguities are resolved. However, cycle slips can be easily detected for dual frequency by monitoring the ionospheric signal in Eq. (2.1-30). Taking the time difference of the ionospheric signal and denoting it, $SLIP$, the result with no cycle slip is

$$\begin{aligned}SLIP &\equiv \phi_I(t_n) - \phi_I(t_{n-1}) \\ &= -2\{I(t_n) - I(t_{n-1})\}\end{aligned}\quad (2.3-1)$$

where the multipath and measurement noise are omitted. If a cycle slip occurs in the L1 and L2 carriers as δN_1 and δN_2 , the index will jump as

$$\begin{aligned}SLIP &= -2\{I(t_n) - I(t_{n-1})\} + \lambda_N(\delta N_1 + \delta N_2) - \lambda_W(\delta N_1 - \delta N_2) \\ &= -2\{I(t_n) - I(t_{n-1})\} - 75.5 \cdot \delta N_1 + 96.9 \cdot \delta N_2\end{aligned}\quad (\text{cm}). \quad (2.3-2)$$

Assuming the measurement noise of L1 and L2 carrier phase as 0.1 radians, corresponding to 3mm and 3.9mm, respectively, the measurement noise of the ionospheric signal is 20mm. Then the measurement noise in $SLIP$ becomes 28mm because the time difference is taken. Therefore, even a cycle slip of one cycle in the L1 or L2 carrier would be easily detected by using a threshold value, 8.4cm (3σ). However, there are some special cases in which the detection is very difficult, for example, 5-cycles slip in the L1 and 4-cycles in the L2 carrier, that cause only a 10cm jump in $SLIP$. Nevertheless, since L1 and L2 cycle slips are independent and normally large numbers, we adopt this index to detect cycle slips. When a cycle slip is detected and the phase locks of more than three satellites are maintained, the corresponding ambiguity is computed using the receiver position obtained from the remaining satellites' carrier phases. And if the number of satellites maintaining the phase locks becomes less than four, the OTF is performed as the initialization. Instead of the initialization, some methods of cycle slip fixing have been proposed using a simple linear regression (Mader, 1986), or using the Kalman filtering (Bastos and Landau 1988; Landau, 1989).

If L1 single frequency receiver is used, the cycle slip may be detected using the carrier smoothed pseudorange (Lachapelle, et. al., 1992a), \overline{PR}_1 , as

$$\begin{aligned}SLIP_S &\equiv \{\phi_1(t_n) - \overline{PR}_1(t_n)\} - \{\phi_1(t_{n-1}) - \overline{PR}_1(t_{n-1})\} \\ &= -2 \frac{f_2}{f_1} \{I(t_n) - I(t_{n-1})\}\end{aligned}\quad , \quad (2.3-3)$$

or using the carrier doppler, $\dot{\phi}_1$, as

$$SLIP_D \equiv \{\phi_1(t_n) - \phi_1(t_{n-1})\} - \dot{\phi}_1(t_n) \cdot (t_n - t_{n-1}) \quad . \quad (2.3-4)$$

However, the detection of a few cycles slip would be difficult because the accuracy of smoothed pseudorange is normally worse than 50cm and the doppler changes significantly during the observation interval. If the smoothed pseudorange or carrier doppler were sufficiently accurate, these indexes could be used for cycle slip fixing.

2.4 Positioning Algorithm

Two types of positioning methods are used in our software. The least squares method is used in the OTF algorithm to calculate positions for each ambiguity candidate set. And the extended Kalman filter is used for positioning after the widelane/L1 ambiguity are resolved, while the least squares method is also available in this case.

2.4.1 Least Squares Method

Herein, the double differenced measurement vector is denoted by \mathbf{y} as

$$\mathbf{y} = (DD_1, DD_2, \dots, DD_{nsv-1})^T \quad (2.4-1)$$

where DD is the double difference of pseudorange, widelane, or L1 carrier phase.

Denoting a priori position of the receiver by $\bar{\mathbf{r}}$, and computed measurement vector by $\bar{\mathbf{y}}$, the next relation is satisfied

$$\begin{aligned} \mathbf{y} - \bar{\mathbf{y}} &= H(\mathbf{r} - \bar{\mathbf{r}}) + \mathbf{e} \\ \delta\mathbf{y} &= H\delta\mathbf{r} + \mathbf{e} \end{aligned} \quad (2.4-2)$$

where H and \mathbf{e} are the measurement matrix written in Eq. (2.2-7) and the measurement error vector. We wish to minimize the scalar cost function J , where

$$J = (\delta\mathbf{y} - H\delta\mathbf{r})^T C^{-1} (\delta\mathbf{y} - H\delta\mathbf{r}) \quad (2.4-3)$$

C is the covariance matrix of the measurement given as

$$\begin{aligned} C &= E[\mathbf{e}\mathbf{e}^T] \\ &= E[(\varepsilon_1^1 - \varepsilon_1^2 - \varepsilon_2^1 + \varepsilon_2^2, \varepsilon_1^1 - \varepsilon_1^3 - \varepsilon_2^1 + \varepsilon_2^3, \dots, \varepsilon_1^1 - \varepsilon_1^{nsv} - \varepsilon_2^1 + \varepsilon_2^{nsv})^T \\ &\quad (\varepsilon_1^1 - \varepsilon_1^2 - \varepsilon_2^1 + \varepsilon_2^2, \varepsilon_1^1 - \varepsilon_1^3 - \varepsilon_2^1 + \varepsilon_2^3, \dots, \varepsilon_1^1 - \varepsilon_1^{nsv} - \varepsilon_2^1 + \varepsilon_2^{nsv})] \quad (2.4-4) \\ &= 2s^2 \begin{pmatrix} 2 & & 1 \\ & \ddots & \\ 1 & & 2 \end{pmatrix} \end{aligned}$$

assuming that the measurement errors are independent for all satellites and the standard deviations are the same which is denoted by $s (= \sqrt{E[\varepsilon^2]})$. The superscript of ε denotes the satellite number and the subscript denotes the receiver number, not the

L1/L2 band. Then the inverse of covariance is gives as follows

$$C^{-1} = \frac{1}{nsv} \frac{2}{s^2} \begin{pmatrix} nsv-1 & & -1 \\ & \ddots & \\ -1 & & nsv-1 \end{pmatrix} \quad (2.4-5)$$

The weighted least squares estimate is then given as

$$\delta\hat{\mathbf{r}} = (H^T C^{-1} H)^{-1} H^T C^{-1} \delta\mathbf{y} \quad (2.4-6)$$

If the measurement error, \mathbf{e} , is assumed to be a zero mean and gaussian-distributed noise, the estimate is also the maximum likelihood estimate. In our software, an orthogonal transformation approach with the givens rotation is used as follows:

$$\mathbf{U}\delta\hat{\mathbf{r}} = \mathbf{b} \quad (2.4-7)$$

where \mathbf{U} is the upper triangular matrix and the estimate is obtained by backward substitution.

The error covariance matrix of the state is given as

$$C_r = (H^T C^{-1} H)^{-1} \quad (2.4-8)$$

Denoting the diagonal elements of C_r by q_{xx}, q_{yy}, q_{zz} , the standard deviation of position estimate, σ_p , is

$$\begin{aligned} \sigma_p &= \sqrt{q_{xx} + q_{yy} + q_{zz}} \\ &= \sqrt{\text{trace}(H^T C^{-1} H)^{-1}} \end{aligned} \quad (2.4-9)$$

Here, we define the $RDOP$ as

$$RDOP \equiv \sqrt{\text{trace}(H^T C^{-1} H) / \sigma_m^2} \quad (2.4-10)$$

where σ_m^2 is the standard deviation of double differenced measurement that is equal to the diagonal element of C , i.e., $4s^2$ (in the OTF algorithm, $RDOP$ is simplified as Eq. (2.2-6)). Therefore, the standard deviation of position and measurement satisfy Eq. (2.2-8),

$$\sigma_p = RDOP \cdot \sigma_m \quad (2.2-8)$$

If the carrier doppler data are available, the velocity of user receiver is estimated more precisely. Since the carrier doppler is time derivative of the carrier phase, the observation equation and its double difference are expressed as follows

$$\dot{\phi} = \dot{\rho}^* - \frac{f_2}{f_1} \dot{I} + \dot{d}_{trop} + \dot{b} - \dot{b}_{SV} + \dot{d}_{eph} + \dot{d}_{m,phase} + \dot{\epsilon} \quad (2.4-11)$$

$$\nabla \Delta \dot{\phi} = \nabla \Delta \dot{\rho}^* + \nabla \Delta \dot{\epsilon} \quad (2.4-12)$$

In Eq. (2.4-12), most of the measurement errors are neglected. When the velocity is estimated, the measurement matrix, H , is extended as follows

$$H = \begin{pmatrix} \frac{\partial \nabla \Delta \dot{\phi}_1}{\partial \mathbf{r}} & \dots & \frac{\partial \nabla \Delta \dot{\phi}_{nsv-1}}{\partial \mathbf{r}} & \frac{\partial \nabla \Delta \dot{\phi}_1}{\partial \dot{\mathbf{r}}} & \dots & \frac{\partial \nabla \Delta \dot{\phi}_{nsv-1}}{\partial \dot{\mathbf{r}}} \end{pmatrix}^T$$

$$= \begin{pmatrix} \frac{\mathbf{r}^T - \mathbf{r}_{SV1}^{*T}}{\rho_u^{*1}} - \frac{\mathbf{r}^T - \mathbf{r}_{SV2}^{*T}}{\rho_u^{*2}} & \dots & \dots & \dots & \dots & \dots \\ \vdots & \vdots & \vdots & \vdots & \vdots & \vdots \\ \frac{\mathbf{r}^T - \mathbf{r}_{SV1}^{*T}}{\rho_u^{*1}} - \frac{\mathbf{r}^T - \mathbf{r}_{SVnsv}^{*T}}{\rho_u^{*nsv}} & \dots & \dots & \dots & \dots & \dots \\ \vdots & \vdots & \vdots & \vdots & \vdots & \vdots \\ \frac{\dot{\mathbf{r}}^T - \dot{\mathbf{r}}_{SV1}^{*T}}{\rho_u^{*1}} - \frac{\dot{\mathbf{r}}^T - \dot{\mathbf{r}}_{SV2}^{*T}}{\rho_u^{*2}} & \frac{\dot{\mathbf{r}}^T - \dot{\mathbf{r}}_{SV1}^{*T}}{\rho_u^{*1}} & \frac{\dot{\mathbf{r}}^T - \dot{\mathbf{r}}_{SV2}^{*T}}{\rho_u^{*2}} & \dots & \dots & \dots \\ \vdots & \vdots & \vdots & \vdots & \vdots & \vdots \\ \frac{\dot{\mathbf{r}}^T - \dot{\mathbf{r}}_{SV1}^{*T}}{\rho_u^{*1}} - \frac{\dot{\mathbf{r}}^T - \dot{\mathbf{r}}_{SVnsv}^{*T}}{\rho_u^{*nsv}} & \frac{\dot{\mathbf{r}}^T - \dot{\mathbf{r}}_{SV1}^{*T}}{\rho_u^{*1}} & \frac{\dot{\mathbf{r}}^T - \dot{\mathbf{r}}_{SVnsv}^{*T}}{\rho_u^{*nsv}} & \dots & \dots & \dots \end{pmatrix} \quad (2.4-13)$$

And the error covariance matrix of the measurement and the state, (C, C_r) are also extended correspondingly.

2.4.2 Extended Kalman Filter

A system dynamics below is considered in the Kalman filtering.

$$\dot{\mathbf{x}} = F\mathbf{x} + B\mathbf{u} \quad (2.4-14)$$

In our application, the state vector contains the aircraft position, velocity and acceleration $(\mathbf{r}, \mathbf{v}, \mathbf{a})$ as follows

$$\mathbf{x} = \begin{pmatrix} \mathbf{r} \\ \mathbf{v} \\ \mathbf{a} \end{pmatrix} \quad (2.4-15)$$

The so-called acceleration dead reckoning (ADR) model is adopted as an aircraft dynamics model:

$$\begin{cases} \dot{\mathbf{r}} = \mathbf{v} \\ \dot{\mathbf{v}} = \mathbf{a} \\ \dot{\mathbf{a}} = -\frac{1}{\tau}\mathbf{a} + \mathbf{u} \end{cases} \quad (2.4-16)$$

Namely, a Gauss-Markov process is assumed for acceleration, in which τ is the time constant and \mathbf{u} is the white noise. This can be written in the next form,

$$\begin{pmatrix} \dot{\mathbf{r}} \\ \dot{\mathbf{v}} \\ \dot{\mathbf{a}} \end{pmatrix} = \begin{pmatrix} \mathbf{O}_{3 \times 3} & \mathbf{I}_{3 \times 3} & \mathbf{O}_{3 \times 3} \\ \mathbf{O}_{3 \times 3} & \mathbf{O}_{3 \times 3} & \mathbf{I}_{3 \times 3} \\ \mathbf{O}_{3 \times 3} & \mathbf{O}_{3 \times 3} & -\frac{1}{\tau}\mathbf{I}_{3 \times 3} \end{pmatrix} \begin{pmatrix} \mathbf{r} \\ \mathbf{v} \\ \mathbf{a} \end{pmatrix} + \begin{pmatrix} \mathbf{O}_{3 \times 3} \\ \mathbf{O}_{3 \times 3} \\ \mathbf{I}_{3 \times 3} \end{pmatrix} \mathbf{u} \quad (2.4-17)$$

Then, the matrix F and B are expressed as

$$F = \begin{pmatrix} \mathbf{O}_{3 \times 3} & \mathbf{I}_{3 \times 3} & \mathbf{O}_{3 \times 3} \\ \mathbf{O}_{3 \times 3} & \mathbf{O}_{3 \times 3} & \mathbf{I}_{3 \times 3} \\ \mathbf{O}_{3 \times 3} & \mathbf{O}_{3 \times 3} & -\frac{1}{\tau}\mathbf{I}_{3 \times 3} \end{pmatrix}, \quad B = \begin{pmatrix} \mathbf{O}_{3 \times 3} \\ \mathbf{O}_{3 \times 3} \\ \mathbf{I}_{3 \times 3} \end{pmatrix} \quad (2.4-18)$$

The covariance matrix for the process noise \mathbf{u} is given by

$$Q = E\{\mathbf{u}\mathbf{u}^T\} = \begin{pmatrix} q_{ax} & 0 & 0 \\ 0 & q_{ay} & 0 \\ 0 & 0 & q_{az} \end{pmatrix} \quad (2.4-19)$$

In order to implement this system model into the computer programs, the differential equation of motion has to be transformed to a discrete form such as

$$\mathbf{x}(t_k) = \Phi(t_k, t_{k-1})\mathbf{x}(t_{k-1}) + G(t_k)\mathbf{w}(t_k) \quad (2.4-20)$$

where

$$E\left\{ \begin{pmatrix} \mathbf{w}(t_k) \\ \mathbf{v}(t_k) \end{pmatrix} \begin{pmatrix} \mathbf{w}(t_l)^T & \mathbf{v}(t_l)^T \end{pmatrix} \right\} = \begin{pmatrix} \tilde{Q}(t_k) & 0 \\ 0 & C(t_k) \end{pmatrix} \delta_{kl} \quad (2.4-21)$$

This form is also suited for the U-D factorization in which the numerical stability is of special concern (Katayama, 1983). Then the problem herein is to express matrixes Φ, G, Q' by F, B, Q .

The matrix Φ and F generally satisfy the following equations

$$\dot{\Phi}(t, t_{k-1}) = F(t)\Phi(t, t_{k-1}) \quad (2.4-22)$$

$$\Phi(t_{k-1}, t_{k-1}) = I \quad (2.4-23)$$

Since the matrix $F(t)$ is constant ($= F$) in this application, the state transition matrix Φ is expressed by F as the next equation

$$\begin{aligned} \Phi(t, t_{k-1}) &= \Phi(t - t_{k-1}) \\ &= e^{F(t-t_{k-1})} \\ &= I + F \cdot (t - t_{k-1}) + \frac{1}{2!} F^2 \cdot (t - t_{k-1})^2 + \dots \end{aligned} \quad (2.4-24)$$

Therefore, the transition matrix is given explicitly as follows

$$\begin{aligned} \Phi(t_k, t_{k-1}) &= \Phi(\Delta) \\ &= \begin{pmatrix} I_{3 \times 3} & \Delta I_{3 \times 3} & \Phi_{13} \\ O_{3 \times 3} & I_{3 \times 3} & \Phi_{23} \\ O_{3 \times 3} & O_{3 \times 3} & \Phi_{33} \end{pmatrix}, \end{aligned} \quad (2.4-25)$$

$$\begin{aligned} \Phi_{13} &= \frac{\Delta^2}{2} - \frac{\Delta^3}{6\tau} \\ \Phi_{23} &= \Delta - \frac{\Delta^2}{2\tau} + \frac{\Delta^3}{6\tau^2} \\ \Phi_{33} &= 1 - \frac{\Delta}{\tau} + \frac{\Delta^2}{2\tau^2} - \frac{\Delta^3}{6\tau^3} \end{aligned} \quad (2.4-26)$$

where the fourth or higher order terms concerning $\Delta (= t_k - t_{k-1})$ are neglected. On the other hand, the solution of Eq. (2.4-14) is given by

$$\mathbf{x}(t_k) = \Phi(t_k, t_{k-1})\mathbf{x}(t_{k-1}) + \int_{t_{k-1}}^{t_k} \Phi(t_k, \xi) B(\xi) \mathbf{u}(\xi) d\xi \quad (2.4-27)$$

The second part of the right side,

$$\mathbf{x}' \equiv \int_{t_{k-1}}^{t_k} \Phi(t_k, \xi) B(\xi) \mathbf{u}(\xi) d\xi \quad (2.4-28)$$

is the accumulated process noise between t_{k-1} and t_k . If the process noise \mathbf{u} were constant from t_{k-1} to t_k as $\mathbf{u}'(t_k)$, Eq. (2.4-27) would be approximated as

$$\mathbf{x}' \equiv \left[\int_{t_{k-1}}^{t_k} \Phi(t_k, \xi) B(\xi) d\xi \right] \cdot \mathbf{u}'(t_k) \quad (2.4-29)$$

Comparing this with Eq. (2.4-19), G and \mathbf{w} will be of the form:

$$\begin{aligned} G(t_k) &= \int_{t_{k-1}}^{t_k} \Phi(t_k, \xi) B d\xi \\ &= \begin{pmatrix} \frac{\Delta^3}{6} I_{3 \times 3} \\ \left(\frac{\Delta^2}{2} - \frac{\Delta^3}{6\tau} \right) I_{3 \times 3} \\ \left(\Delta - \frac{\Delta^2}{2\tau} + \frac{\Delta^3}{6\tau^2} \right) I_{3 \times 3} \end{pmatrix}, \end{aligned} \quad (2.4-30)$$

$$\mathbf{w}(t_k) \equiv \mathbf{u}'(t_k) \quad (2.4-31)$$

Now, we adopt an average of process noise as $\mathbf{u}'(t_k)$, i.e.,

$$\mathbf{u}'(t_k) \equiv \int_{t_{k-1}}^{t_k} \mathbf{u}(\xi) d\xi / \Delta \quad (2.4-32)$$

Then the covariance for process noise in the discrete model will be

$$\begin{aligned} Q'(t_k) &= E(\mathbf{u}'(t_k) \mathbf{u}'(t_k)^T) \\ &= \int_{t_{k-1}}^{t_k} Q(\xi) d\xi / \Delta^2 \end{aligned} \quad (2.4-33)$$

Since the covariance for process noise is assumed to be constant in this model as $Q(\xi) = Q$, it will be

$$\begin{aligned} Q' &= Q / \Delta \\ &= \begin{pmatrix} q_{ax} / \Delta & 0 & 0 \\ 0 & q_{ay} / \Delta & 0 \\ 0 & 0 & q_{az} / \Delta \end{pmatrix} \end{aligned} \quad (2.4-34)$$

On the other hand, the measurement equations, which are already given by Eq. (2.2-1,2,3), can be written as

$$\mathbf{y} = h(\mathbf{x}) + \mathbf{e} \quad (2.4-35)$$

The measurement matrix $H = \left(\frac{\partial h}{\partial \mathbf{x}} \right)^T$ and the error covariance for measurement are given in Eq. (2.2-7) and Eq. (2.4-4). If the velocity of the user receiver would be estimated, the extended measurement matrix (Eq. (2.4-13)) and the covariance matrix would be used. Though the measurements are given in the form of vector, they are treated as an order of scalar in the computer program. Now we gave the entire matrixes requisite for implementation of the extended Kalman filter.

2.5 Attitude Determination Algorithm

In addition to the precise position of a vehicle, the GPS interferometric technique can give attitude information if the vehicle has more than one antenna onboard. Some results have been reported using a dedicated receiver such as the Trimble Tans Vector (Cohen and Parkinson, 1992; Cohen et. al., 1993) and Ashtech 3DF (Graas and Braasch, 1994). The advantage of the dedicated receiver is that the clock oscillator is common for all channels. That means there is one additional degree of freedom in the determination of attitude. However, the line bias calibration has to be performed before the attitude determination (Uematsu, 1994). On the other hand, results using a non-dedicated receiver system were also reported (Cannon and Sun, 1994; MacMillan et. al., 1995). The system comprised three or more independent receivers mounted on the platform, and has the advantages of cost-effectiveness and flexibility to be used for a variety of applications in addition to attitude determination (Sun, 1994).

An airborne attitude determination system using independent receivers has also been developed at NAL. Preliminary flight tests were conducted on 4 October 1995 at Nagoya, Japan (Tsujii et. al., 1995c, 1996c). Two Trimble 4000SSE GPS receivers were installed in NAL's Dornier Do-228-200 (Do-228) research aircraft, a twin engined turboprop aircraft with two L1 antennas mounted on the fuselage. Since two antennas were installed forward and aft on the fuselage, the yaw and pitch angles were estimated. The attitude estimated by GPS was compared with the attitude data from the Inertial Navigation System (INS), and the differences were 0.1 deg in pitch and 0.2 deg in yaw.

Furthermore, two L1 antennas were mounted on the wing tips of the Do-228 in autumn, 1996, to provide the roll angle as well as pitch and yaw. The first flight experiments with this 4-antenna attitude system were conducted in October, 1996. The objective of this study is to establish the algorithms for GPS carrier-based attitude determination, including the structural flexure estimate, for many kinds of platform such as aircraft, ships, satellites, and space structures.

2.5.1 Attitude Determination

The attitude of an aircraft is defined by a rotation transformation between a coordinate system fixed in the body and a coordinate system fixed in the local level (North East Down). At first, the body frame was determined by three vectors between the four GPS antennas as shown in Fig.2-8. The elements of vectors in the body frame are calculated by a one-hour GPS static survey and are listed in Table 2-3.

Next, the positions of the front, left wing, and right wing antennas relative to the rear antenna are calculated precisely using the kinematic GPS positioning algorithm described previously. In the algorithm, the double-differenced L1 carrier phases are used to eliminate satellite and receiver clock offsets. After double-differenced integer ambiguities are resolved on-the-fly using the least squares searching method, the three antenna vectors are calculated by the least squares method. Then the aircraft attitude is determined by transforming the body frame coordinates of the antenna vectors to the local level coordinates.

Suppose $\mathbf{r}_j^B = (x_j^B, y_j^B, z_j^B)^T$, $j = 1 \sim 3$, are the antenna vectors of j-th antenna in the body frame, and $\mathbf{r}_j^L = (N_j, E_j, D_j)^T$ are those in the local level frame. Then the 3×3 matrix $\mathbf{r}^B = (\mathbf{r}_1^B, \mathbf{r}_2^B, \mathbf{r}_3^B)$ and $\mathbf{r}^L = (\mathbf{r}_1^L, \mathbf{r}_2^L, \mathbf{r}_3^L)$ satisfy the following relation:

$$\mathbf{r}^B = R_L^B(\varphi, \theta, \psi) \mathbf{r}^L = \begin{pmatrix} \cos \theta \cos \psi & \cos \theta \sin \psi & -\sin \theta \\ \sin \varphi \sin \theta \cos \psi - \cos \varphi \sin \psi & \sin \varphi \sin \theta \sin \psi + \cos \varphi \cos \psi & \sin \varphi \cos \theta \\ \cos \varphi \sin \theta \cos \psi + \sin \varphi \sin \psi & \cos \varphi \sin \theta \sin \psi - \sin \varphi \cos \psi & \cos \varphi \cos \theta \end{pmatrix} \mathbf{r}^L, \quad (2.5-1)$$

where $R_L^B(\varphi, \theta, \psi)$, φ, θ, ψ are a rotation matrix, roll, pitch, and yaw angle respectively. If there is no structural flexure, the rotation matrix is calculated using the least squares method to minimize the following cost function

$$J = \sum_{i,j} [\mathbf{r}^{B0} - R_L^B(\varphi, \theta, \psi) \mathbf{r}^L]_{ij}^2 \quad (2.5-2)$$

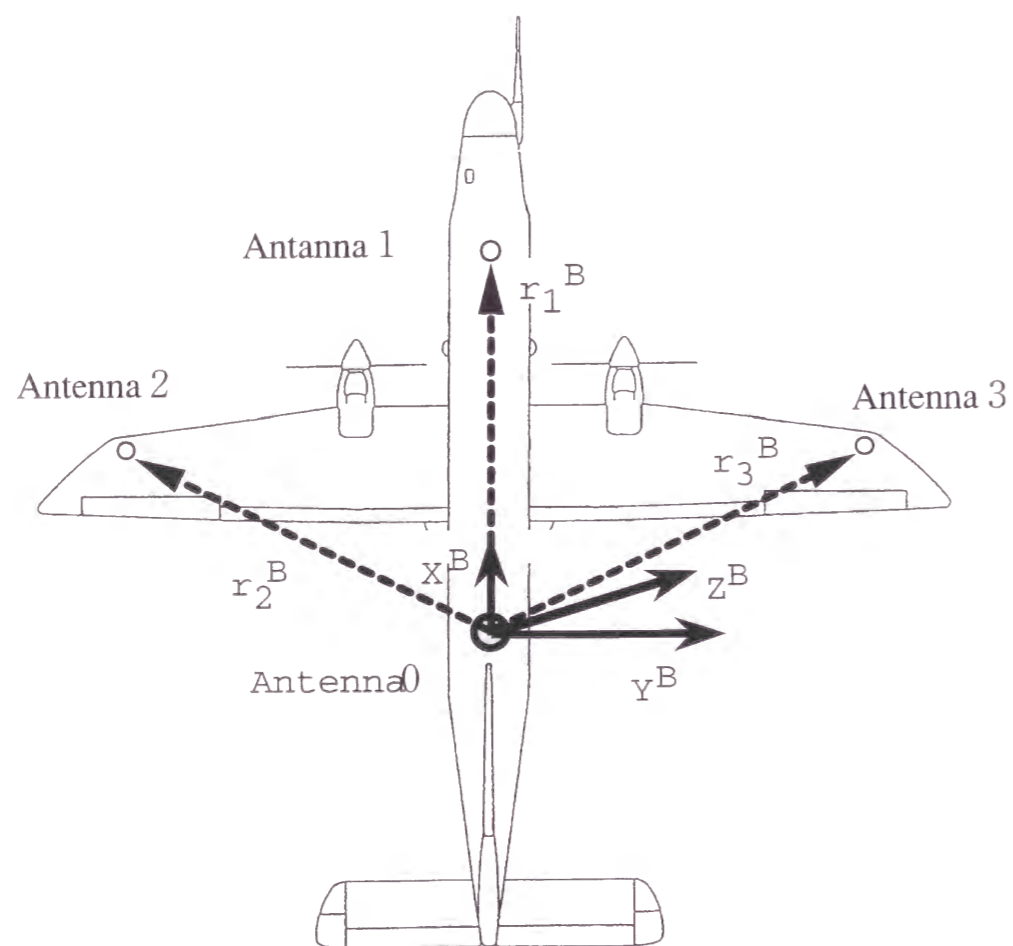


Fig.2-8 Aircraft body frame defined by four GPS antennas

Table 2-3 Body frame coordinates of antenna vectors

	X^B	Y^B	Z^B
\mathbf{r}_1^B	6.413	0	0
\mathbf{r}_2^B	3.121	-7.637	-0.048
\mathbf{r}_3^B	3.508	7.626	-0.093

(Unit: m)

2.5.2 Structural Flexure Modeling

The importance of the wing flexure modeling to obtain precise aircraft attitude has been reported by several authors (Cohen, et. al., 1993; Cannon and Sun, 1994). Additionally, the lateral flexure of the aircraft fuselage is modeled in this study because the fuselage is likely to bend when yaw angle changes rapidly. To estimate the vertical flexure of the fuselage is difficult because the direction of the vertical fuselage is the same as that of wing flexure. Supposing \mathbf{r}^{B0} and \mathbf{r}^B are antenna vector matrices when the aircraft is stationary and in motion, respectively. The structural flexure matrix B is introduced as follows:

$$\begin{aligned} \mathbf{r}^B &= \mathbf{r}^{B0} - B \\ &= \mathbf{r}^{B0} - (\mathbf{b}_1, \mathbf{b}_2, \mathbf{b}_3) \\ &= \mathbf{r}^{B0} - \begin{pmatrix} 0 & 0 & 0 \\ -fl & -fl & -fl \\ 0 & fw & fw \end{pmatrix} \end{aligned} \quad (2.5-3)$$

where fw is the wing flexure and fl is the lateral flexure of the fuselage as shown in Fig.2-9. The fw and fl are positive when the wing and the fuselage flexes upward and rightward respectively. In this case, the cost function to be minimized is given by

$$J = \sum_{i,j} [\mathbf{r}^{B0} - B - R_L^B(\varphi, \theta, \psi) \mathbf{r}^L]_{ij}^2 \quad (2.5-4)$$

2.5.3 Least Squares Adjustment

In this chapter, we give the mathematical equations for attitude determination by the least squares method. The state vector to be estimated is defined as follows

$$\mathbf{x}_a = (\varphi, \theta, \psi, fw, fl)^T \quad (2.5-5)$$

Now, we introduce a fictitious measurement vector \mathbf{y}_a (9×1) as

$$\begin{aligned} \mathbf{y}_a &\equiv \mathbf{h}(\mathbf{x}_a) \\ &= \begin{pmatrix} \mathbf{b}_1 \\ \mathbf{b}_2 \\ \mathbf{b}_3 \end{pmatrix} - \begin{pmatrix} R_L^B \mathbf{r}_1^L \\ R_L^B \mathbf{r}_2^L \\ R_L^B \mathbf{r}_3^L \end{pmatrix} \end{aligned} \quad (2.5-6)$$

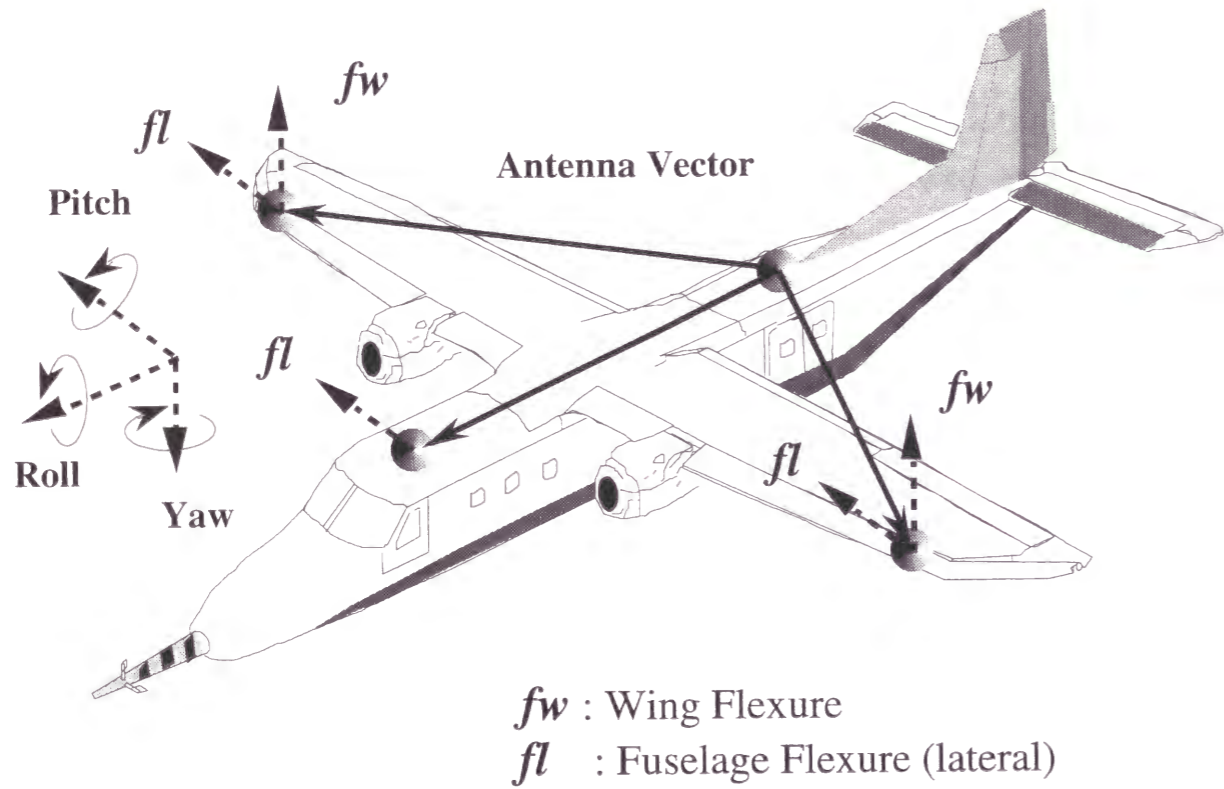


Fig.2-9 Structural flexure modeling

Denoting a priori state vector by $\bar{\mathbf{x}}_a$, and computed measurement vector by $\bar{\mathbf{y}}_a$, the residual vector is given as

$$\begin{aligned} \delta\mathbf{y}_a &\equiv \begin{pmatrix} \mathbf{r}_1^{B0} \\ \mathbf{r}_2^{B0} \\ \mathbf{r}_3^{B0} \end{pmatrix} - \bar{\mathbf{y}}_a \\ &= \left. \frac{\partial \mathbf{h}_a(\mathbf{x}_a)}{\partial \mathbf{x}_a} \right|_{\mathbf{x}_a = \bar{\mathbf{x}}_a} (\mathbf{x}_a - \bar{\mathbf{x}}_a) \\ &= H_a(\bar{\mathbf{x}}_a) \delta\mathbf{x}_a \end{aligned} \quad (2.5-7)$$

Therefore, the least squares estimate which minimizes the cost function in Eq. (2.5-4) is given as

$$\delta\hat{\mathbf{x}}_a = (H_a^T H_a)^{-1} H_a^T \delta\mathbf{y}_a \quad (2.5-8)$$

The measurement matrix H_a (9×5) is written as

$$H_a = \begin{pmatrix} \frac{\partial R_{1i}}{\partial \varphi} r_{i1} & \frac{\partial R_{1i}}{\partial \theta} r_{i1} & \frac{\partial R_{1i}}{\partial \psi} r_{i1} & 0 & 0 \\ \frac{\partial R_{2i}}{\partial \varphi} r_{i1} & \frac{\partial R_{2i}}{\partial \theta} r_{i1} & \frac{\partial R_{3i}}{\partial \psi} r_{i1} & 0 & -1 \\ \frac{\partial R_{3i}}{\partial \varphi} r_{i1} & \frac{\partial R_{3i}}{\partial \theta} r_{i1} & \frac{\partial R_{3i}}{\partial \psi} r_{i1} & 0 & 0 \\ \frac{\partial R_{1i}}{\partial \varphi} r_{i2} & \frac{\partial R_{1i}}{\partial \theta} r_{i2} & \frac{\partial R_{1i}}{\partial \psi} r_{i2} & 0 & 0 \\ \frac{\partial R_{2i}}{\partial \varphi} r_{i2} & \frac{\partial R_{2i}}{\partial \theta} r_{i2} & \frac{\partial R_{3i}}{\partial \psi} r_{i2} & 0 & -1 \\ \frac{\partial R_{3i}}{\partial \varphi} r_{i2} & \frac{\partial R_{3i}}{\partial \theta} r_{i2} & \frac{\partial R_{3i}}{\partial \psi} r_{i2} & 1 & 0 \\ \frac{\partial R_{1i}}{\partial \varphi} r_{i3} & \frac{\partial R_{1i}}{\partial \theta} r_{i3} & \frac{\partial R_{1i}}{\partial \psi} r_{i3} & 0 & 0 \\ \frac{\partial R_{2i}}{\partial \varphi} r_{i3} & \frac{\partial R_{2i}}{\partial \theta} r_{i3} & \frac{\partial R_{2i}}{\partial \psi} r_{i3} & 0 & -1 \\ \frac{\partial R_{3i}}{\partial \varphi} r_{i3} & \frac{\partial R_{3i}}{\partial \theta} r_{i3} & \frac{\partial R_{3i}}{\partial \psi} r_{i3} & 1 & 0 \end{pmatrix} \quad (2.5-9)$$

where the R_{ij} , r_{ij} denote (i,j) elements of matrix R_L^B and \mathbf{r}^L . The partial derivatives of R_{ij} with respect to attitude angles are given in the following equations:

$$\frac{\partial R_{11}}{\partial \varphi} = 0$$

$$\frac{\partial R_{11}}{\partial \theta} = -\sin \theta \cos \psi$$

$$\frac{\partial R_{11}}{\partial \psi} = -\cos \theta \sin \psi$$

$$\frac{\partial R_{12}}{\partial \varphi} = 0$$

$$\frac{\partial R_{12}}{\partial \theta} = -\sin \theta \sin \psi$$

$$\frac{\partial R_{12}}{\partial \psi} = \cos \theta \cos \psi$$

$$\frac{\partial R_{13}}{\partial \varphi} = 0$$

$$\frac{\partial R_{13}}{\partial \theta} = -\cos \theta$$

$$\frac{\partial R_{13}}{\partial \psi} = 0$$

$$\frac{\partial R_{21}}{\partial \varphi} = \cos \varphi \sin \theta \cos \psi + \sin \varphi \sin \psi$$

$$\frac{\partial R_{21}}{\partial \theta} = \sin \varphi \cos \theta \cos \psi$$

$$\frac{\partial R_{21}}{\partial \psi} = -\sin \varphi \sin \theta \sin \psi - \cos \varphi \cos \psi$$

$$\frac{\partial R_{22}}{\partial \varphi} = \cos \varphi \sin \theta \sin \psi - \sin \varphi \cos \psi$$

$$\frac{\partial R_{22}}{\partial \theta} = \sin \varphi \cos \theta \sin \psi$$

$$\frac{\partial R_{22}}{\partial \psi} = \sin \varphi \sin \theta \cos \psi - \cos \varphi \sin \psi$$

$$\frac{\partial R_{23}}{\partial \varphi} = \cos \varphi \cos \theta$$

$$\frac{\partial R_{23}}{\partial \theta} = -\sin \varphi \sin \theta$$

$$\frac{\partial R_{23}}{\partial \psi} = 0$$

$$\frac{\partial R_{31}}{\partial \varphi} = -\sin \varphi \sin \theta \cos \psi + \cos \varphi \sin \psi$$

$$\frac{\partial R_{31}}{\partial \theta} = \cos \varphi \cos \theta \cos \psi$$

$$\frac{\partial R_{31}}{\partial \psi} = -\cos \varphi \sin \theta \sin \psi + \sin \varphi \cos \psi$$

$$\frac{\partial R_{32}}{\partial \varphi} = -\sin \varphi \sin \theta \sin \psi - \cos \varphi \cos \psi$$

$$\frac{\partial R_{32}}{\partial \theta} = \cos \varphi \cos \theta \sin \psi$$

$$\frac{\partial R_{32}}{\partial \psi} = \cos \varphi \sin \theta \cos \psi + \sin \varphi \sin \psi$$

$$\frac{\partial R_{33}}{\partial \varphi} = -\sin \varphi \cos \theta$$

$$\frac{\partial R_{33}}{\partial \theta} = -\cos \varphi \sin \theta$$

$$\frac{\partial R_{33}}{\partial \psi} = 0$$

(2.5-10)

2.5.4 Comparison with INS Attitude

In order to use the INS attitude measurement as the attitude reference, the misalignment errors between two coordinate systems have to be calibrated. Antenna vectors in the INS frame are converted from those in the local level frame via a rotation matrix R_L^I :

$$\mathbf{r}^I = R_L^I(\varphi_I, \theta_I, \psi_I) \mathbf{r}^L \quad (2.5-11)$$

where $\varphi_I, \theta_I, \psi_I$ are the attitude angles measured by the INS. Then \mathbf{r}^I is converted to \mathbf{r}^B as follows

$$\begin{aligned} \mathbf{r}^B &= R_I^B \mathbf{r}^I \\ &= R_I^B R_L^I \mathbf{r}^L \end{aligned} \quad (2.5-12)$$

If the transformation matrix from the INS frame to the body frame, R_I^B , is known, a transformation matrix, R_L^B , can be computed

$$R_L^B(\varphi_i', \theta_i', \psi_i') = R_i^B R_L^I \quad (2.5-13)$$

where $\varphi_i', \theta_i', \psi_i'$ are the calibrated INS attitude. R_i^B is given by

$$R_i^B = R_L^B R_i^L \quad (2.5-14)$$

When the aircraft is stationary on the ground, R_i^B is constant because the body frame is unchanged. However, during flight, the body frame changes due to the structural flexure (Eq. (2.5-3)) while the INS frame can be assumed to be unchanged. Therefore, R_i^B changes epoch by epoch when the aircraft is in motion. R_i^B is averaged over the flight and is used to calibrate the INS measurement. Note that the calibrated INS attitude is defined by the rotation from the local level frame to the 'averaged body frame'. Accordingly, the difference between GPS and INS attitude will increase naturally when the aircraft is in a strong maneuver, which results in large structural flexure.

Chapter 3

Evaluation of Positioning Accuracy

Although several efforts have been made in order to evaluate the positioning accuracy by KGPS, it is difficult to find other equipment for positioning whose accuracy is similar or better than KGPS. A laser tracker can be imagined, but there seem to be some problems. For example, it is difficult to calibrate the tracker mounting error with sufficient accuracy, and its positioning accuracy degrades when the distance between the tracker and the reflector is increased. An attempt will be made here, namely, analyses of static baselines by KGPS. Solutions of KGPS will be compared with the positions which were determined previously by software for static survey, and the time variation of positioning error and effects of various errors will be discussed. Data taken from the Izu-Islands area are used for the evaluation. Since this area is located in a volcanically and tectonically active zone, a number of GPS receivers have been installed by several organizations. We analyzed eight baselines with various lengths chosen from six observation sites. Then the possibility of OTF depending on the baseline length is discussed using the same data. Finally, we demonstrate that a crustal movement due to an earthquake with a few centimeters level can be detected by kinematic GPS positioning (Tsujii et. al., 1997c).

3.1 Evaluation of Positioning Accuracy Using Static Data

3.1.1 Comparison with Static Positioning Solutions

We analyzed data from six observation sites, namely Kozujima, Niijima, Miyakeizu, Miyaketsubota, Minamiizu, and Shizuoka. Locations of those sites are shown in Fig.3-1, The eight baselines used and their lengths are listed in Table 3-1.

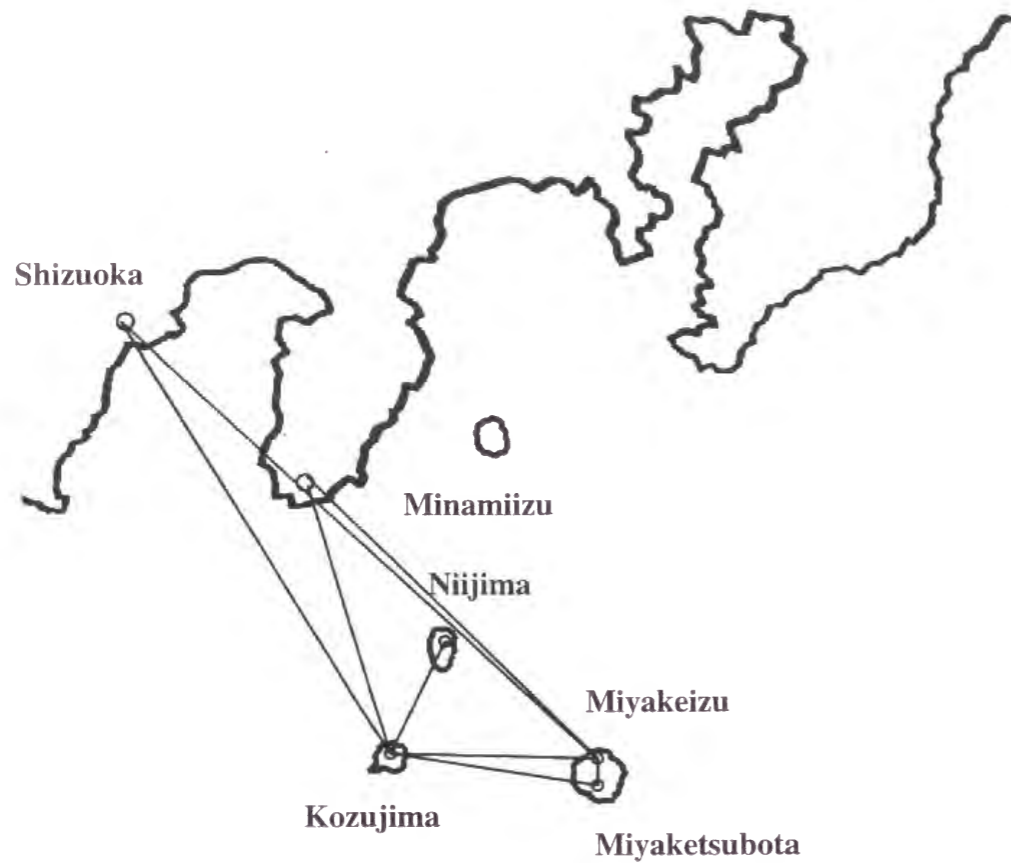


Fig.3-1 Map of Izu-Islands area

Table 3-1 Summary of baselines and their lengths

Baseline No.	Reference station	User station	baseline length(km)
1	Miyakeizu	Miyaketsubota	7.951
2	Niijima	Kouzujiima	22.146
3	Miyakeizu	Kozujima	35.182
4	Miyaketsubota	Kozujima	41.173
5	Minamiizu	Kozujima	56.695
6	Minamiizu	Miyakeizu	84.029
7	Shizuoka	Kozujima	106.719
8	Shizuoka	Miyakeizu	136.005

The receivers are Trimble 4000SSE, and those antennas are with groundplanes that mitigate the multipath effect. Data from Minamiizu are provided by the University of Tokyo, and others are by the Geodetic Survey Institute of Japan.

An earthquake with magnitude 5.6 occurred on 6 Oct. 1995, in the sea near Kozujima, and accordingly the position of Kozujima moved eastward 2-3 cm (University of Nagoya and Shizuoka University, 1996). In order to compare the KGPS solutions with static position, we analyzed the data of 5 Oct. 1995 in this section. We assume that there was no crustal movement before the earthquake. Static position solutions of those sites were estimated by using the software, GAMIT, which was published at the Massachusetts Institute of Technology. The data were recorded from 6 to 18 o'clock in GPS time at 60-second intervals, and the precise ephemeris made by the International GPS Service (IGS) was used. Minamiizu site was used as a reference site, and positions of other sites were estimated relative to the reference site.

Then we compared the KGPS solution with the GAMIT solutions. Fig.3-2 (a-f) show the difference between these two solutions. In the kinematic analyses, double differenced ionospheric-free measurements were used, and the IGS precise ephemeris was also used instead of the broadcast ephemeris. The tropospheric propagation delay was calculated using the Saastamoinen's zenith delay model and the Cfa2.2 mapping function, where meteorological data were set to the standard values (temperature 20°C, humidity 50%, pressure 1013HPa) for all sites. In case of baselines No.1 - 5, L1 and L2 ambiguities were correctly resolved except for a period around 17 o'clock and later. These miss-fixings of ambiguity occurred because only 4 to 5 satellites were visible and their constellation was inadequate in that period. Fig.3-3 shows the time variation of RHDOP and RVDOP for baseline No.2. The DOP values were quite similar for other baselines because we treated a local area. The RMS (Root Mean Square) of RHDOP and RVDOP during all observation time were 1.35 and 1.78 respectively. It can be seen clearly that the positioning accuracy correlates with the baseline length. For baseline No. 6, ambiguities were not resolved correctly from 11:30 to 12:30, and for baselines No.7 and 8, correct ambiguities were never resolved. Since the positioning accuracy obviously degrades according to the increase of baseline length, the baseline dependence of the various kinds of errors will be evaluated in the next section.

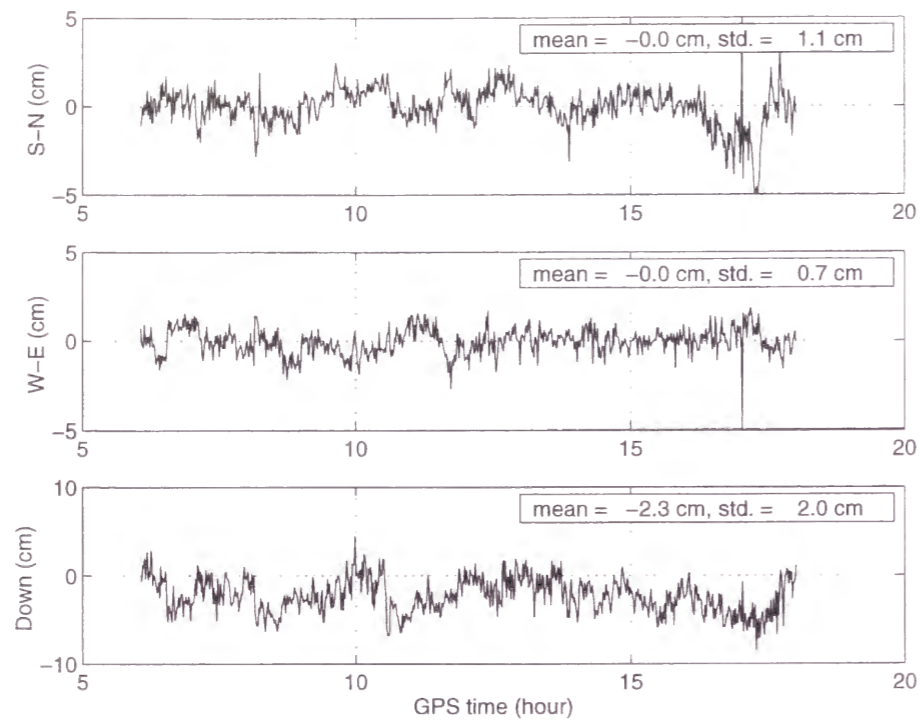


Fig.3-2a KGPS positioning errors when ionospheric-free observable was used (Deviations from the GAMIT static solutions on DOY278) (Miyakeizu - Miyaketsubota, 7.951km)

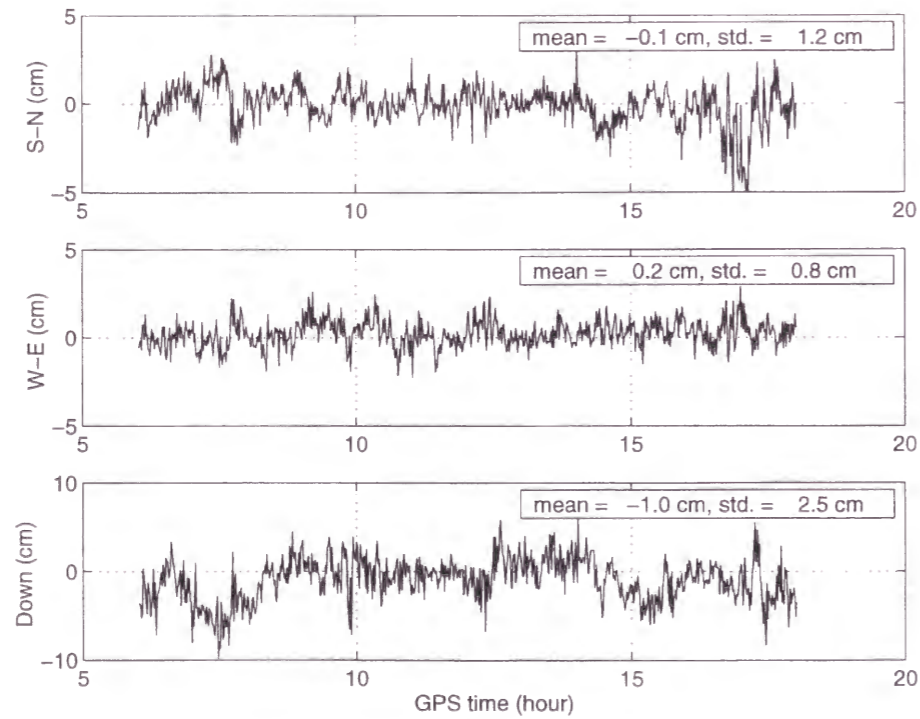


Fig.3-2b Errors of ionospheric-free KGPS solution (Niijima - Kozujima, 22.146km)

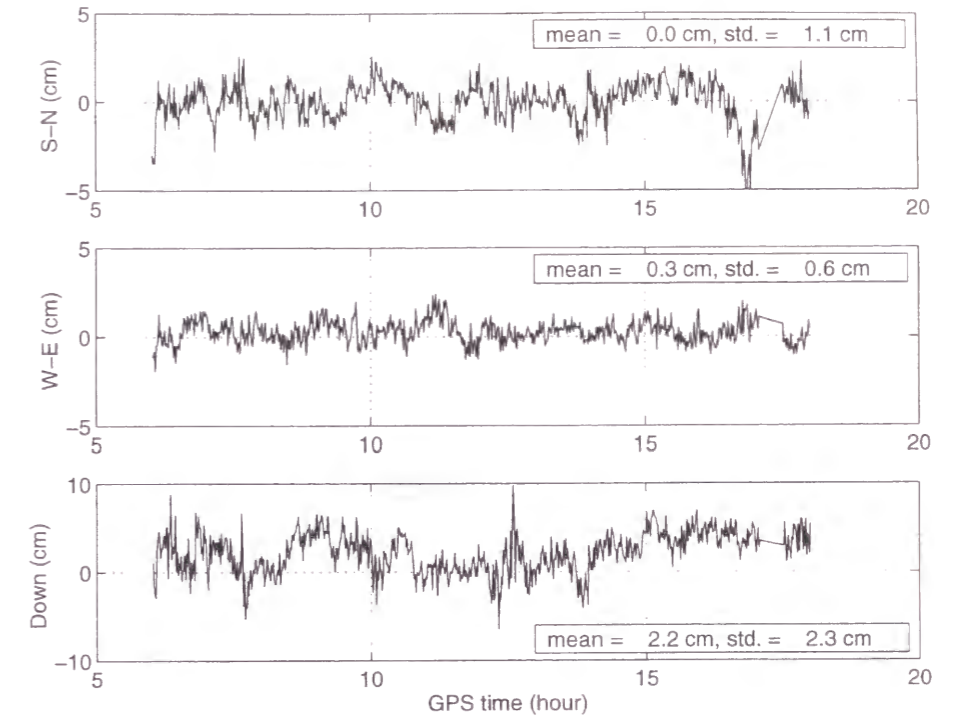


Fig.3-2c Errors of ionospheric-free KGPS solution (Miyakeizu - Kozujima, 35.182km)

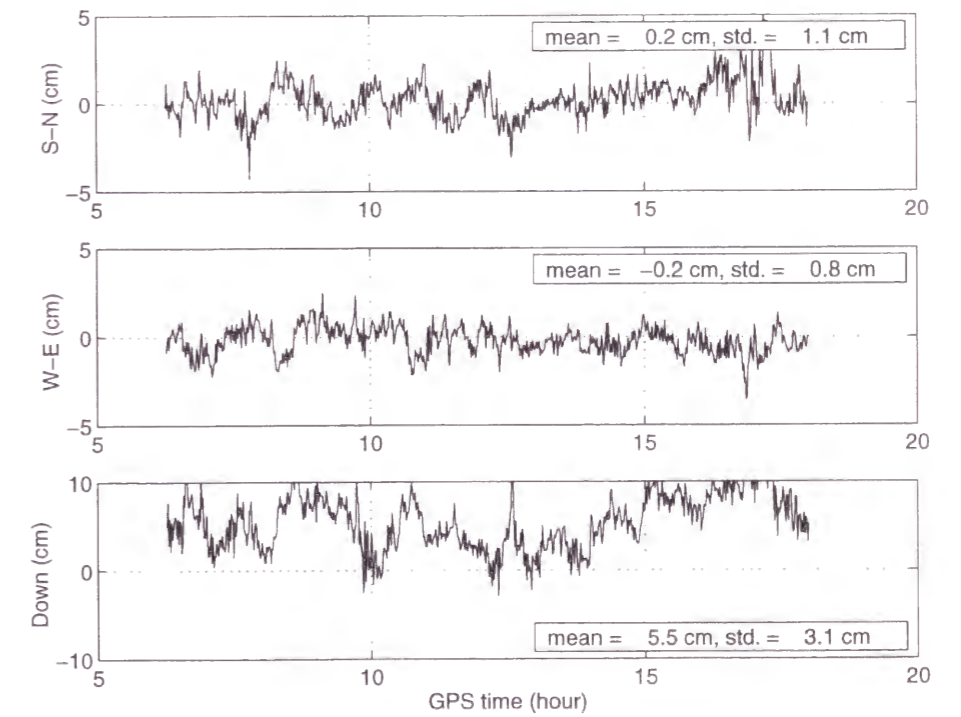


Fig.3-2d Errors of ionospheric-free KGPS solution (Miyaketsubota - Kozujima, 41.173km)

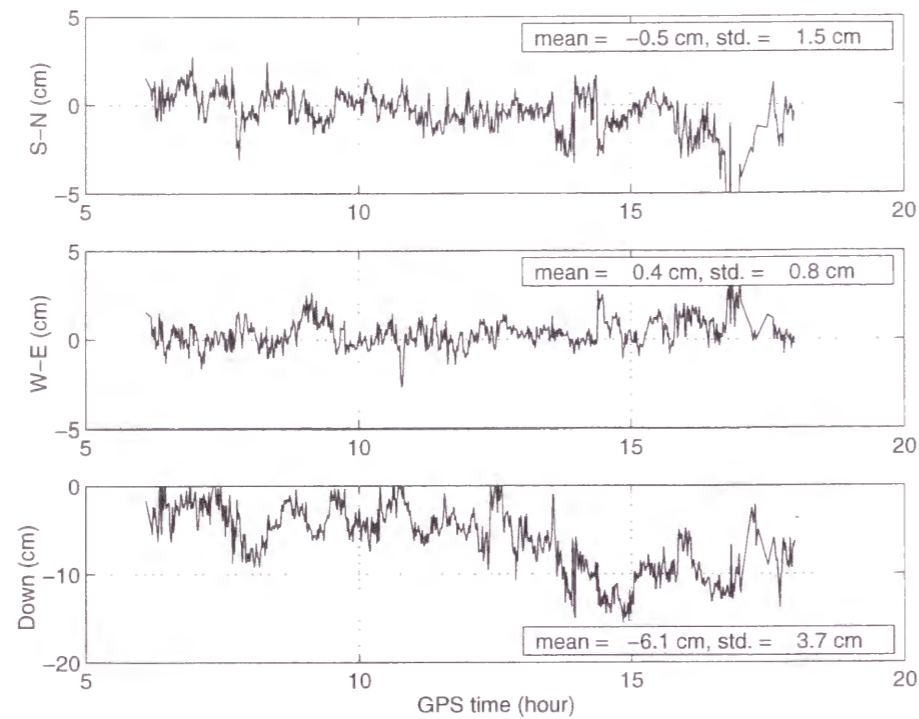


Fig.3-2e Errors of ionospheric-free KGPS solution (Minamiizu - Kozujima, 56.695km)

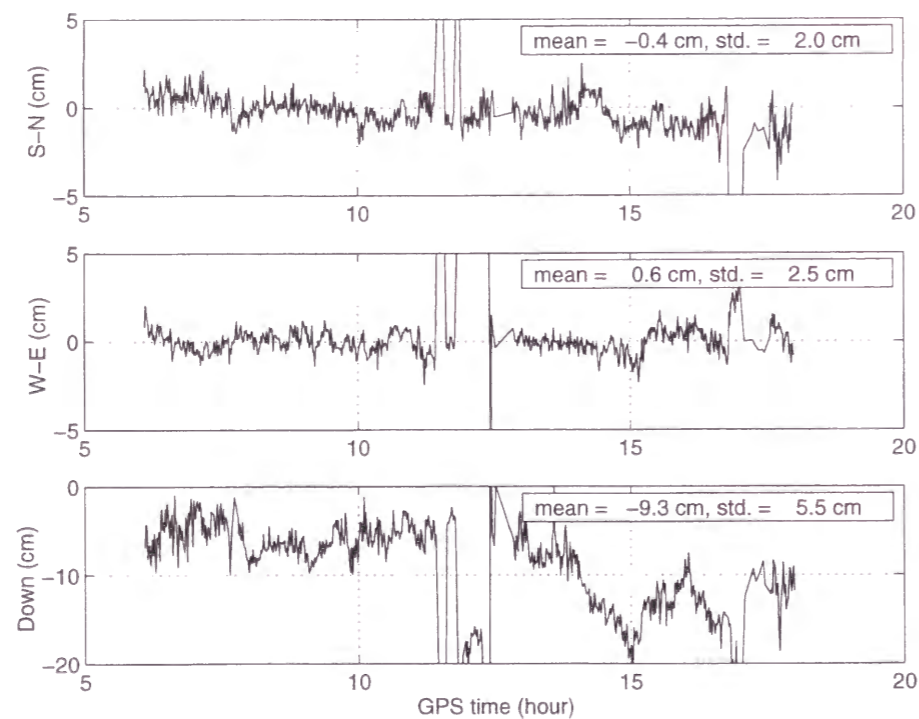


Fig.3-2f Errors of ionospheric-free KGPS solution (Minamiizu - Miyakeizu, 84.029km)

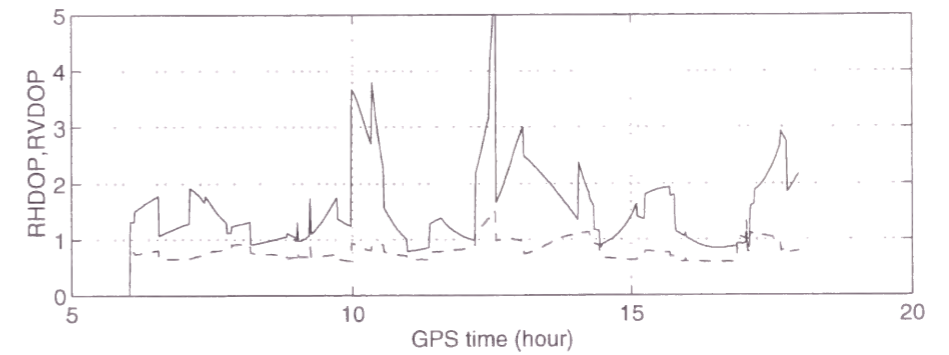


Fig.3-3 Variation of RHDOP and RVDOP (Dashed line is RHDOP and solid line is RVDOP)

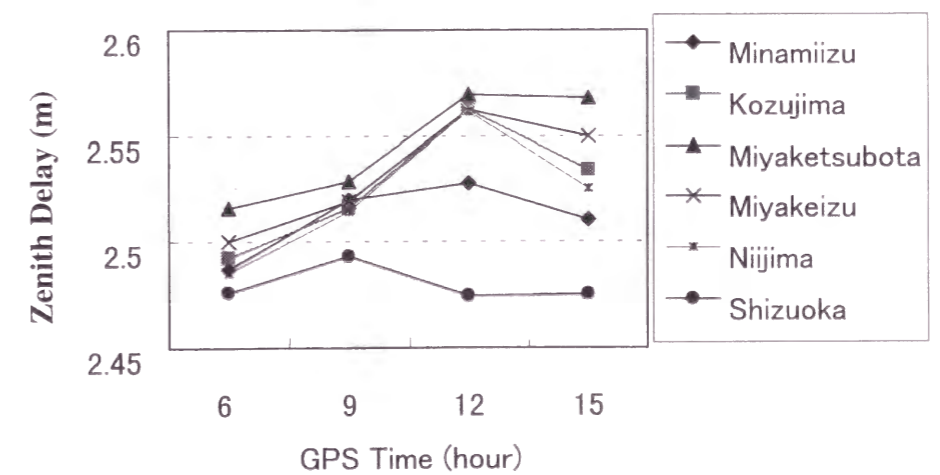


Fig.3-4 Position error caused by estimation error of zenith delay

3.1.2 Error Sources

The GPS positioning accuracy is mainly affected by the tropospheric propagation delay, ionospheric propagation delay, ephemeris error, and multipath error. The effects of these error sources will be discussed in order in this section.

First, the tropospheric delay caused by dry atmosphere depends only on the temperature and the atmospheric pressure at the ground, and its magnitude can be calculated with an accuracy in millimeter order. On the other hand, it is difficult to estimate the propagation delay caused by vapor because it strongly depends on the weather. Hence, around 90% of tropospheric delay is removed in general by adopting a tropospheric delay model (Spilker, 1996a). Though the tropospheric delay is calculated by multiplying the estimated zenith delay by a mapping function, the model accuracy depends mainly on the estimation accuracy of the zenith delay. Since the zenith delay depends on atmospheric vapor, precise meteorological data is necessary to improve the estimation accuracy. In these kinematic analyses, the accuracy is not sufficient because we adopted standard values as the meteorological data. On the other hand in the static analyses with GAMIT, the zenith delay was estimated every three hours (MIT, 1995). Fig.3-4 shows the time variation of estimated zenith delay. The differences of estimates between the observation sites were increasing with time. This seems to be due to the change of meteorological conditions after sunset. Note that the zenith delay estimate of the Shizuoka site seems to change independently of the other sites. These variations of zenith delay were taken into account in the static survey with GAMIT while the fixed standard values were used in KGPS. And it can be seen that the horizontal position differences hold within 1cm for baselines No. 1-6 while the vertical position differences increase according to the baseline length and reaches 9cm in baseline No.6. Therefore, the position differences shown in Fig.3-2 would be mainly caused by the tropospheric delay effect in KGPS positioning because the tropospheric delay mainly affects the vertical position.

Furthermore, the tendencies of vertical position variations for baselines No. 5 and 6 (Fig.3-2e,f) are similar, which may be due to the meteorological condition of Minamiizu sites included in both baselines. In fact, we cannot see a similar tendency in other baselines.

Then we simulate the tropospheric delay effect on positioning. Fig.3-5 shows the position errors assuming that the zenith delay for the reference site is correct and that of the estimation site contains 1, 2, 3, and 4cm errors. These values are calculated substituting the double difference of assumed tropospheric error into $\delta\mathbf{y}$ in Eq. (2.4-6) in which $(H^T C^{-1} H)^{-1} H^T C^{-1}$ is obtained using the real satellite constellation. It is obvious in Fig.3-5 that the tropospheric delay affects the vertical position estimate very much. The zenith delay estimate error of 1cm causes a bias error of around 2.5cm in the vertical position. This indicates that the zenith delay may differ around 1cm between the Miyakeizu and the Miyaketsubota sites even though they are on the same island, since the vertical position difference for baseline No.1 has around 2.3cm bias. One reason why the positioning accuracy degrades with increasing baseline length is that the difference in meteorological conditions between two sites would become larger with the baseline length.

Although the ionospheric delay does not affect the final solution for the dual frequency receivers, it will degrade the performance of the OTF. In this thesis, the ionospheric delay is not modeled because only 50% of delay can be estimated by the models if no other measurement sensor is used (Klobuchar, 1996; Spilker, 1996b), and inaccurate modeling rather affects the OTF performance. In order to evaluate the effect of ionospheric delay on positioning accuracy without the ionospheric modeling, the ionospheric signal described in Chapter 2.1.4 is used. The double differenced ionospheric signal is given as follows

$$\begin{aligned} \nabla\Delta\phi_I &= \nabla\Delta\phi_N - \nabla\Delta\phi_W \\ &= -2\nabla\Delta I + \lambda_N \nabla\Delta N_N - \lambda_W \nabla\Delta N_W + (\nabla\Delta d_{mN} - \nabla\Delta d_{mW}) + (\nabla\Delta\epsilon_N - \nabla\Delta\epsilon_W) \end{aligned} \quad (2.1-30)$$

From the above equation, the double difference ionospheric delay is calculated if the L1 and L2 ambiguities are correctly resolved, although it contains the multipath error and the observation noise which are around three times as large as for the L1 carrier phase.

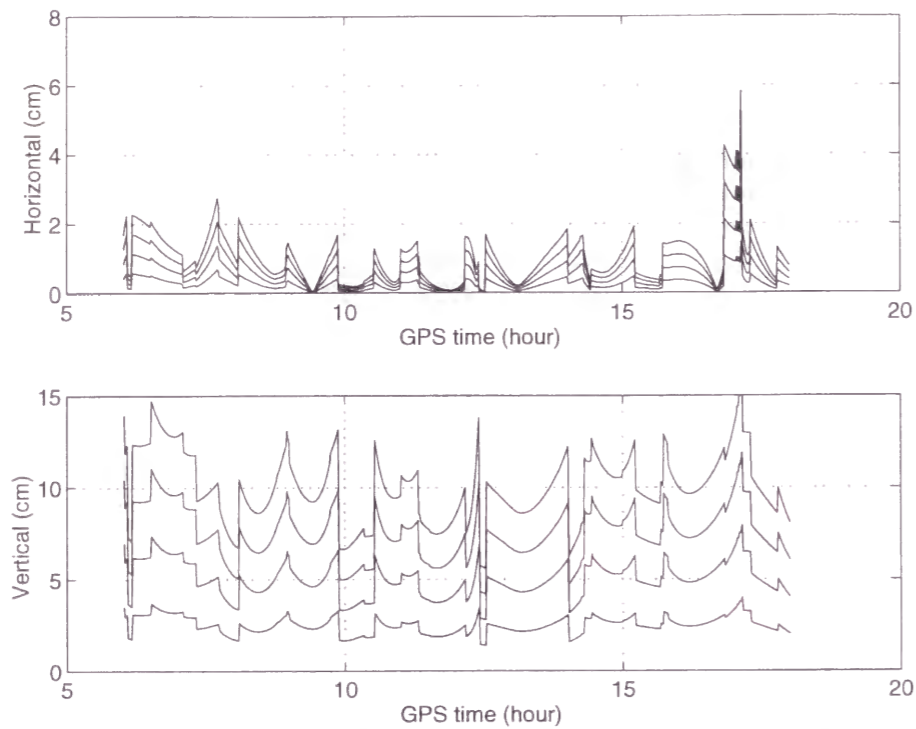


Fig.3-5 Horizontal and Vertical position errors assuming that the zenith delay for reference site is correct and that of estimation site contains 1, 2, 3, and 4cm errors

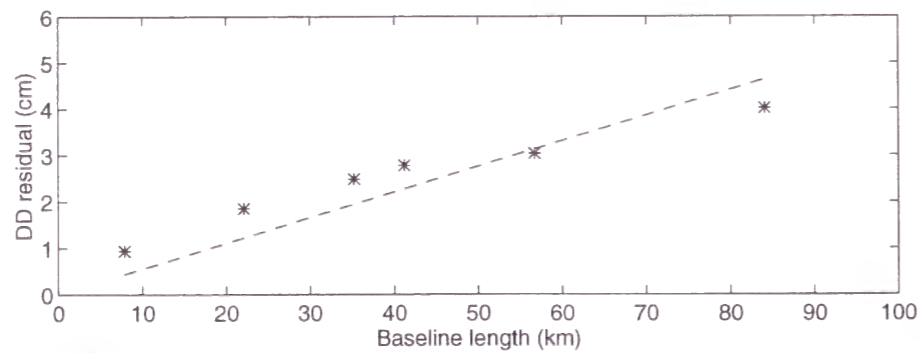


Fig.3-6 RMSs of the double differenced ionospheric errors for various baseline lengths

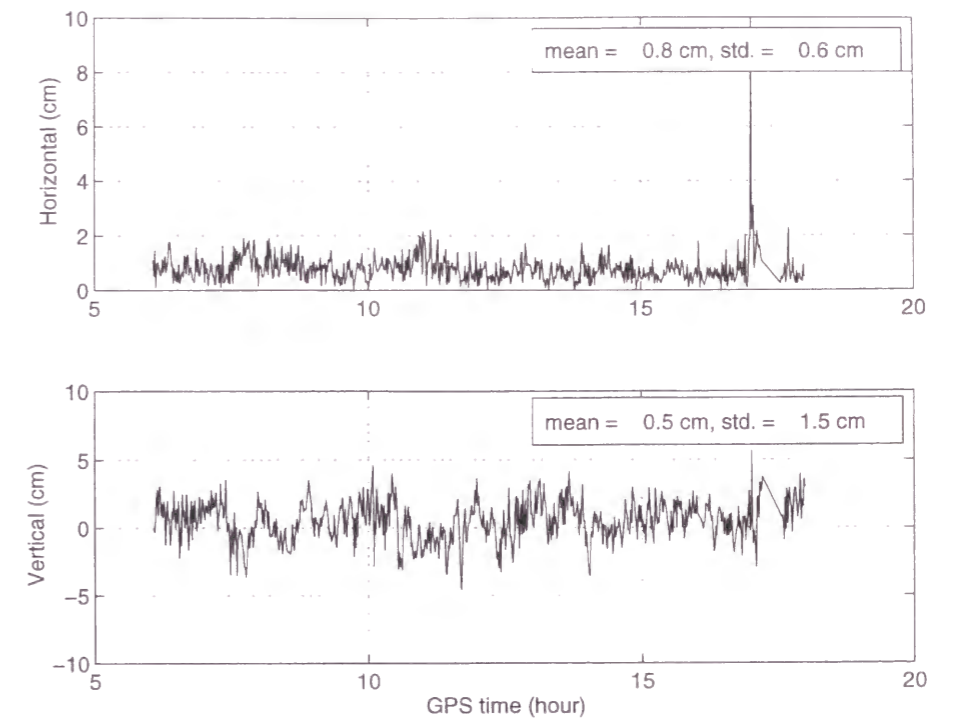


Fig.3-7a Horizontal and vertical position error caused by ionospheric delay (Miyakeizu - Miyaketsubota, 7.951km)

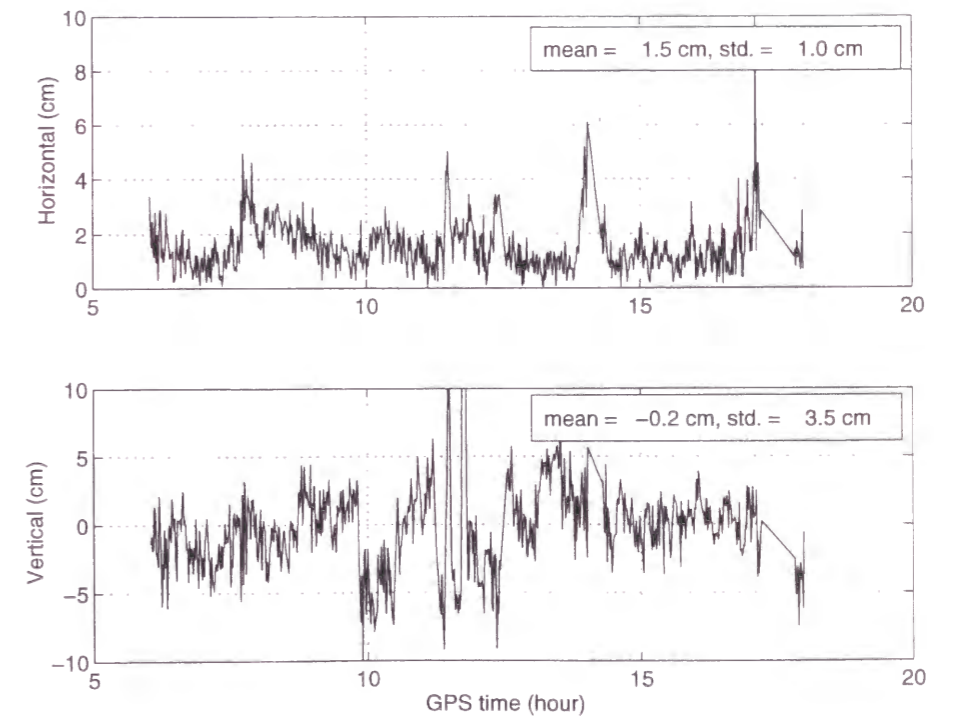


Fig.3-7b Horizontal and vertical position error caused by ionospheric delay (Niijima - Kozujima, 22.146km)

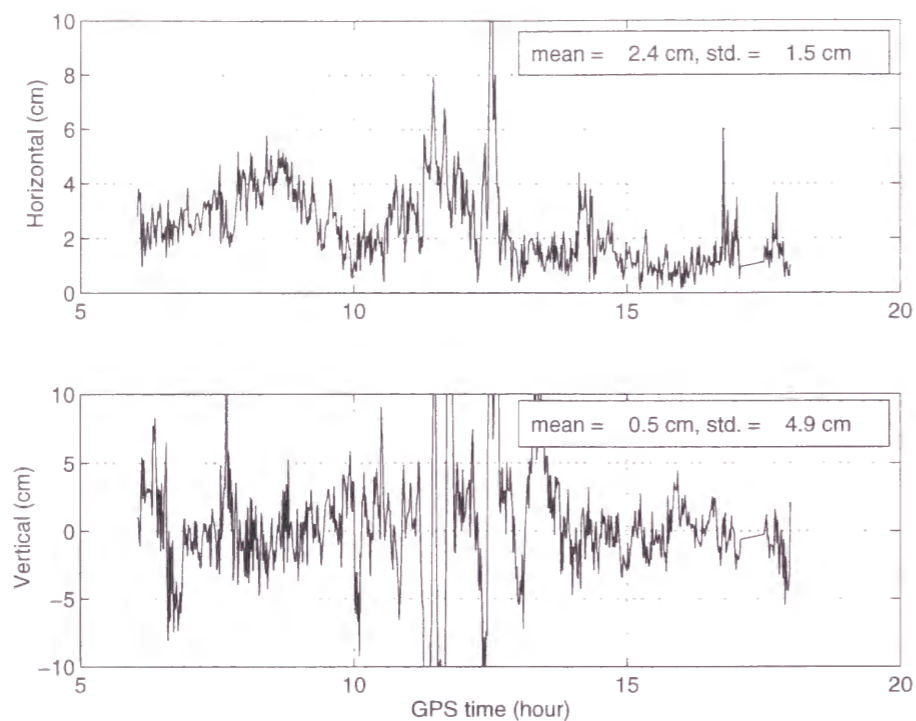


Fig.3-7c Horizontal and vertical position error caused by ionospheric delay (Miyakeizu - Kozujima, 35.182km)

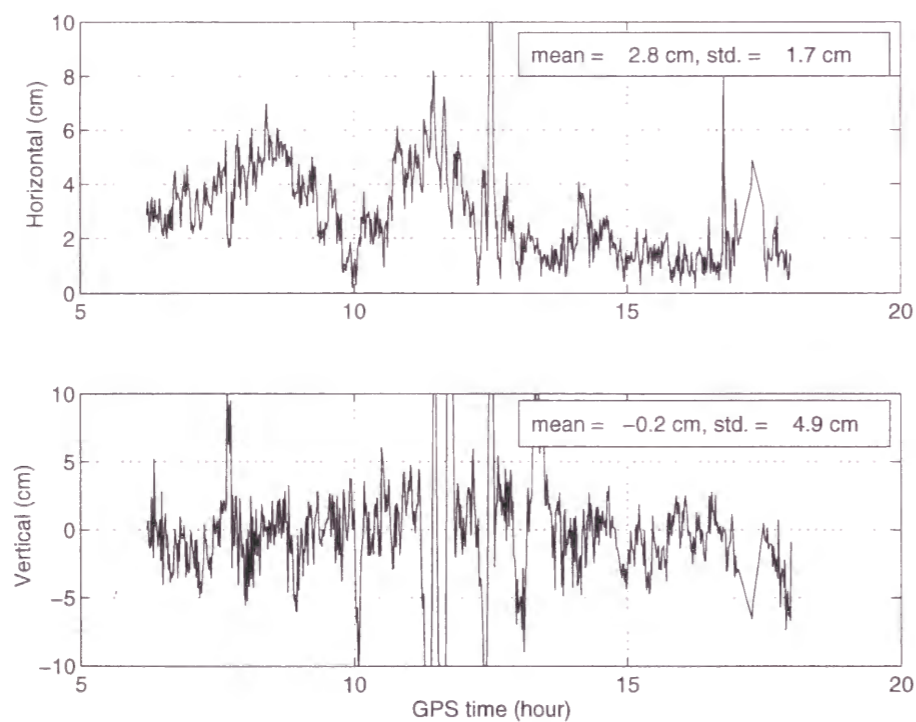


Fig.3-7d Horizontal and vertical position error caused by ionospheric delay (Miyaketsubota - Kozujima, 41.173km)

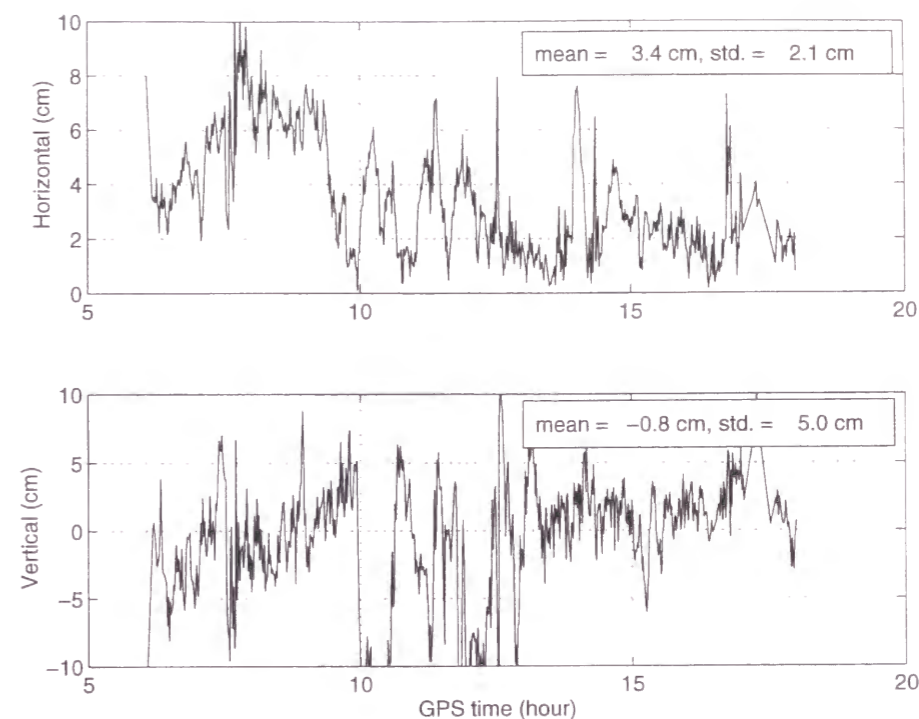


Fig.3-7e Horizontal and vertical position error caused by ionospheric delay (Minamiizu - Kozujima, 56.695km)

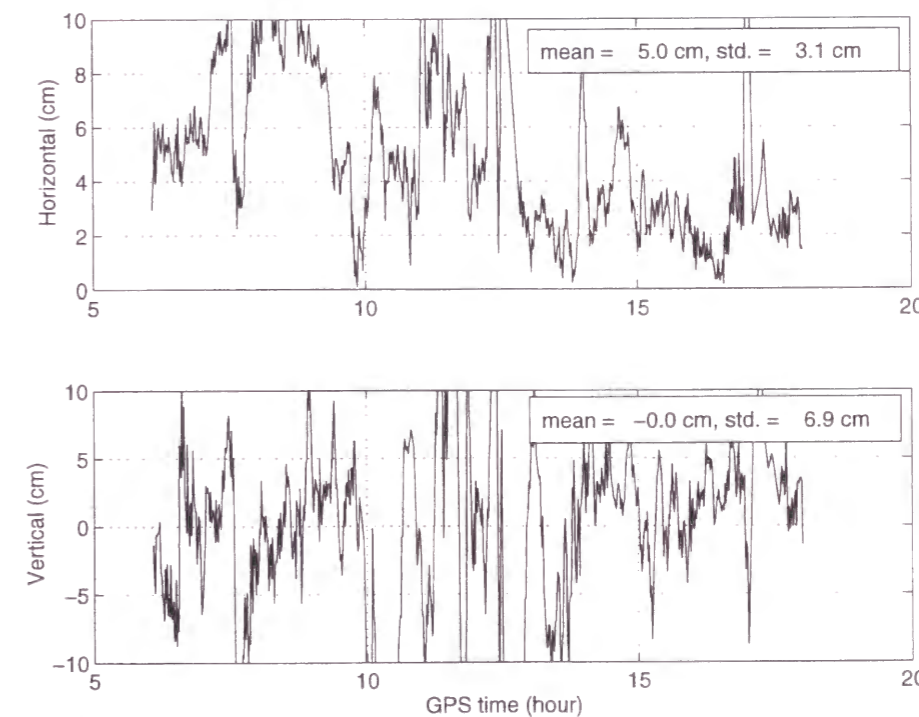


Fig.3-7f Horizontal and vertical position error caused by ionospheric delay (Minamiizu - Miyakeizu, 84.029km)

Fig.3-6 shows the RMS values of $\nabla\Delta I$ for baselines No.1-6 calculated by using Eq. (2.1-30). They would be approximately expressed by a function of the baseline length in the following equation

$$\overline{\nabla\Delta I}(cm) \cong 5.5 \cdot \left(\frac{l(km)}{100} \right) \quad (3.1-1)$$

The positioning errors caused by $\nabla\Delta I$ are shown in Fig.3-7. Considering Eq. (2.2-3), they are the positioning errors of widelane solutions. The positioning error of the L1 solution is equivalent to the value of Eq. (3.1-1) multiplied by $-f_2/f_1 (= -60/77)$, namely 4.3. We calculate the RMS values of horizontal and vertical positioning error caused by ionospheric delay when the widelane observable was used, and show their dependence on baseline length in Fig.3-8. The approximated RMSs are given in the following equations:

$$\delta h_{ion,wide}(cm) \cong 7.3 \cdot \left(\frac{l(km)}{100} \right) \quad (3.1-2)$$

$$\delta v_{ion,wide}(cm) \cong 9.5 \cdot \left(\frac{l(km)}{100} \right) \quad (3.1-3)$$

Coefficients in the right side of the above equations are 5.7 and 7.4 for the L1 solution. Since these values are obtained by averaging the effect of ionospheric delay from 3:00 p.m. (in Japan Standard Time) to 3:00 a.m. of the next day, they vary depending on the observation time.

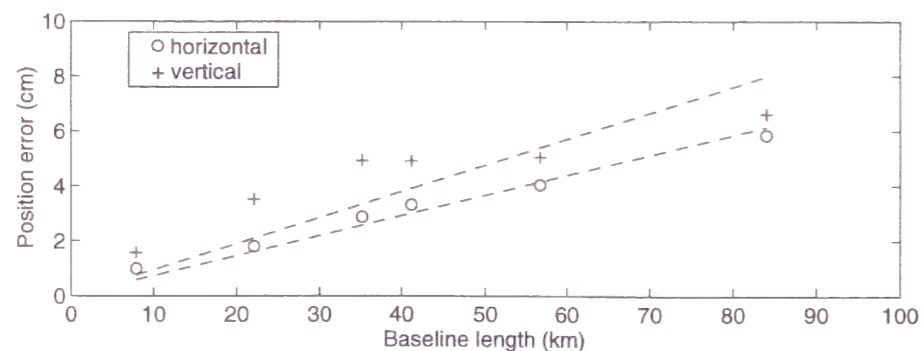


Fig.3-8 RMSs of the horizontal and vertical position errors caused by ionospheric delay

Next, we evaluate the effect of multipath on positioning accuracy. Multipath effect on the pseudorange is two orders of magnitude larger than on the carrier phase. It amounts to 15m even for a weak multipath signal whose relative amplitude is at -20db and sometimes to over a hundred meters when the relative amplitude of multipath is strong (Braasch 1996). In those cases, since it is almost impossible to resolve carrier phase ambiguities, multipath errors should be mitigated by using an antenna with a groundplane, or changing the location of the antenna. Also, the multipath effect on the carrier phase degrades the performance of OTF. Even when the ambiguities are correctly resolved, the multipath error affects the positioning accuracy. We simply simulate the magnitude of multipath error for the carrier phase, assuming that there is only one reflected signal. The direct and reflected signals are given in simplified expressions

$$\begin{aligned} A_D &= A \cos \varphi_D \\ A_R &= \alpha A \cos(\varphi_D + \varphi) \end{aligned} \quad (3.1-4)$$

where A_D and A_R are amplitude of direct and reflected signals, and φ_D is the phase of the direct signal. α is a damping factor which ranges from 0 to 1 and φ is the phase shift of the reflected signal. The superposition of both signals gives

$$\begin{aligned} A_s &\cong A \cos \varphi_D + \alpha A \cos(\varphi_D + \varphi) \\ &= B \cos(\varphi_D + \Theta) \end{aligned} \quad (3.1-5)$$

where the resultant multipath error Θ is

$$\Theta = \arctan \left(\frac{\sin \varphi}{\alpha^{-1} + \cos \varphi} \right) \quad (3.1-6)$$

and the amplitude of superposed signal B is

$$B = A \sqrt{1 + \alpha^2 + 2\alpha \cos \varphi} \quad (3.1-7)$$

Eq. (3.1-4,5,6,7) are taken from (Seeber, 1993). The maximum multipath error is 90 degrees when $\alpha = 1$, i.e., the amplitude of the reflected signal is as strong as the direct signal. Therefore, the maximum errors in L1 and L2 carrier phase are about 5cm and 6cm respectively. Fig.3-9 shows the L1 and L2 carrier phase error for various damping factor $\alpha = 0.1, 0.3, 0.5, 0.7, 0.9, 0.9999$. The larger the damping factor, the larger the multipath error. Fig.3-10 shows the amplitude of superposed signal, B , for the same damping factor. The multipath errors for widelane, narrowlane, and ionospheric-free

observable are obtained by linearly combining the L1 and L2 multipath error, and are shown in Fig.3-11 (in meters) with respect to phase shift, ϕ (in meters). The RMSs of multipath errors are summarized in Table 3-2.

Table 3-2 Summary of multipath for various observables against the dumping factor. The signal strength of L2 carrier is assumed to be the same with L1 carrier.

α observable	0.1	0.3	0.5	0.7	0.9	0.9999
L1	0.2	0.6	1.1	1.6	2.2	2.7
L2	0.3	0.8	1.4	2.1	2.9	3.5
Widelane	1.4	4.1	7.1	10.3	14.3	17.4
Narrowlane	0.2	0.5	0.9	1.3	1.8	2.2
Ionospheric-free	0.7	2.1	3.6	5.2	7.2	8.8

(Units: cm)

It is very difficult to observe the multipath error separately from other errors such as the tropospheric delay and ionospheric delay. However, it can be seen by comparing the observed data on successive days for a very short baseline in which the propagation delays are negligible. Because the GPS satellites orbit the earth twice every sidereal day (23h 56m), they return to almost the same location four minutes earlier each day. Thus, errors thought to be multipath would show the same pattern between successive days. Some authors have reported that the multipath error shows typical periods of about 30 minutes due to the changing satellite geometry (Braasch 1996, Seeber 1993). The L1 carrier multipath error in these experiments would be thought to be less than 1cm (1σ) because antennas used were with groundplanes. Multipath error does not depend on the baseline length because it is due to the location of the antenna. If we extrapolate the fitting line in Fig.3-6 toward the zero baseline length, we would estimate the position error due to the multipath error and measurement noise. Considering the typical magnitude of noise to be 2~3mm (doubled in double difference), the multipath error is sufficiently reduced to a few millimeters by using the ground plane.

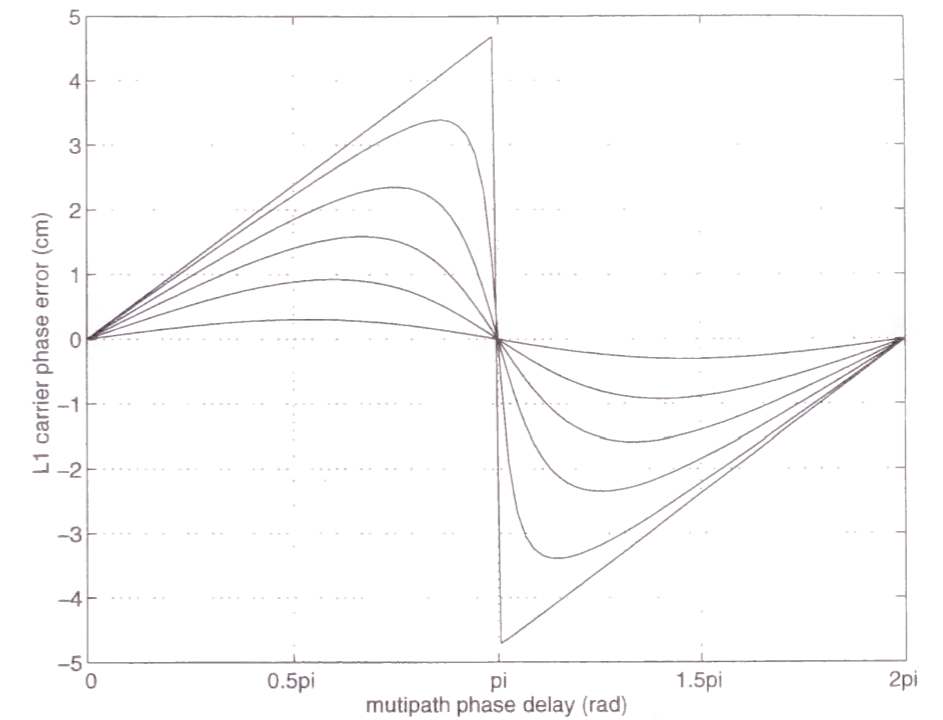


Fig.3-9a Multipath errors on L1 carrier phase for various damping factors

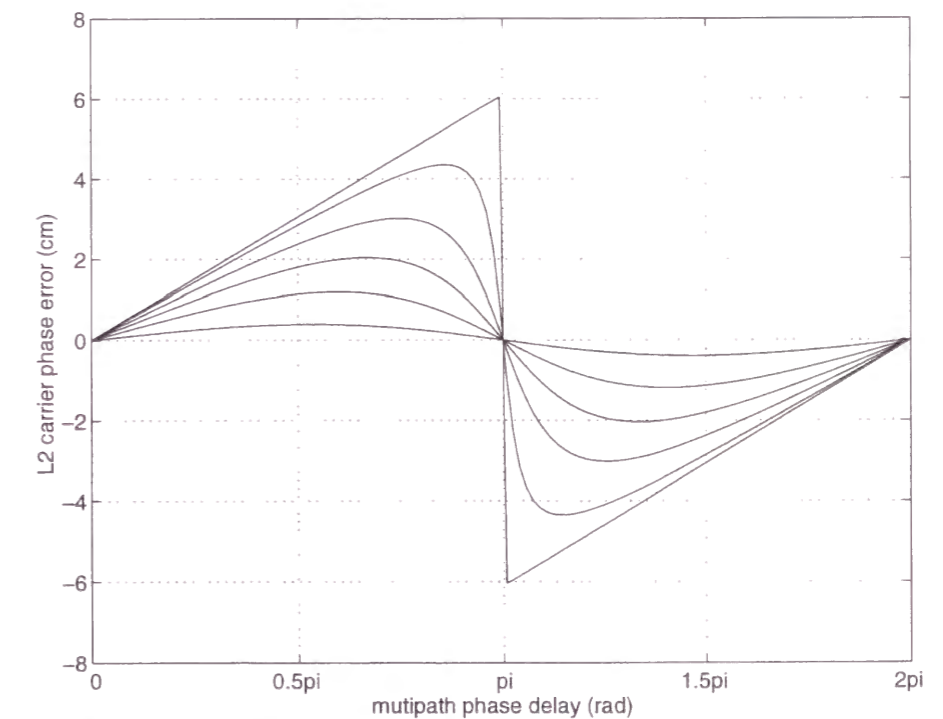


Fig.3-9b Multipath errors on L2 carrier phase for various damping factors

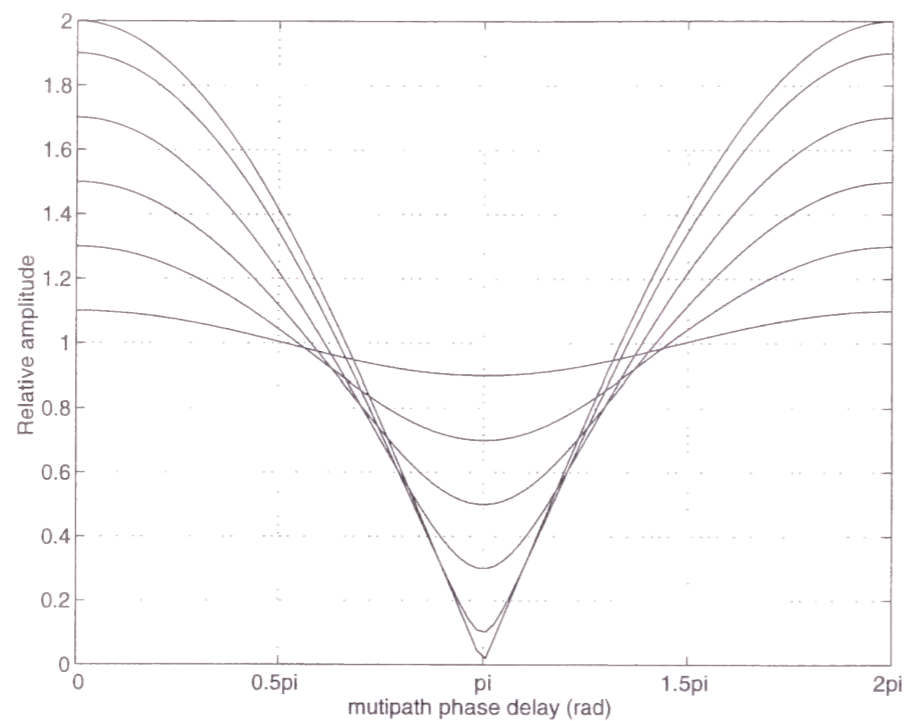


Fig.3-10 Amplitude of superposed signal for the damping factor same with Fig.3-9

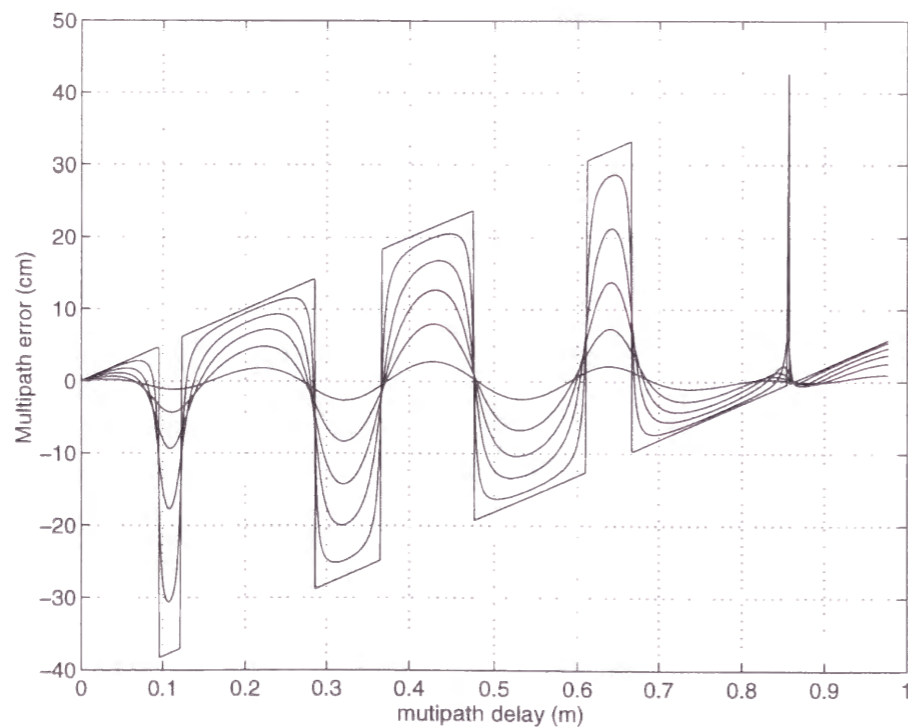


Fig.3-11a Multipath errors on widelane observable

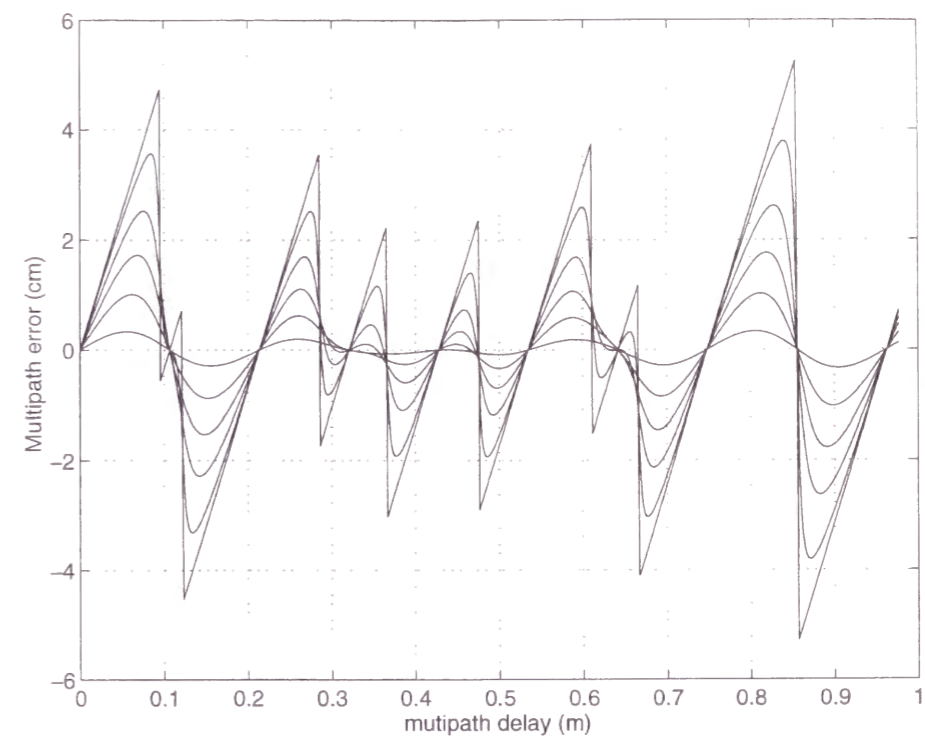


Fig.3-11b Multipath errors on narrowlane observable

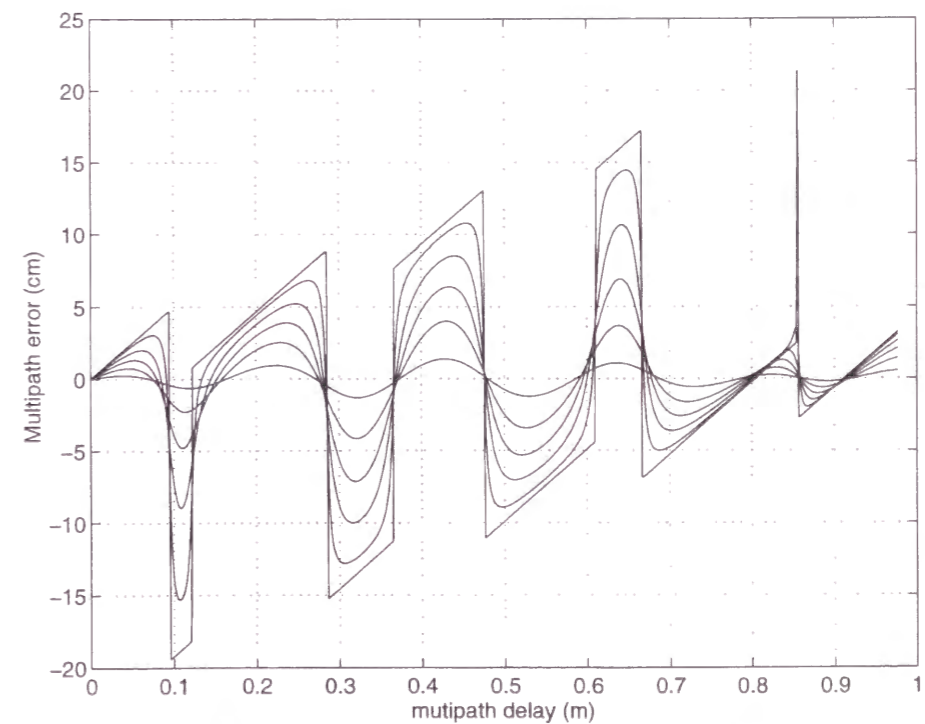


Fig.3-11c Multipath errors on ionospheric-free observable

Furthermore, we evaluate the effect of broadcast ephemeris error on positioning accuracy for various baseline lengths. Though the precise or predicted precise ephemeris will be used nominally for this kind of analyses, it is worthy to consider the broadcast ephemeris because it can be obtained in real time aboard. The differences between broadcast ephemeris and precise ephemeris in this experiment are shown in Fig.3-12, which are defined as broadcast ephemeris error here and about 30m in RMS. Fig.3-13 shows the variation of double differenced ephemeris error. The larger the baseline length, the larger the ephemeris error. The RMSs of double differenced ephemeris errors depending on baseline length are shown in Fig.3-14 and are calculated approximately by the following equation

$$\overline{\nabla \Delta d_{eph}}(cm) \cong 3.5 \cdot \left(\frac{l(km)}{100} \right) \quad (3.1-8)$$

The horizontal and vertical positioning error caused by ephemeris error are shown in Fig.3-15 and their RMSs are shown in Fig.3-16. The least squares fittings of them give the estimates of positioning error in horizontal and vertical direction as follows:

$$\delta h_{eph}(cm) \cong 4.3 \cdot \left(\frac{l(km)}{100} \right) \quad (3.1-9)$$

$$\delta v_{eph}(cm) \cong 6.0 \cdot \left(\frac{l(km)}{100} \right) \quad (3.1-10)$$

Finally, the error budget for kinematic positioning is shown in Table 3-3. And the factors of positioning error for other observables relative to the L1 positioning error are summarized in Table 3-4, in which the signal amplitude and the measurement noise of the L2 carrier phase are assumed to be the same as those of the L1 carrier phase.

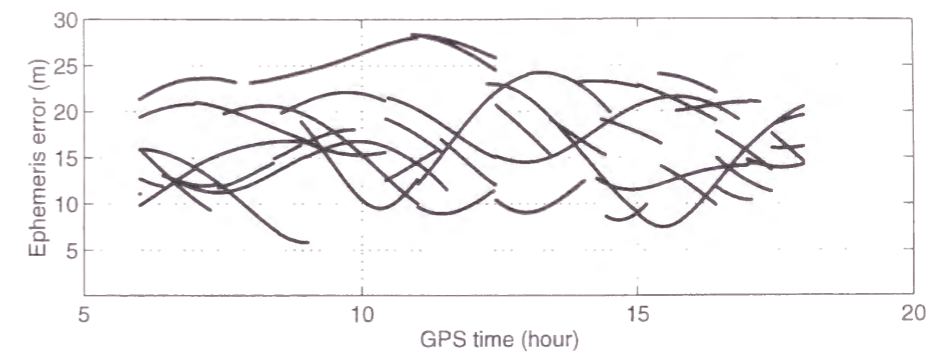


Fig.3-12 Differences between broadcast and precise ephemeris

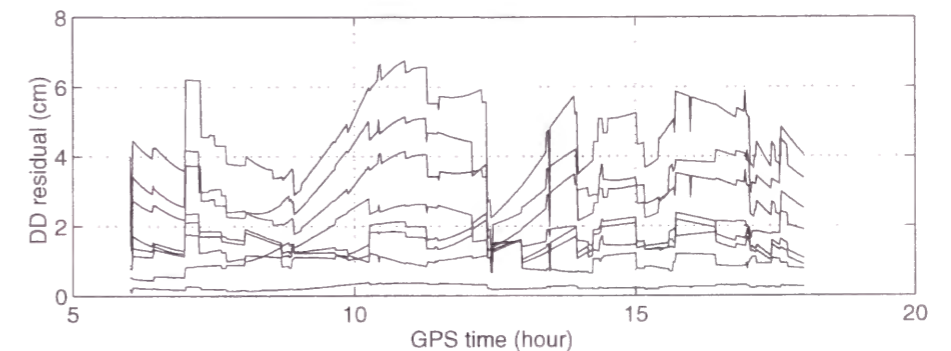


Fig.3-13 Time variation of double difference of the orbit difference (Baseline No.1-8)

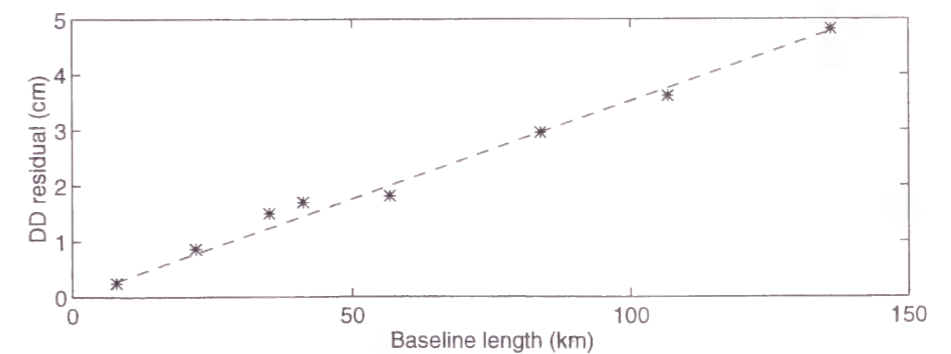


Fig.3-14 RMSs of the double differenced orbit errors depending on the baseline length

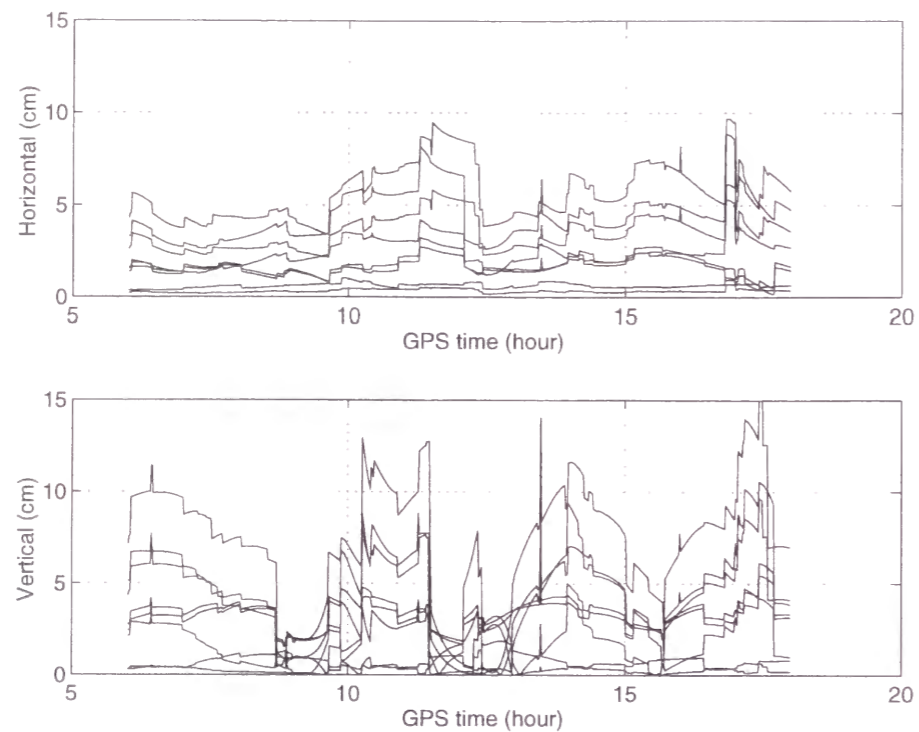


Fig.3-15 Position error caused by broadcast ephemeris error (Baseline No.1-8)

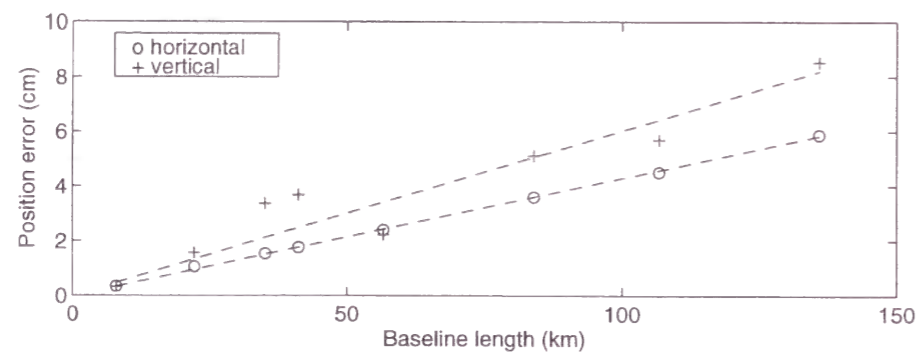


Fig.3-16 RMSs of the horizontal and vertical position errors caused by broadcast ephemeris error (Baseline No.1-8)

Table 3-3 Kinematic GPS error budget

Error Source	Double Differenced Error (cm)	Horizontal Position Error (cm)	Vertical Position Error (cm)	Note
Tropospheric Delay	1.0	0.3	2.5	Estimation error of zenith delay is assumed to be 1cm.
Ionospheric Delay	$4.1 \cdot (l/100)$	$5.7 \cdot (l/100)$	$7.4 \cdot (l/100)$	Values for L1 carrier phase. l is baseline length (km).
Multipath	< 1.0	$< 1.0 \cdot \text{HDOP}$	$< 1.0 \cdot \text{VDOP}$	Values for L1 carrier phase.
Broadcast Ephemeris	$3.5 \cdot (l/100)$	$4.3 \cdot (l/100)$	$6.0 \cdot (l/100)$	
Measurement Noise	6	$0.6 \cdot \text{HDOP}$	$0.6 \cdot \text{VDOP}$	Values for L1 carrier phase.

Table 3-4 Relative effect of GPS error sources on various observables

	Ionospheric-free	L1	Narrowlane	Widelane
Tropospheric Delay	1	1	1	1
Ionospheric Delay	0	1	1.3	1.3
Multipath	3.3	1	0.7	6.5
Broadcast Ephemeris	1	1	1	1
Measurement Noise	3.3	1	0.7	6.5

3.1.3 Positioning Accuracy Dependent on Baseline length

We summarize in Table 3-5 the positioning error of KGPS solutions when the L1, narrowlane, and widelane observables were used besides the ionospheric-free observable, and plot them against the baseline length in Fig.3-17. The precise ephemeris was used in kinematic positioning, and GAMIT solutions were used as the true positions. For baselines No.7 and 8, only the widelane positioning error is shown because the L1 ambiguity was not resolved for them.

Table 3-5 Accuracy of horizontal and vertical position estimated by KGPS (RMS)

Baseline	Ionospheric-free		L1		Narrowlane		Widelane	
	Horizontal	Vertical	Horizontal	Vertical	Horizontal	Vertical	Horizontal	Vertical
1	1.3	3.0	1.1	3.2	1.2	3.4	2.1	3.5
2	1.4	2.7	1.5	3.0	1.7	3.5	2.8	5.2
3	1.3	3.2	2.7	4.6	3.2	5.4	3.2	6.2
4	1.3	5.1	2.9	6.4	3.6	7.2	3.6	7.1
5	1.8	7.1	3.4	7.9	4.2	8.5	4.6	9.0
6	3.2	10.8	6.0	12.9	7.2	13.8	6.5	12.3
7	—	—	—	—	—	—	7.8	24.1
8	—	—	—	—	—	—	9.2	27.4

(Units: cm)

It can be seen from Table 3-5 that the fact the positioning errors differ from one another for each observable is mainly due to the effect of ionospheric delay. Actually, the position calculated by using the ionospheric-free observable is the most accurate solution in general. The vertical position error for baselines No.5 and 6 is worse than for shorter baselines. One possible reason is that those baselines contain the Minamiizu site that belongs to Izu Peninsula while other sites are on islands. Therefore, the solutions of baseline No.5 and 6 would be affected by tropospheric delays that may differ from each other according to the weather conditions in a land area and in an island area.

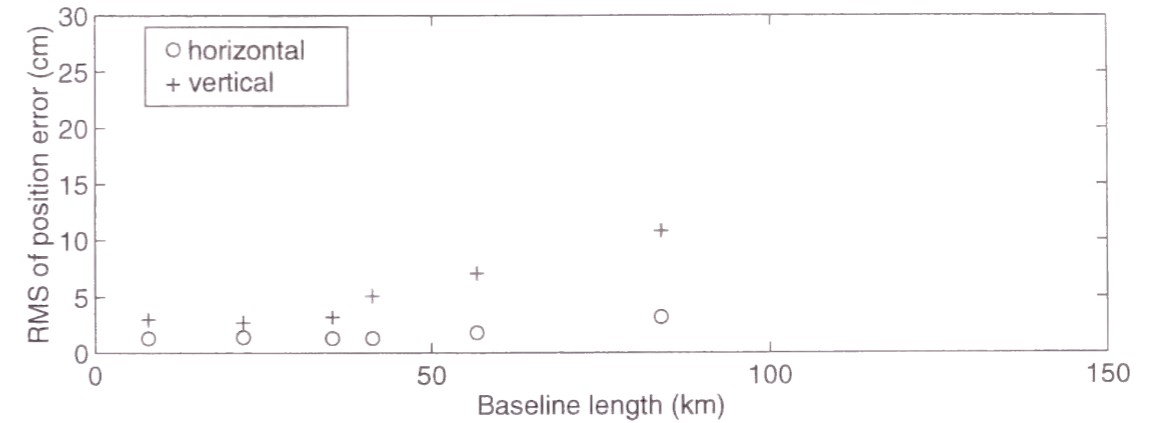


Fig.3-17a RMSs of the horizontal and vertical position errors when ionospheric-free observable was used (Baseline No. 1-6)

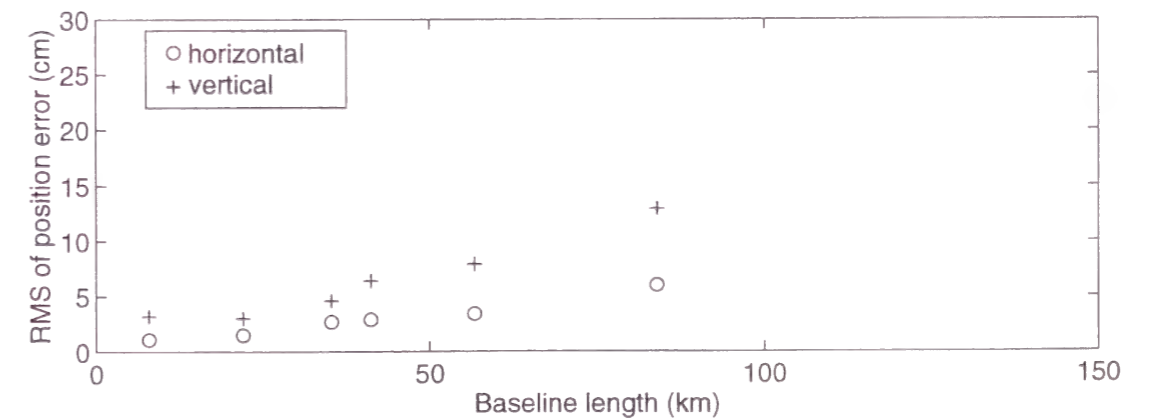


Fig.3-17b RMSs of the horizontal and vertical position errors when L1 carrier observable was used (Baseline No. 1-6)

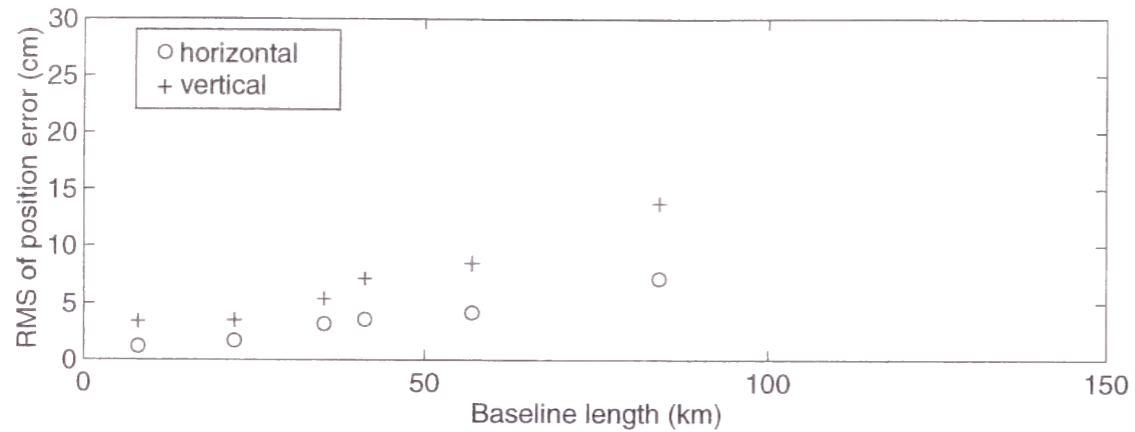


Fig.3-17c RMSs of the horizontal and vertical position errors when narrowlane observable was used (Baseline No. 1-6)

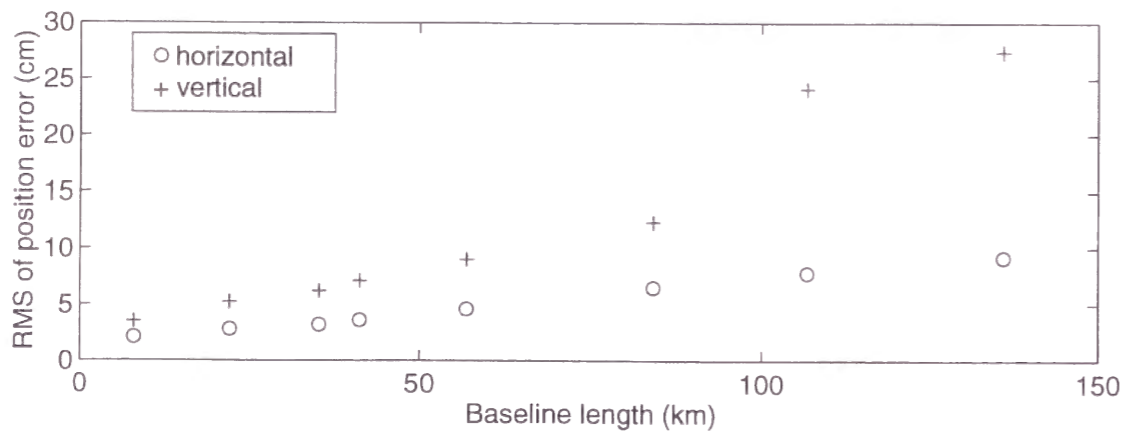


Fig.3-17d RMSs of the horizontal and vertical position errors when widelane observable was used (Baseline No. 1-6)

The variations of horizontal position are relatively small even in baselines No.5 and 6 because the tropospheric delay degrades horizontal positioning accuracy less than for the vertical direction. The ionospheric-free positioning errors in baselines No.1-4 are similar, while the positioning error for other observables increase in proportion to the baseline length. These are due to the ionospheric delay. Fig.3-18 shows the time variations of the L1, narrowlane, and widelane solutions for baseline No.3. Comparing the L1 positioning error in Fig.3-18a with the ionospheric-free positioning error in Fig.3-2c, the large fluctuation seen from 11 to 13 o'clock in Fig.3-18a can not be seen in Fig.3-2c. Hence, it is concluded that this large error in the L1 solution is caused by the ionospheric delay.

The accuracy of the narrowlane solution is better than the L1 solution for very short baseline length where the ionospheric delay is negligible, because the measurement noise of the narrowlane is smaller. In our experiments, the L1 solution is better than the narrowlane except for baseline No.1 because the effect of ionospheric delay on the narrowlane is amplified by a factor of $f_1 / f_2 (\cong 1.3)$ relative to the L1 carrier.

The widelane solution is inferior to other solutions because the multipath error and measurement noises are large. However, it has the advantage that the ambiguity of the widelane can be resolved correctly for a long baseline length of over 100km. Therefore, the widelane solution could be used for various kinds of applications, for example, the AirInSar (Airborne In Synthetic aperture radar) (Kimata, et. al., 1997), in which the precise repeat paths of aircraft are necessary.

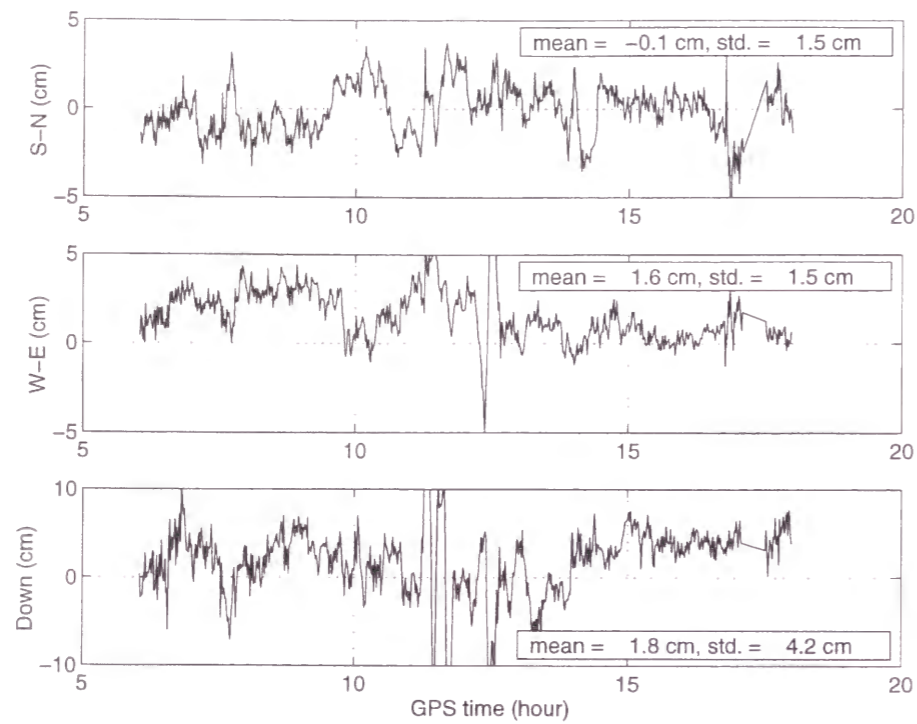


Fig.3-18a Position error in the baseline Miyakeizu - Kozujima (35.182km) when L1 carrier observable is used

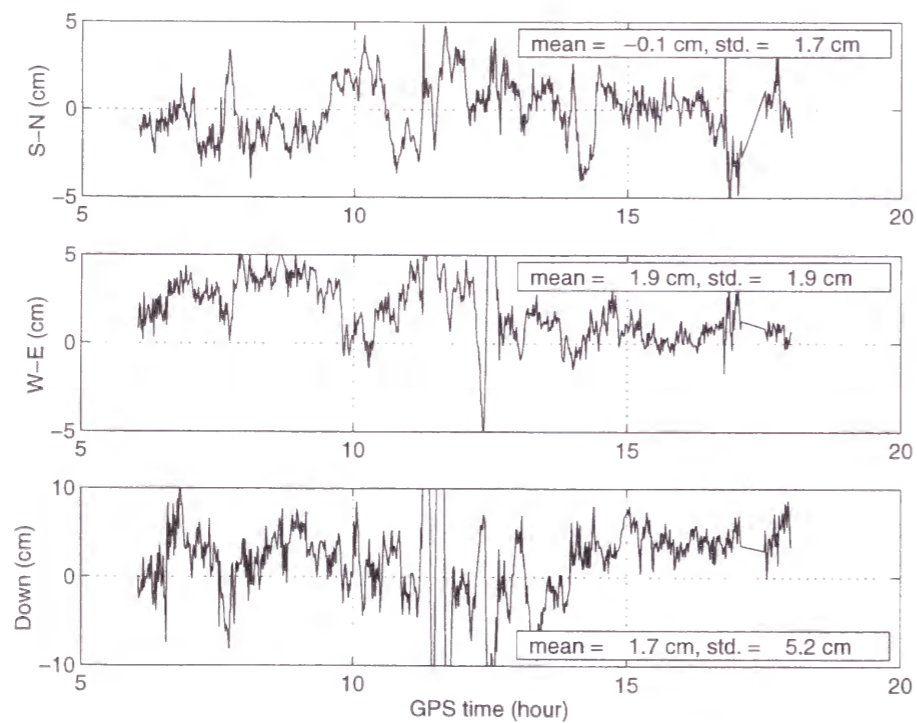


Fig.3-18b Position error in the baseline Miyakeizu - Kozujima (35.182km) when narrowlane observable is used

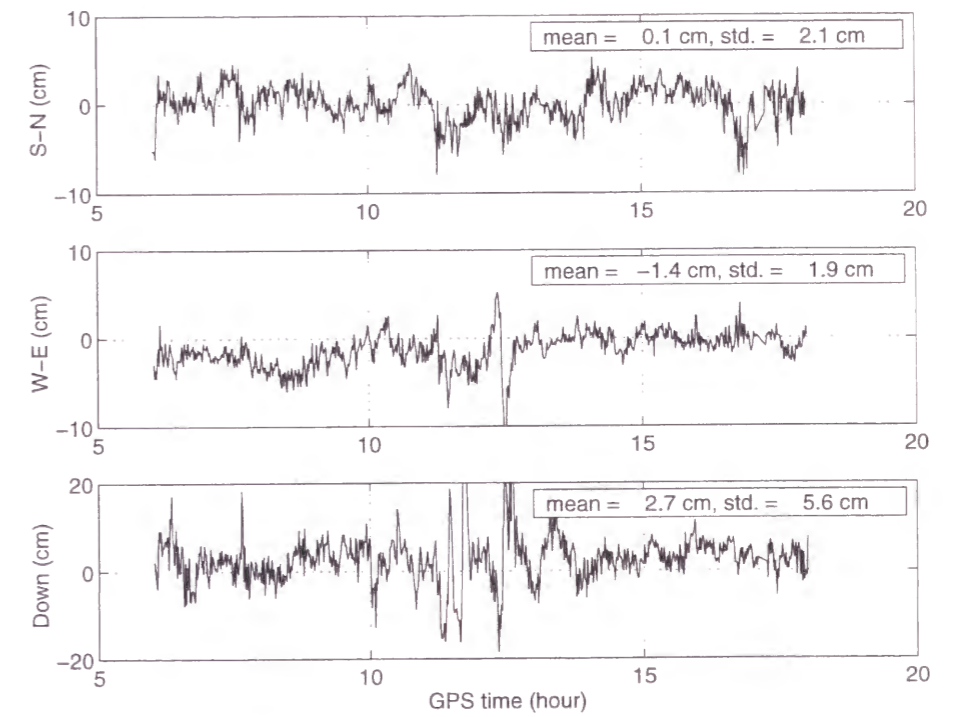


Fig.3-18c Position error in the baseline Miyakeizu - Kozujima (35.182km) when widelane observable is used

3.2 OTF Limit in Baseline Length

The dependence of OTF performance on baseline length will be evaluated in this section. Since the resolution of widelane ambiguity is easy for considerably long baselines (~ 100 km), we will estimate here the limit baseline length for OTF of L1 ambiguity. We should take into account several kinds of errors for OTF, such as multipath error, tropospheric delay, ionospheric delay, and ephemeris error if we use the broadcast ephemeris.

At first, we consider the test in measurement domain. Assuming that six satellites are observed, the degree of freedom is $6-4=2$, and $\chi_{2,0.05}^2/df = 3.0$ in Inequality (2.2-12) if we adopt 95% as the significant level. The sum of squared measurement residuals is calculated approximately by summing the double differenced errors in Table 3-3. Hence, Inequality (2.2-12) becomes as follows in this case

$$\sqrt{1^2 + 4 \cdot 1^2 \cdot (l/100)^2 + 1^2} > 3.0 \cdot 1 \quad (3.2-1)$$

where the first term on the left is the residual due to the tropospheric delay assuming that the difference of zenith delay estimate error between two sites is 1cm. The second term on the left is due to the ionospheric delay while the third term is the combined error of multipath and measurement noise that is assumed to be 1cm. On the right hand side, the parameter k_1^{L1} is set to 1. According to Eq. (3.2-1), the maximum baseline length in which the correct ambiguity will not be rejected is 62km. If we assumed the difference of zenith delay estimate error to be 2cm, and furthermore the ionospheric delay was as large as in the previous case, the limit baseline length for OTF would be 23km.

The test in positioning domain is considered next. Comparing Eq. (2.2-2) with (2.2-3), the effect of tropospheric delay on widelane and L1 measurement is the same. Therefore, its effect cancels if we take the difference between widelane solution and L1 solution. Since the multipath and noise are much smaller than the ionospheric delay, they can be omitted in this test. On the other hand, the effect of ionospheric delay on the position difference between widelane and L1 solutions is amplified by a factor of 2.3

because the signs of ionospheric error in measurements are opposite (see Eq. (2.2-2) and (2.2-3)). If the significant level of 95% is adopted in Inequality (2.2-13), i.e., $k_2^{L1} = 2$, and the RHDOP is set to 1.35, which is the average magnitude in this experiment, the ambiguity candidates which satisfy the following relation will be rejected.

$$\sqrt{(2.3 \cdot 5.7)^2 \cdot (l/100)^2} > 2 \cdot \sqrt{1^2 + 4^2} \cdot 1.35 \quad (3.2-2)$$

According to the above relation, the maximum baseline length, in which the correct candidate will not be rejected, is 82km. If the ionospheric delay becomes two times as large as in this case, the limit baseline length is 41km. Obviously, the test in positioning domain is effective over a wider area than in the case using the test in measurement domain. Moreover, the test in measurement domain is sensitive to the meteorological condition because its performance is affected by the tropospheric delay in addition to the ionospheric delay. In fact, if the difference of zenith delay estimate error reached 3cm, all of the ambiguity candidates would be rejected by the test in measurement domain (Eq. (3.2-1)). The limits to apply the tests in both domains are summarized in Table 3-6 for various meteorological conditions. Note that these experiments were conducted at night and the solar activity was intermediate. It is expected from Table 3-6 that the limit baseline length would be reduced to about 10km if the observations were conducted in the day at a period when the sun is extremely active.

Table 3-6 Limit of the ambiguity resolution on-the-fly in baseline length

Relative estimation error of zenith delay between stations (cm)	Ionospheric delay (factor to these tests)	Limit to apply the test in observation domain (km)		Limit to apply the test in position domain (km)
		Precise ephemeris	Broadcast ephemeris	
1	1	65	49	82
1	2	32	30	41
1	3	22	21	27
2	1	49	37	82
2	2	24	22	41
2	3	16	16	27

3.3 Detection of Crustal Movement due to an Earthquake

Finally in this chapter, we demonstrate the KGPS capability to observe the crustal movement due to an earthquake. The earthquake occurred in the sea near Kozujima at 12h43m (UTC) on 6th Oct. 1995, and its magnitude was 5.6. Fig.3-19 shows the ionospheric-free solutions for baselines No.2-5, in which the arrows show the time of the earthquake occurrence. The positioning accuracy of baseline No. 2-4 would be thought to be about 1.3cm horizontally according to the analyses of the previous day (Table 3-5). It can be seen from Fig.3-19 that Kozujima moved eastward by 2-3 cm, and this fact is consistent with the report of other authors. The movement was observed most remarkably in the baseline with Minamiizu (No.5). Although the movement before and after the earthquake can not be seen clearly in baseline No.4 and there is a bias error in the east-west direction, this may be caused by the peculiar weather of the Miyaketsubota site. On the other hand, movement in the vertical direction was not observed. We cannot judge whether or not the island moved in the vertical direction because the vertical positioning accuracy is not sufficient to detect a few centimeters of movement.

Recently, the predicted precise ephemeris are available via the Internet, which are published by the Jet Propulsion Laboratory, University of Bern, and so on. The accuracy is about 30cm for one day before prediction (Hatanaka, 1996a), while the ordinary broadcast ephemeris has errors of a few tens of meters. Therefore, the area where the KGPS was effective in real time would be larger if the predicted precise ephemeris were used. Furthermore, a dense GPS observation network which covers the whole of Japan has been established by the Geodetic Survey Institute (Hatanaka, 1996b). The network has 610 observation sites and the average distance between the sites is about 25km (April 1996). Thus, the use of such a dense network suggests the possibility of the real time monitoring of the crustal movement by the KGPS.

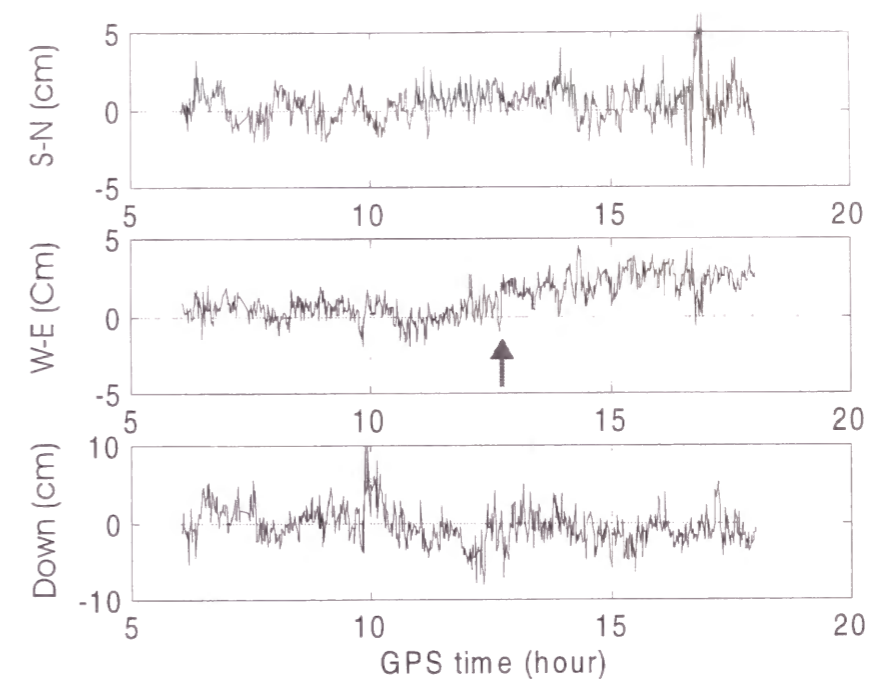


Fig.3-19a Position of Kozujima estimated by kinematic GPS before and after an earthquake that occurred at 12h43m, DOY279. (Niijima - Kozujima, 22.146km)

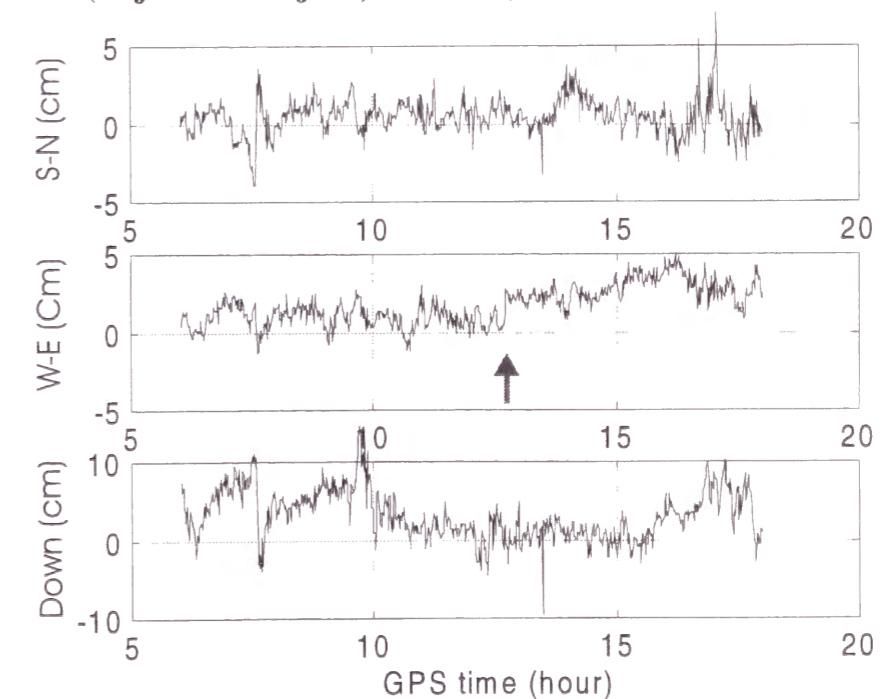


Fig.3-19b Position of Kozujima estimated by kinematic GPS before and after an earthquake (Miyakeizu - Kozujima, 35.182km)

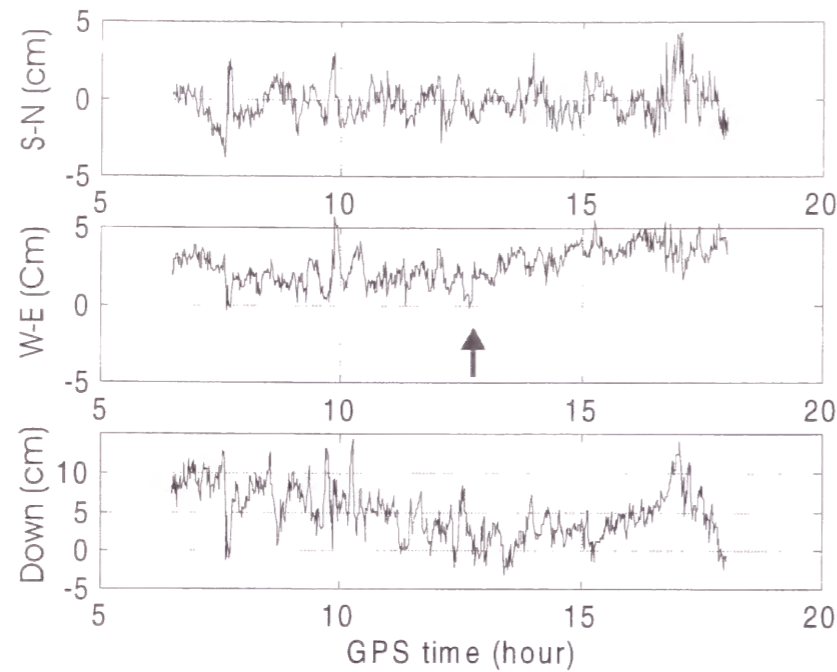


Fig.3-19c Position of Kozujima estimated by kinematic GPS before and after an earthquake (Miyaketsubota - Kozujima, 41.173km)

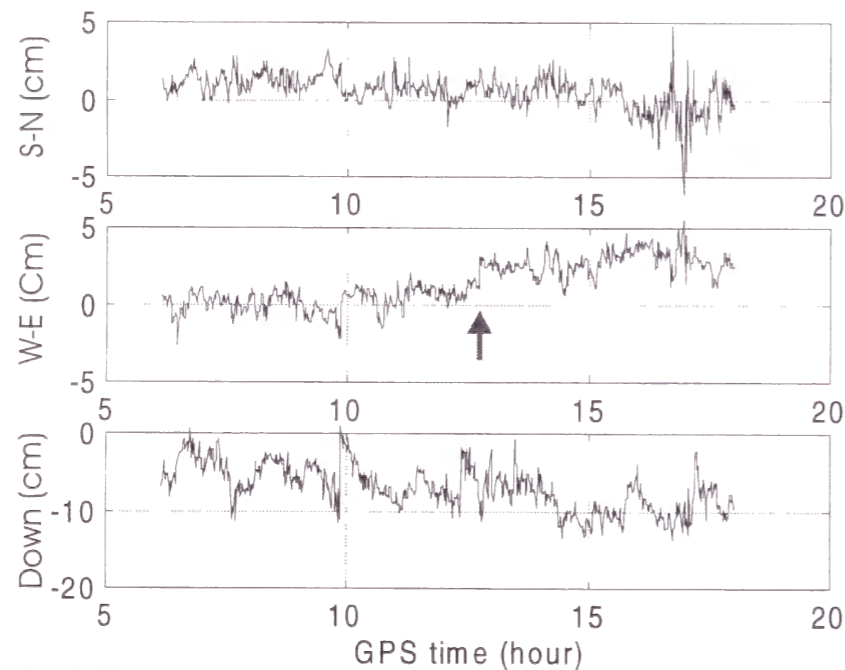


Fig.3-19d Position of Kozujima estimated by kinematic GPS before and after an earthquake (Minamiizu - Kozujima, 56.695km)

Chapter 4

Flight Tests and Results

A number of flight experiments have been conducted at NAL in order to evaluate the performance of the KGPS and the attitude determination where all of the analytical software have been developed by ourselves. In this chapter, we firstly evaluate the KGPS positioning accuracy of flying aircraft by several methods, then demonstrate the performance of OTF algorithm, and finally show the results of attitude determination including the estimate of aircraft structural flexure.

4.1 KGPS Positioning accuracy of aircraft in flight

We have already evaluated the KGPS positioning accuracy for static baselines in the previous chapter, i.e., around 1.5cm horizontally and 3.0cm vertically (1 sigma) when the baseline length is shorter than about 30km. Moreover, a comparison between our KGPS solution and the Ashtech PNAV solution showed agreement of better than 1cm (Kusaba, et. al., 1997). Hence, we guess the positioning accuracy of aircraft in flight would be in the same level if the correct ambiguity were resolved. It is very difficult to evaluate the positioning accuracy of aircraft in flight because there is no instrument to measure the position of moving bodies with an accuracy of 10cm or better. However, we will make effort to do so by some methods. At first, we will compare some kinds of kinematic solutions and show some evidences which support the theoretically estimated accuracy. Next, we will compare the KGPS solution with the positions estimated by the laser tracking system and DGPS/INS hybrid navigation system, though these comparisons seem to be the evaluation of the laser tracker and DGPS/INS rather than the evaluation of KGPS.

4.1.1 Flight Test Configuration

The flight experiment was conducted at the Sendai international airport on 7 Oct. 1993. Trimble 4000SSE dual frequency GPS receivers and the research aircraft, Do-228 (Fig.4-1), were used. One receiver was installed aboard the Do-228, and another was located at a ground monitor site in the airport. Fig.4-2 shows the ground monitor site, on which a Trimble Geodetic L1/L2 antenna was mounted. The antenna was with groundplane that mitigated the multipath error, and was connected to the reference GPS receiver in the monitor site as shown in Fig.4-3. The onboard receiver was connected to a Tecom MIL-E-5400 antenna mounted on the roof of the Do-228 cockpit (Fig.4-4). Applying interferometric surveying and laser theodolites, ground control points which include the locations of the monitor site and the runway thresholds were surveyed with respect to the WGS84 (Murata et. al., 1992b). Based on the results of this survey, the runway coordinate system (RCS) was defined and all positioning results were mapped onto this common RCS for trajectory comparison and assessment of positioning accuracy. Fig.4-5 shows the configuration of the flight experiments and the RCS coordinate system. The transmitter in Fig.4-2, 3,5 was used only for the experiments of real time DGPS/INS (Differential GPS and Inertial Navigation System) navigation to transmit the pseudorange correction data. The GPS measurements were recorded at a 2 Hz rate, and used for KGPS processing in post flight mode.

4.1.2 GPS-Estimated Flight Trajectory

In order to achieve high positioning accuracy using the carrier phase measurements, the ambiguity has to be resolved by some method. Although the OTF technique is very powerful and useful, a traditional method is used in this section. Namely, the initial and final positions of the aircraft are determined by an hour static survey, and those are used to determine the ambiguity. If new satellites are observed or cycle slips occur, the ambiguities of those satellites are determined from the antenna's position calculated using the satellites such that the corresponding ambiguities are known.



Fig.4-1 Research aircraft Do-228 and the laser tracker



Fig.4-2 Ground monitor site, on which a Trimble Geodetic L1/L2 antenna was mounted, and the antenna of transmitter

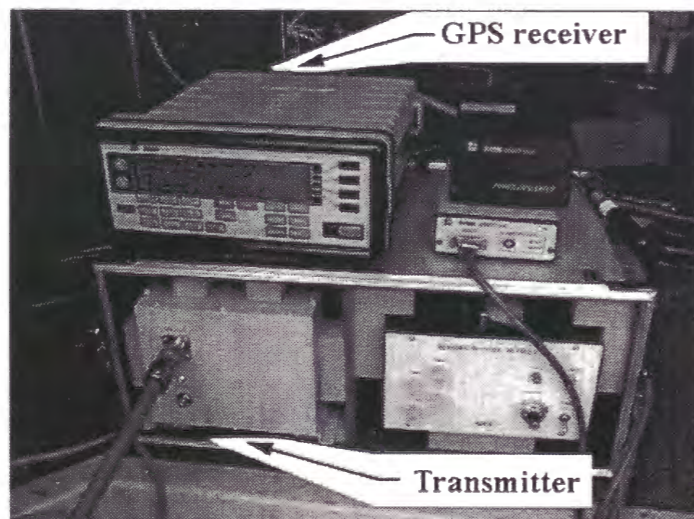


Fig.4-3 GPS receiver (Trimble 4000SSE) and the transmitter installed in the monitor site

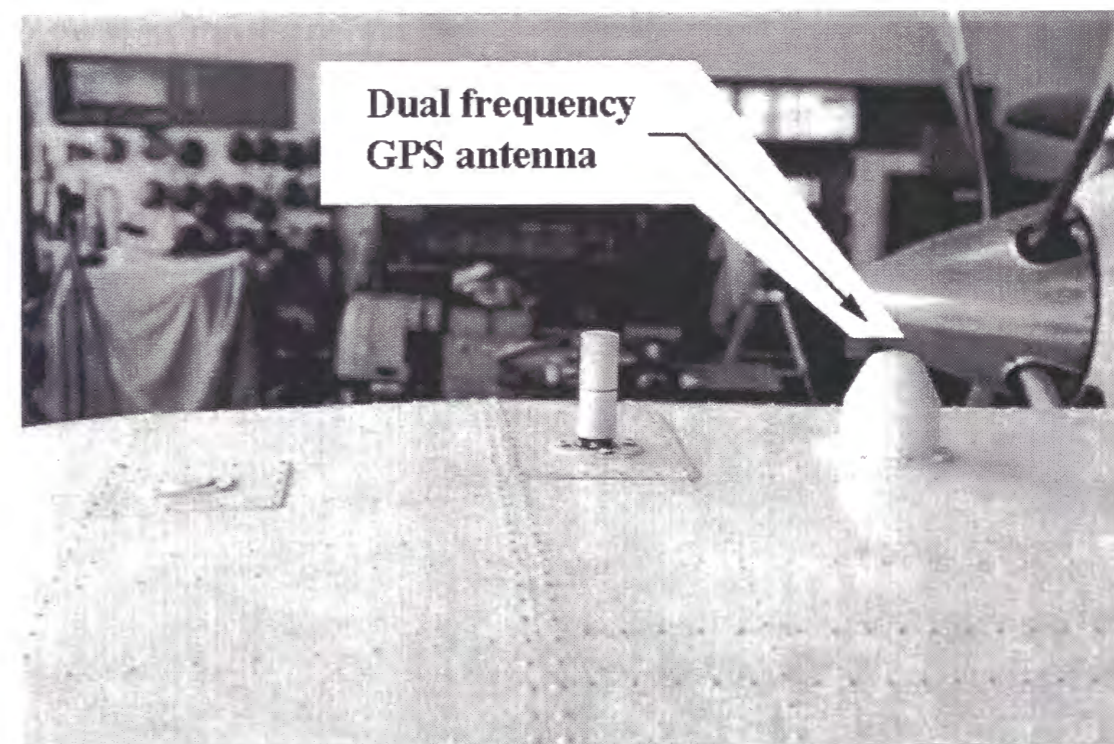


Fig.4-4 Dual frequency GPS antenna (Tecom MIL-E-5400) mounted on the roof of Do-228

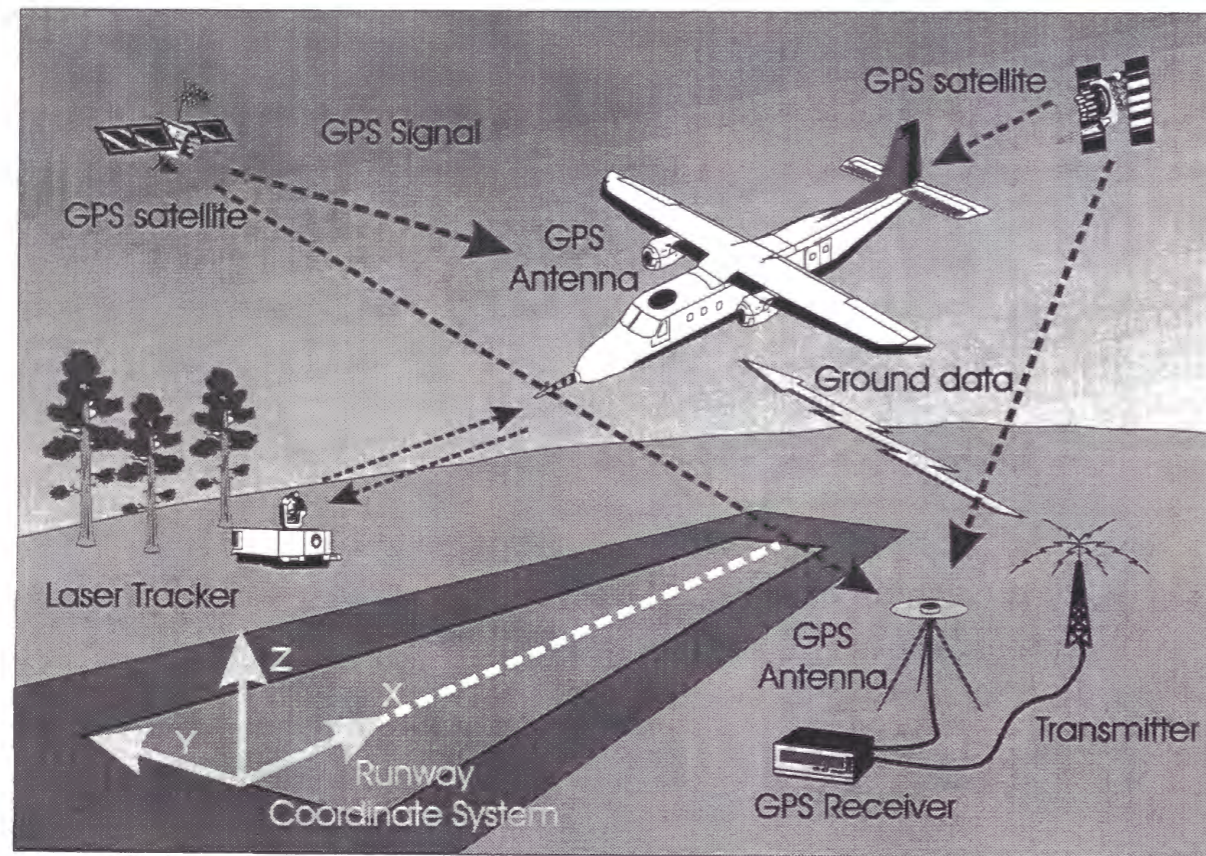


Fig.4-5 Flight test configuration and the RCS coordinate system

The ambiguities determined by this method will be available for the evaluation of the OTF performance later.

With these pre-determined ambiguities, aircraft positions are estimated by the least squares method or the extended Kalman filter whose states are position, velocity and accelerations (Tsujii and Murata, 1993a; Murata et. al., 1994). The flight trajectory are calculated for four cases, each differing in the treatment of the propagation delay. For land based application with short baseline length (up to some 20km), double differenced ionospheric and tropospheric delays are sufficiently small to achieve high positioning accuracy and to resolve ambiguities correctly. However, in the case of the aircraft positioning, the double and even double differenced tropospheric delay would not be so small as to be neglected even with a short baseline due to the strong height dependence of the tropospheric delay. Table 4-1 summarizes the cases tested.

Table 4-1: Models for the carrier phase observable

	model
Case 1	DD L1
Case 2	DD ionospheric-free
Case 3	DD ionospheric-free + trop. model
Case 4	TD ionospheric-free + trop. model

DD and TD denote double difference and triple difference phase data respectively. In cases 3 and 4, a tropospheric delay model is implemented based on the Saastamoinen model with CfA2.2 mapping function with pressure and temperature gradients considered. Fig.4-6 shows the estimated flight trajectory for case 1. Positions are in a runway coordinate system whose origin is at the threshold of the runway. The X-axis is along to the runway, and the Y-axis is perpendicular to the X-axis in the horizontal plane. Fig.4-7 shows the height profile.

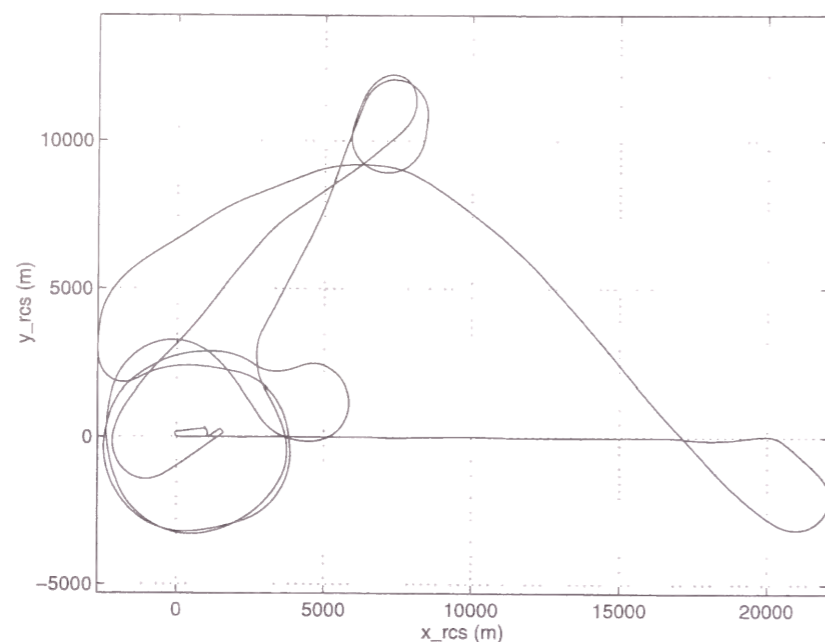


Fig.4-6 Horizontal trajectory of the aircraft

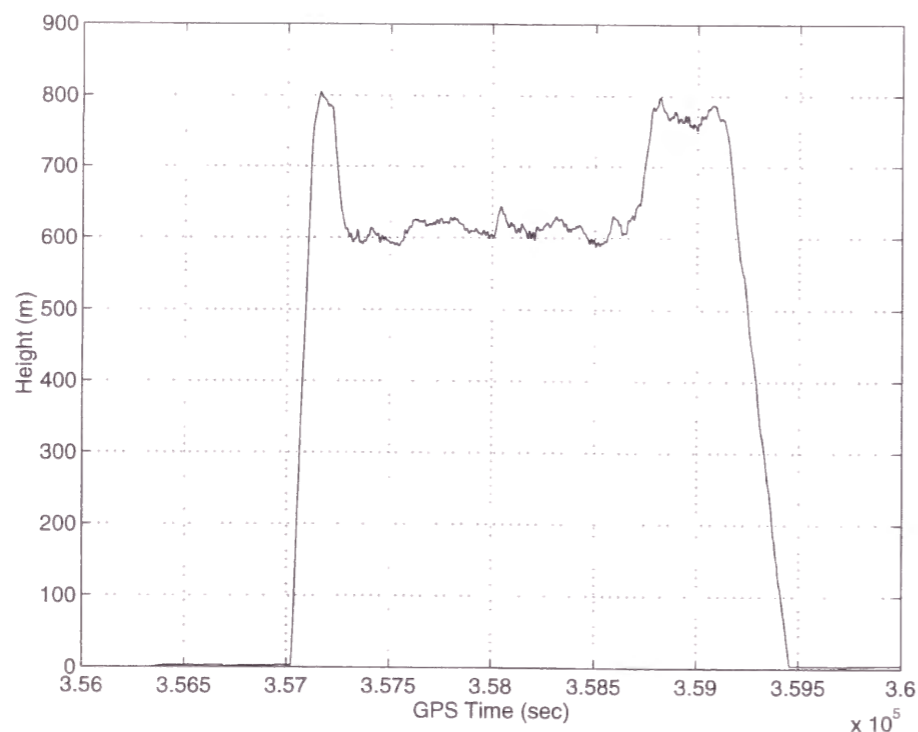


Fig.4-7 Height profile of the aircraft

The measurement residuals of primary satellites for case 2 are shown in Fig.4-8 where the satellite combinations are SV18-7, SV18-24, and SV18-29. Some jumps in Fig.4-8 are caused by appearance or disappearance of satellites. The residuals for case 2 are almost the same in trends as those for case 1, but are a little noisier due to the increase of noise level by the linear combination. Of interest is to note that the residuals are larger than the measurement noise level, and have some systematic trends. Compared with the height profile (Fig.4-7), it can be seen that the trends have correlation with the height difference between reference and onboard receivers. Fig.4-9 plots position differences (Case1 – Case 2) in each of three components resolved onto the RCS. Horizontal components agree well over the experiment within a few centimeters, but height differs to an extent of 20 cm at a maximum and about 10 cm (RMS). These errors are thought to be due to the ionospheric delay error that is included in Case 1.

In order to demonstrate the effect of implementing the tropospheric delay model, we show in Fig.4-10 the residuals with the modeling. Obviously, the systematic error seen in the Fig.4-8 no longer exists. Fig.4-11 shows the position difference with/without tropospheric delay modeling. Horizontal differences have slightly increased but height difference has significantly expanded especially over the dynamic flight phase at a maximum of larger than one meter and with a RMS of about 60 cm.

It seems that the flight trajectory for case 3 is the most accurate among cases 1-3, because the ionospheric-free observable was used and the tropospheric delay model was also implemented. In order to verify if this is true or not, the positioning for case 4 was executed. In case 4, aircraft positions were estimated by the least squares method. The triple difference of an epoch was the time difference between double difference of the epoch and that of the previous epoch. In this experiment the time interval is 0.5 sec. Since the aircraft position of an epoch was computed relative to the position of the previous epoch, positioning error of the previous epoch would propagate to the position of the present epoch. However the final aircraft position for case 4 agrees with values obtained by static survey in 5 cm horizontally and 10 cm vertically. Therefore, the estimated aircraft position for case 4 should have maintained the accuracy of this level. Fig.4-12 shows the position difference between case 3 and 4. Since the difference is a

few cm (RMS), it can be concluded that the trajectory for case 3 is accurate to within about 10 cm. This means that the ambiguity determined by the traditional method is reliably correct because even one cycle error in ambiguity during the flight would propagate to the position estimate and the final solution could not maintain such level of accuracy.

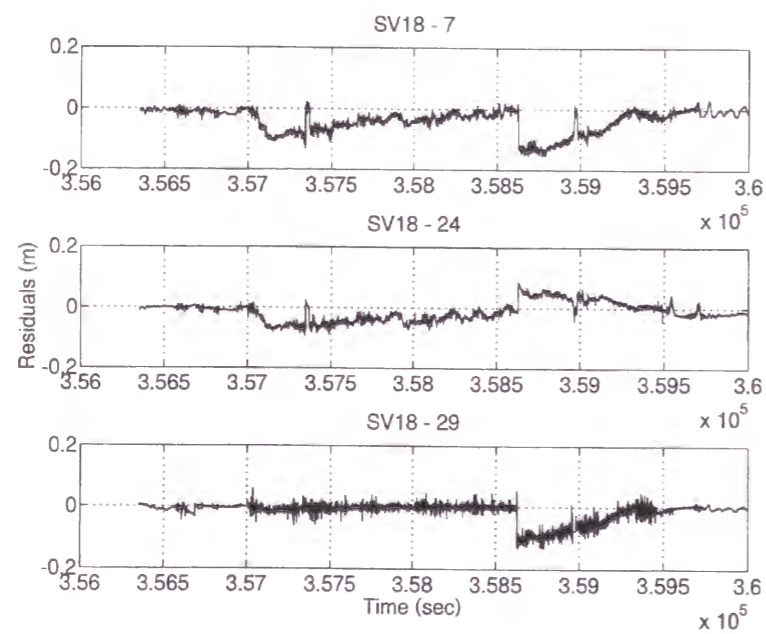


Fig.4-8 Measurement residuals of primary satellites for case 2

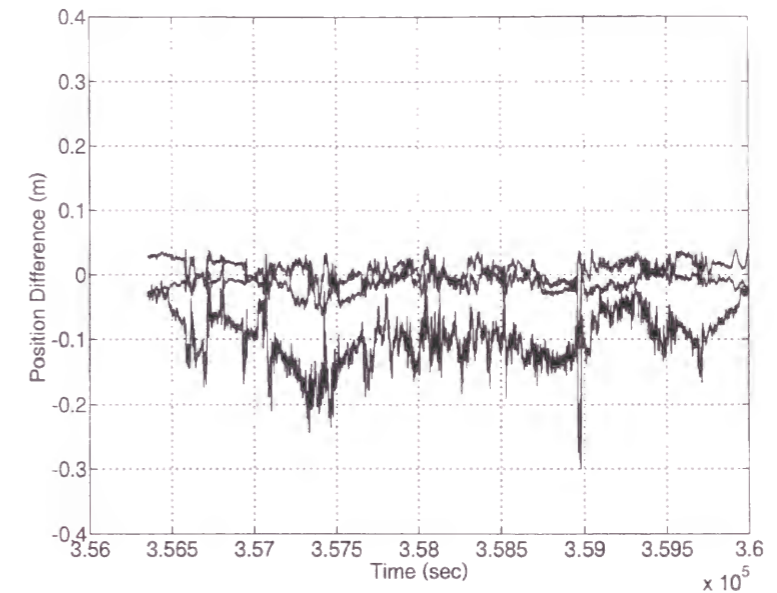


Fig.4-9 Position differences (Case1 - Case 2) in RCS coordinate

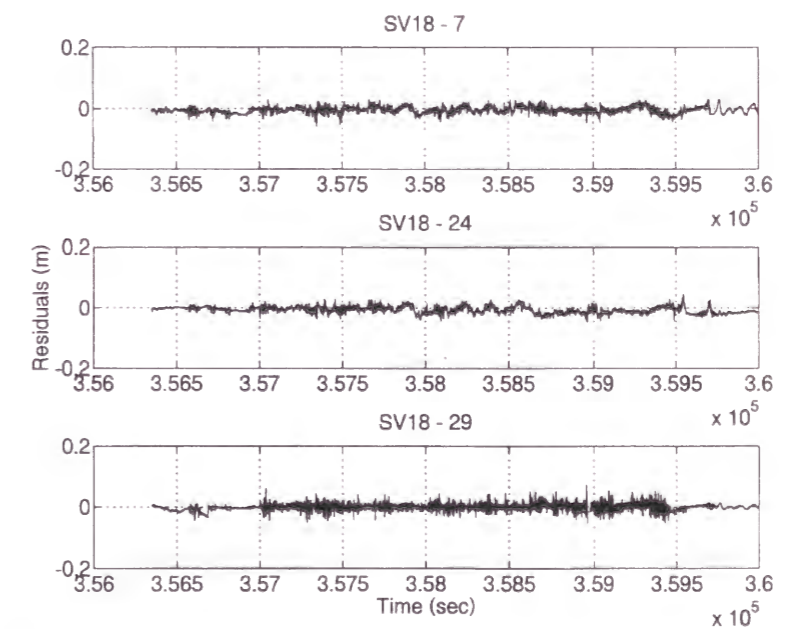


Fig.4-10 Measurement residuals with the tropospheric delay modeling

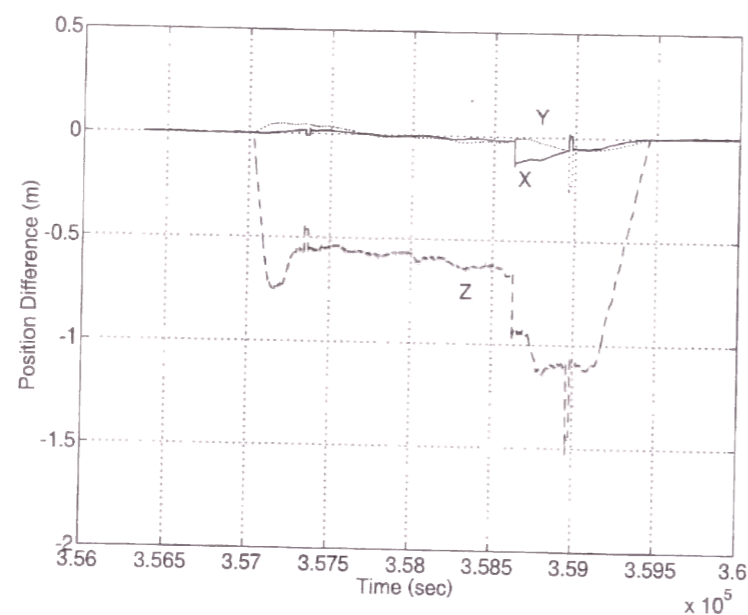


Fig.4-11 Position difference with/without tropospheric delay modeling

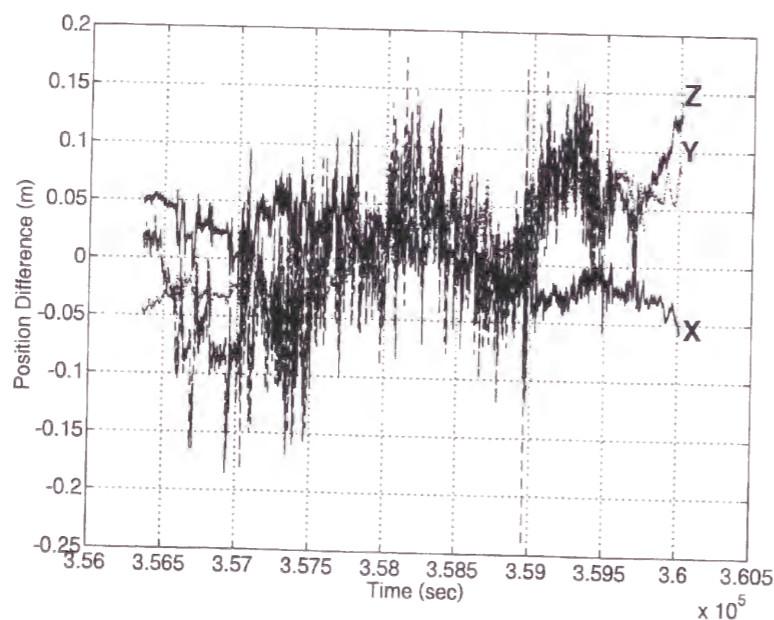


Fig.4-12 Position difference between case 3 and 4

4.1.3 Comparison with Laser Tracked Trajectory

In this section, we compare the KGPS trajectory of an aircraft with the position derived from the laser tracker that is a sensor system independent from GPS. The flight experiment was conducted on 15 Feb. 1995, and the experimental configuration was the same as that described in Chapter 4.1.1. The laser tracker was the Contraves ATARK MK IV (Fig.4-1), which belonged to the Electric Navigation Research Institute (ENRI). The ENRI and NAL conducted a joint research project on the evaluation of Microwave Landing System (MLS) and other navigation systems. The tracker transmits the Yag laser pulse to the reflector which is mounted on the nose of the Do-228 (Fig.4-13), and receives the return pulse. The range between the phase center of the tracker and the reflector is obtained from the propagation time. The position of the reflector is obtained from these range data, the azimuth, and elevation angles data. The accuracy of measuring the range, azimuth, and elevation angles are 0.3m (up to 23km), 0.0056 degrees, and 0.0056 degrees respectively. Therefore the positioning accuracy of the laser tracker degrades according to the distance to the reflector. For example, if the distance from the tracker to the reflector were 10km, the positioning error corresponding to 0.0056 degrees angle error would be about 1m. Fig.4-14 shows the difference between the KGPS solution and the laser tracked position (Harigae, 1997). The position difference between the reflector and the GPS antenna was already calibrated using the INS attitude. The gap seen around the center of Fig.4-14 was due to the lack of tracker data because the tracker couldn't always track the aircraft because of the mechanical limit. It can be seen that the position difference decreased when the aircraft approached the runway. Therefore, we would conclude that the large position difference depending on the distance was derived from the measurement error of the laser tracker's pointing angle. Comparing these two trajectories when the distance was shorter than 3 km, its mean and the standard deviation became as in Table 4-2.

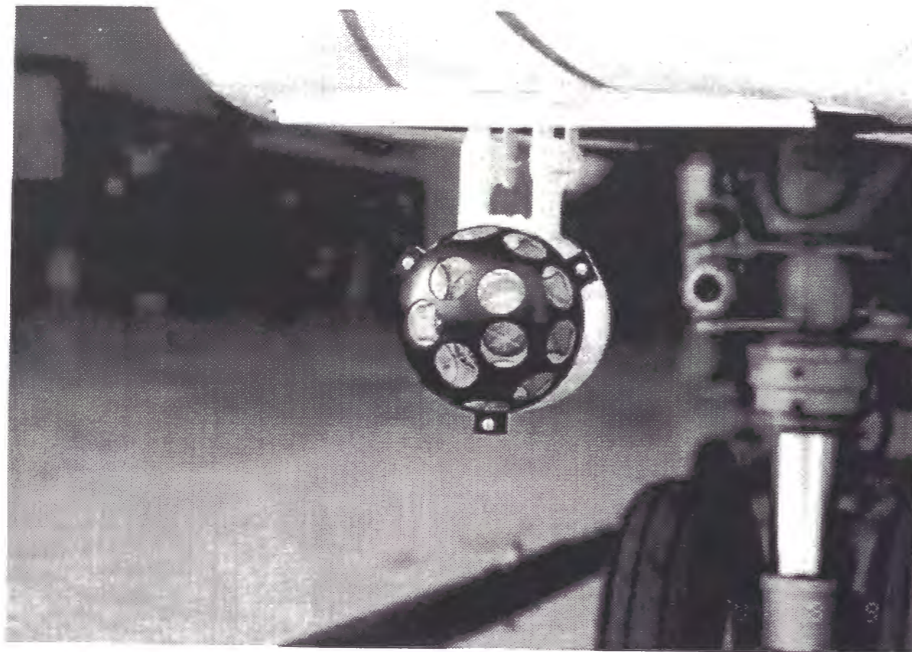


Fig.4-13 Laser reflector mounted under the nose of Do-228

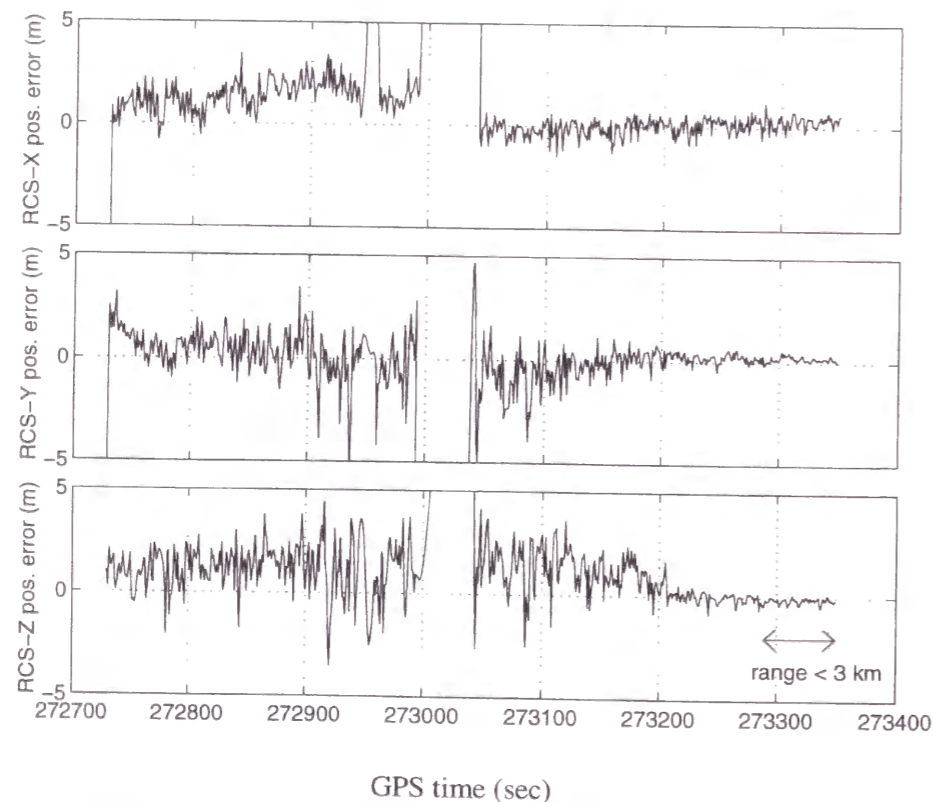


Fig.4-14 Difference between the laser and KGPS trajectory of the Do-228

similar to the range measurement error of the laser tracker. We can conclude herein that the positioning accuracy of KGPS is better than 0.3 m for this short range. However, the accuracy would be at the same level at all distances in the local area if we considered the characteristics discussed in Chapter 3.

Table 4-2 Differences between KGPS and laser trajectory when the distance was shorter than 3 km.

	mean (m)	standard deviation (m)
X	0.32	0.27
Y	0.21	0.12
Z	-0.12	0.14

Also, it can be stated that the KGPS would be a useful tool to calibrate the mounting error of a laser tracker. One orbit around the laser tracker is sufficient to calibrate the local vertical and the reference angle of the azimuth. Actually, we used that method to evaluate the mounting performance by a star calibration system, which was applied to a laser tracker manufactured by the Hitachi Corporation. The laser tracker provided flight profiles of the ALFLEX (Automatic Landing and Flight Experiment) which was an experimental vehicle for a NAL and NASDA (National Space Development Agency of Japan) joint research project to develop an unmanned space vehicle (Matsumoto, et. al., 1996).

4.1.4 Comparison with DGPS/INS Trajectory

A DGPS/INS hybrid navigation system for the automatic approach and landing of aircraft has been developed at NAL (Harigae et. al., 1995). The INS is widely used by airlines during cruise as an autonomous navigation system. However, since the INS has the disadvantage that the position error drifts a few kilometers per hour, it cannot be used for approach and landing (A/L). The instrument landing system (ILS) installed in the airport is used for precise A/L. On the other hand, GPS can give stable position information in any place. If the differential GPS technique were used, its positioning

information in any place. If the differential GPS technique were used, its positioning accuracy would be sufficient for precise A/L. Nevertheless, DGPS also has some disadvantages; for example, the satellite lock would be missed due to banking of the aircraft or a high dynamic maneuver, or the GPS signals would not be available due to the operation by DoD.

The DGPS/INS hybrid navigation system has been investigated to combine the advantages of the two independent systems. In addition to the non-drift precise position, the DGPS/INS provides the velocity, acceleration, attitude, and attitude rate that are essential for the aircraft control in A/L. However, its position accuracy is worse than KGPS since the DGPS/INS uses the pseudorange measurement instead of the carrier phase. Therefore the KGPS solution is used to evaluate the DGPS/INS positioning accuracy (Harigae, 1997). Fig.4-15 shows the position difference between KGPS and DGPS/INS at the approach. The dotted line shows the theoretical value of the DGPS/INS positioning error (3σ). The flight experiment was the same as that described in the previous section. The positioning accuracy was around 1.2m (95%) in all directions which satisfies the requirement of automatic landing. Fig.4-16 shows the velocity difference between KGPS and DGPS/INS, in which the carrier doppler measurements were used for the estimation. If the carrier doppler was not used, the velocity error was two or three times worse than shown in this figure. The dotted line shows the theoretical value of the DGPS/INS velocity error (2σ). Considering that the theoretical accuracy of DGPS/INS velocity is about 0.03 m/s, the large difference seen in Fig.4-16 is thought to be the estimate error of KGPS velocity.

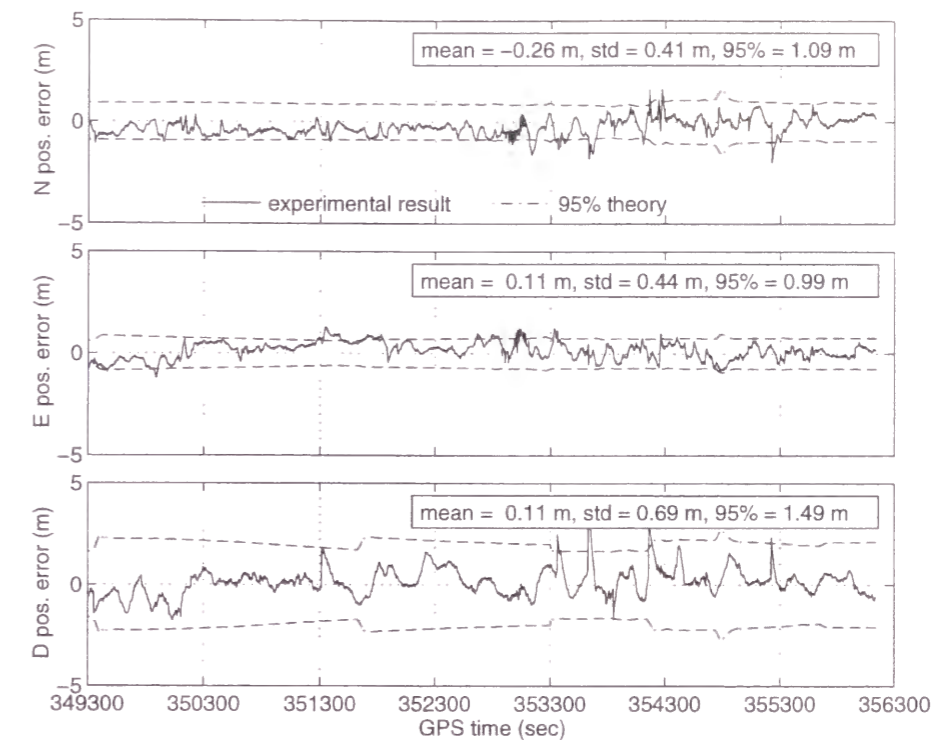


Fig.4-15 Position difference between the DGPS/INS and KGPS

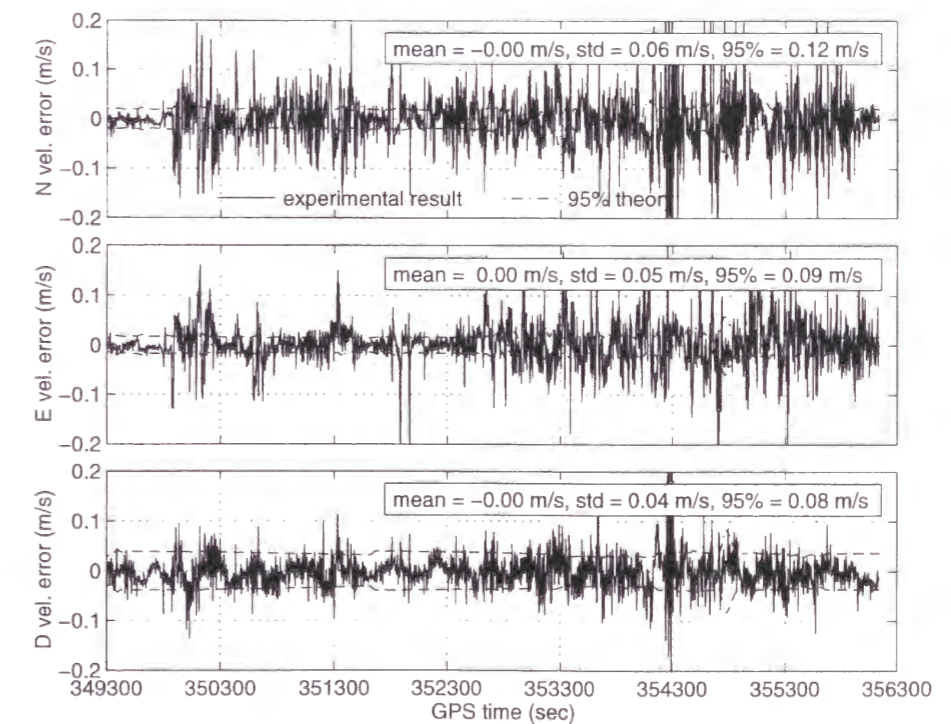


Fig.4-16 Velocity difference between the DGPS/INS and KGPS

4.2 Evaluation of the OTF algorithm

In this section, we evaluate the performance of the OTF algorithm described in Chapter 2 using the real data of a flight experiment conducted on 8th Nov. 1994 at Sendai Airport. The flight test configuration was the same as described in Chapter 4.1.1. The trajectory of the Do-228 is shown in Fig.4-17, and the height profile is shown in Fig.4-18. The one hour of experimental data (GPS DAY¹ 313, GPS Time² 270571 - 274245) included 12 minutes of static data at the parking point (2 and 10 minutes before and after the flight), 41 minutes of flight data, and 8 minutes of taxiing data. The flight area was within about 20km from the reference site, and the height difference is less than 800m. The change of baseline length is shown in Fig.4-19 as well. The number of satellites observed is shown in Fig.4-20, and the RDOP is shown in Fig.4-21. Furthermore, Fig.4-22 gives the elevation of observed satellites. The tropospheric delay was modeled because it is very important for aircraft applications to achieve not only high positioning accuracy but also high performance of OTF (Tsuji et. al. 1994a, 1994b).

At first, we show the performance of the OTF algorithm in Table 4-3 when we applied the test in measurement domain only. The series of OTF trials were performed during the whole of the experiment in a procedure in which the new trial started just after the previous trial finished. The OTF trial here means the so-called initialization in which the ambiguities of all satellites are to be resolved. In this evaluation, the maximum number of observation epochs in one trial, M , was 30 (15 seconds).

It is seen obviously from Table 4-3 that the more satellites observed the more reliable and faster the ambiguity was resolved. To resolve the L1 ambiguity is more difficult than to resolve the widelane ambiguity because the effect of several errors such as the propagation delay, multipath, and noise are relatively large for the L1 carrier phase.

¹The GPS DAY is the cumulative day from the beginning of the year.

²The GPS Time is the cumulative time from the beginning of the week.

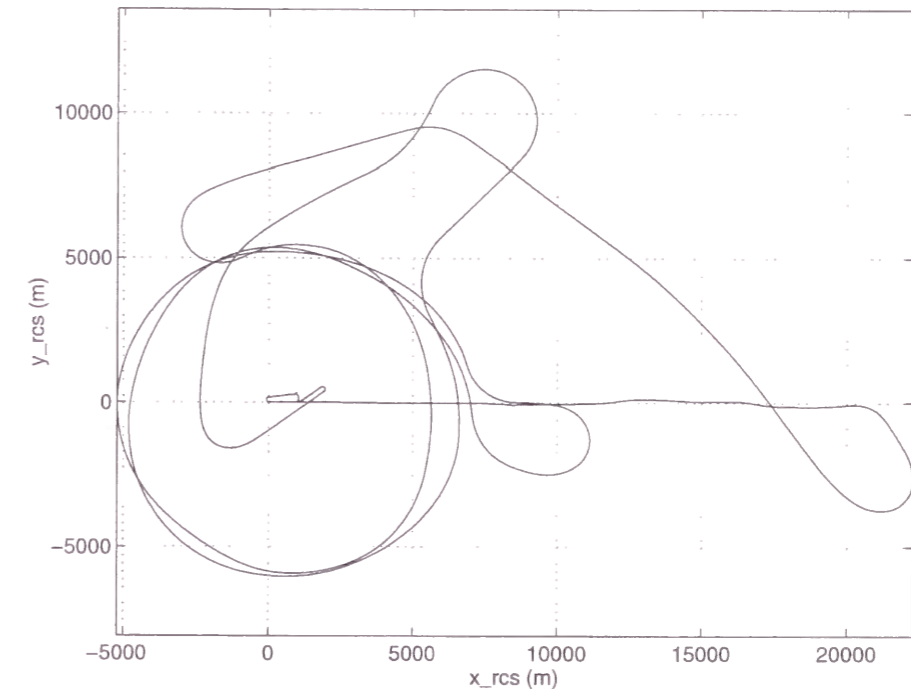


Fig.4-17 Horizontal trajectory of the aircraft

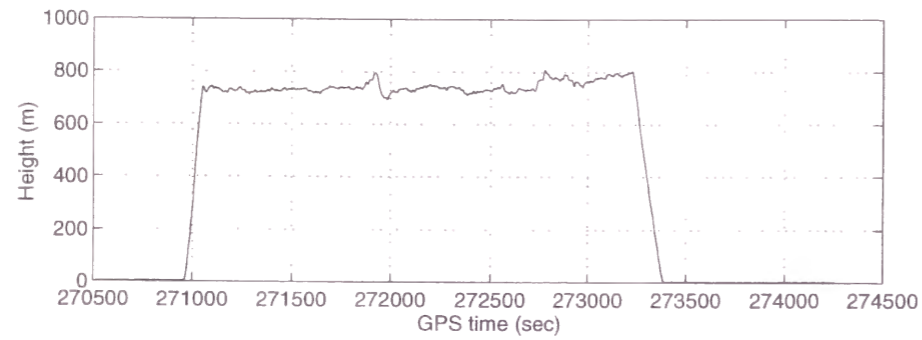


Fig.4-18 Height profile of the aircraft

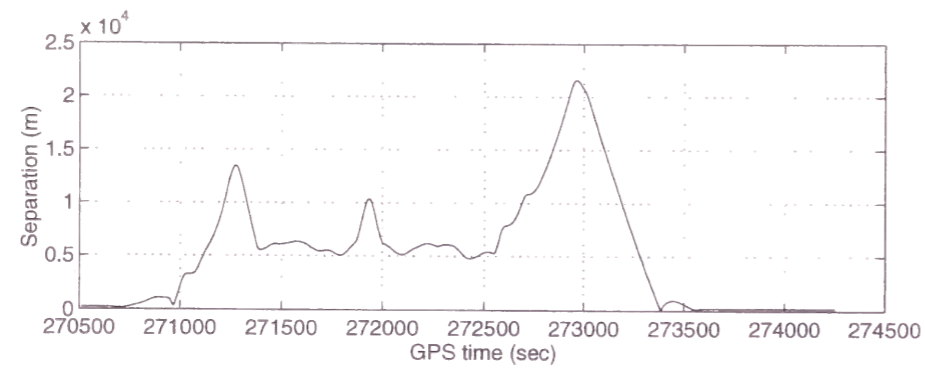


Fig.4-19 Separation between the reference receiver and the aircraft

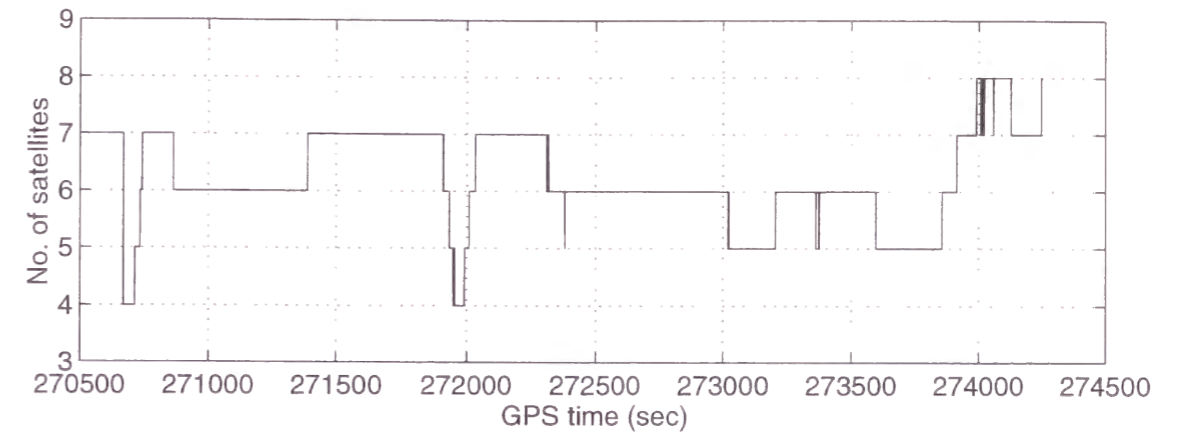


Fig.4-20 Number of satellites observed during the flight test

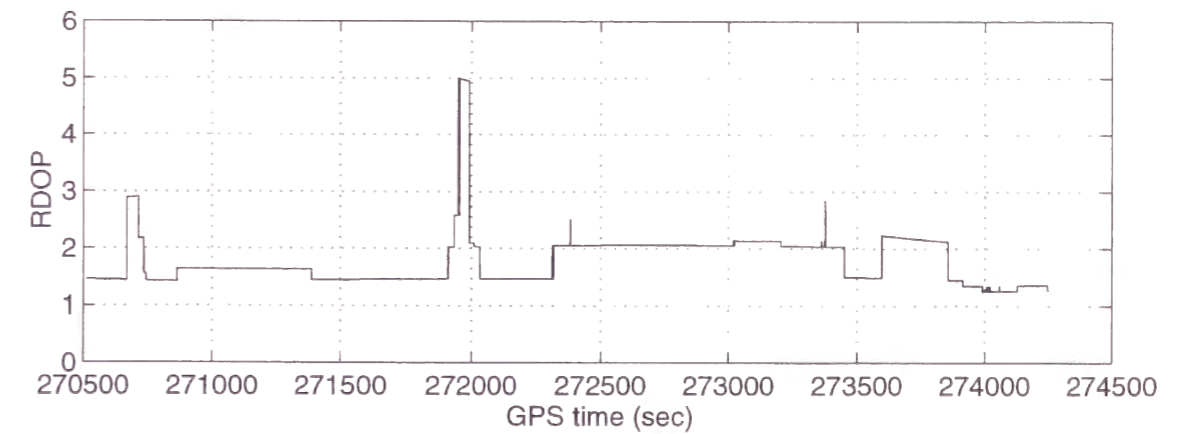


Fig.4-21 Variation of RDOP during the flight test

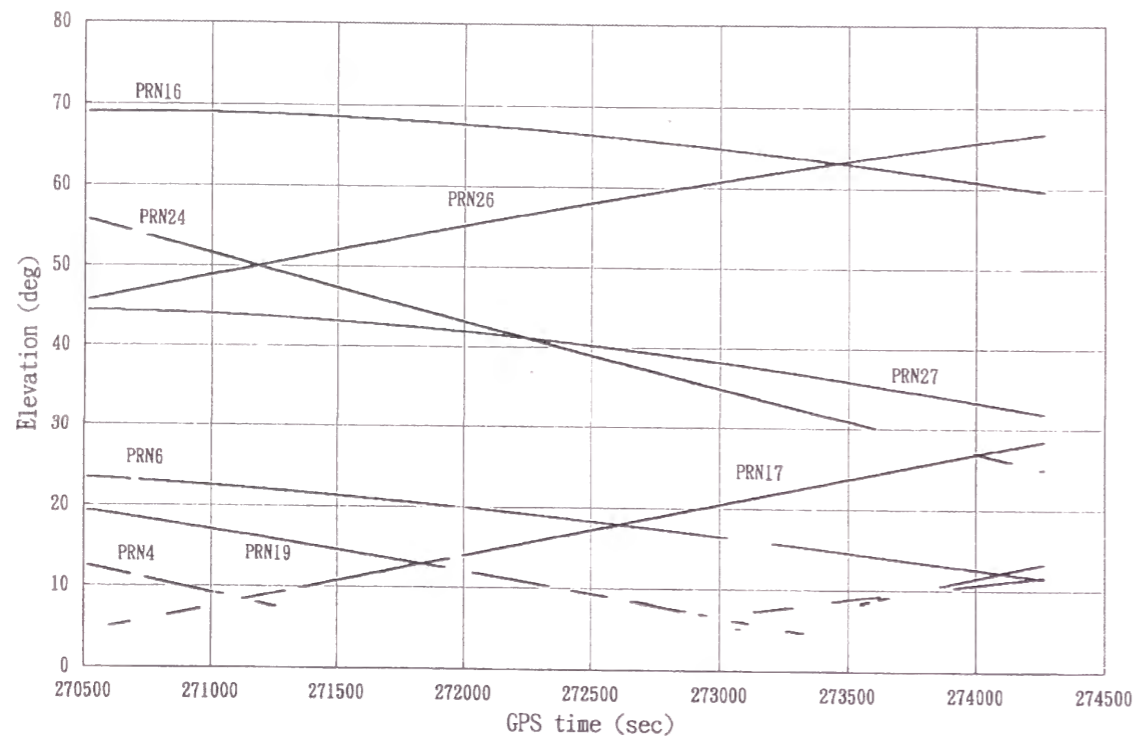


Fig.4-22 Elevations of observed satellites

Table 4-3a Summary of widelane OTF using the test in measurement domain only

No. of satellites	a) No. of total used epochs	b) No. of OTF trials	c) No. of solutions	d) No. of correct solutions	probability of obtaining correct solution (d/c)	average epochs required for resolution(a/d)
5	6379	4241	3846	3769	98.0	1.7
6	5117	5044	4432	4432	100.0	1.2
7	2008	1954	1303	1300	99.8	1.5

Table 4-3b Summary of L1 OTF using the test in measurement domain only

No. of satellites	a) No. of total used epochs	b) No. of OTF trials	c) No. of solutions	d) No. of correct solutions	probability of obtaining correct solution (d/c)	average epochs required for resolution (a/d)
5	6788	794	197	54	27.4	125.7
6	6195	1111	781	691	88.5	9.0
7	2743	993	954	947	99.3	2.9

Table 4-4a Summary of widelane OTF using the tests in both measurement and positioning domains

No. of satellites	a) No. of total used epochs	b) No. of OTF trials	c) No. of solutions	d) No. of correct solutions	probability of obtaining correct solution (d/c)	average epochs required for resolution (a/d)
5	6379	4241	3846	3769	98.0	1.7
6	5117	5044	4432	4432	100.0	1.2
7	1991	1991	1645	1645	100.0	1.2

Table 4-4b Summary of L1 OTF using the tests in both measurement and positioning domains

No. of satellites	a) No. of total used epochs	b) No. of OTF trials	c) No. of solutions	d) No. of correct solutions	probability of obtaining correct solution (d/c)	average epochs required for resolution (a/d)
5	6557	6522	5597	5592	99.9	1.2
6	6170	6170	5476	5475	99.98	1.1
7	2736	2736	2616	2616	100.0	1.05

Note that the wavelength of the L1 carrier phase is about 19cm and is much shorter than that of the widelane. When only five satellites were observed, the possibility of obtaining the correct ambiguity was degraded considerably because the degree of freedom was small ($=1$). Hereafter, we will show an example of the L1 ambiguity search when five satellites were observed. The ambiguity search was performed ± 1 cycle from the initial estimate of the ambiguity so that the number of candidates was 27. Fig.4-23 shows the RSS (Root-Sum-Squares) values of measurement residuals divided by the degree of freedom (the left side of Inequality (2.2-12)) for all candidates at GPS time 272100. The horizontal axis shows the candidate number. The five satellites (PRN 6, 16, 24, 26, 27) with the smallest RDOP were chosen though seven satellites were actually observed at the time. Since the degree of freedom is one, the value of $\chi_{df,1-\alpha}^2/df$ in Inequality (2.2-12) becomes 6.63 with the significant level of 99%. The solid line in Fig.4-23 indicates the threshold of this test. Accordingly, seven candidates were left at the time. The same test would be performed on the remaining candidates with successive measurements, and the one that was not rejected until the end would be the solution. Although the correct ambiguity set is candidate No. 14, the RSS value is minimum for candidate No. 25.

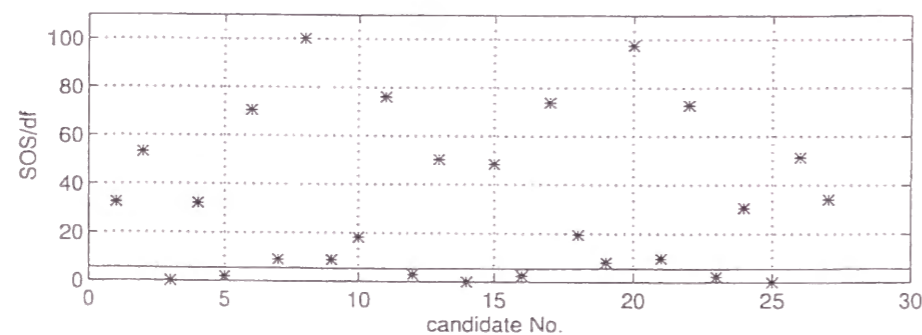


Fig.4-23 (Sum of squared residuals / degree of freedom) of each L1 phase ambiguity candidate. Solid line represents the threshold of 99 %.

Fig.4-24 shows the residuals of double differenced L1 carrier phases for the correct ambiguity set (No.14). The satellite combinations are (PRN16-6), (PRN16-24), (PRN16-26), and (PRN16-27) respectively from top to bottom. On the other hand, Fig.4-25 gives the residuals for candidate No.25 in which the ambiguities of (PRN16-24), (PRN16-26), and (PRN16-27) have one-cycle errors. Though the residuals of the wrong ambiguity set, No.25, increase gradually according to the change of satellite constellation with time, the difference between Fig.4-24 and 4-25 could not be seen clearly until more than 5 minutes passed. In fact, the RSS of the wrong candidate was smaller than that of the correct candidate for 330 seconds. Therefore, the wrong candidate would possibly be selected as a solution in this case. In addition to the test described above, the so called 'ratio test' is often applied, in which the minimum RSS and the second minimum RSS are compared and if the ratio is larger than 2 or 3, the candidate that has minimum RSS should be selected as a solution. However in this example, the ratio was larger than 2 for 288 seconds from the beginning. This means that the ratio test should be performed a few minutes after the beginning of the OTF trial. Considering the reasons mentioned above, it is recommended normally to perform the OTF when 6 or more satellites are observed (Lachapelle 1992a).

Next, we show the result of OTF if the test in positioning domain was performed in addition to the test in measurement domain. The result of widelane OTF is summarized in Table 4-4a, which shows little difference from Table 4-3a. This is because the difference between the pseudorange-position and the position calculated using the widelane ambiguity candidate would be considerably close to the value of σ_H^{PR-W} as seen in Eq. (2.2-17) and (2.2-18).

On the other hand, the performance of L1 OTF shown in Table 4-4b was dramatically improved. The correct ambiguity was resolved almost instantaneously with better than 99% possibility even when five satellites were observed. In the L1 OTF, if the ambiguity of a candidate had a one-cycle error, the position difference would be much greater than σ_H^{W-L1} as seen in Eq. (2.2-21) and (2.2-22). Therefore, the wrong candidates would be easily rejected. Fig.4-26 shows the distribution of the positions calculated using the smoothed pseudorange, the widelane and L1 ambiguity candidates

at the time 272100, in which \times , \ast , \circ stand for pseudorange, widelane, and L1 carrier phase. The position of origin was calculated using correct L1 ambiguity. In this case, the position corresponding to the correct widelane ambiguity was closest to the origin among all the widelane positions. If the difference between the position for correct widelane ambiguity and the position for a L1 candidate (\circ) was larger than the threshold value, the candidate would be rejected according to the test in positioning domain.

Fig.4-27 gives the horizontal, vertical and three dimensional differences between the position calculated using the correct widelane ambiguity and that using each L1 candidate, in which the solid line indicates the threshold of the test in positioning domain with a significant level of 99%. As a result, 10, 22, and 18 candidates would pass the tests in horizontal, vertical and three-dimensional positioning domain. Among these candidates, those that also passed the test in measurement domain would be retained as the candidates at the next measurement epoch. Comparing Fig.4-23 with Fig.4-27, if we considered the vertical or three dimensional position, all of the seven candidates which passed the test in positioning domain also would pass the test in measurement domain. On the other hand, only one candidate would be retained if the horizontal position were evaluated. That is to say, the correct ambiguity of the L1 carrier phase was resolved instantaneously. Thus, it becomes clear that the ambiguity can be resolved fast by evaluating the horizontal position in the positioning domain test.

In the proposed OTF algorithm, the better the accuracy of pseudorange-position is, the faster and more reliable the widelane ambiguity is resolved. Therefore, it is desirable to reduce the multipath error in pseudorange as much as possible. Recently, some GPS receivers, antennas, and software that mitigate the multipath have been developed (Newby, 1995; Kee, 1995). For example, the NovAtel Co. developed the narrow correlator receiver and Multipath Elimination Technology (MET) whose ranging error of pseudorange would be some tens of centimeters. Since the test in positioning domain is available even if four satellites are observed, the proposed algorithm would have a more stable performance by using such a high performance GPS receiver.

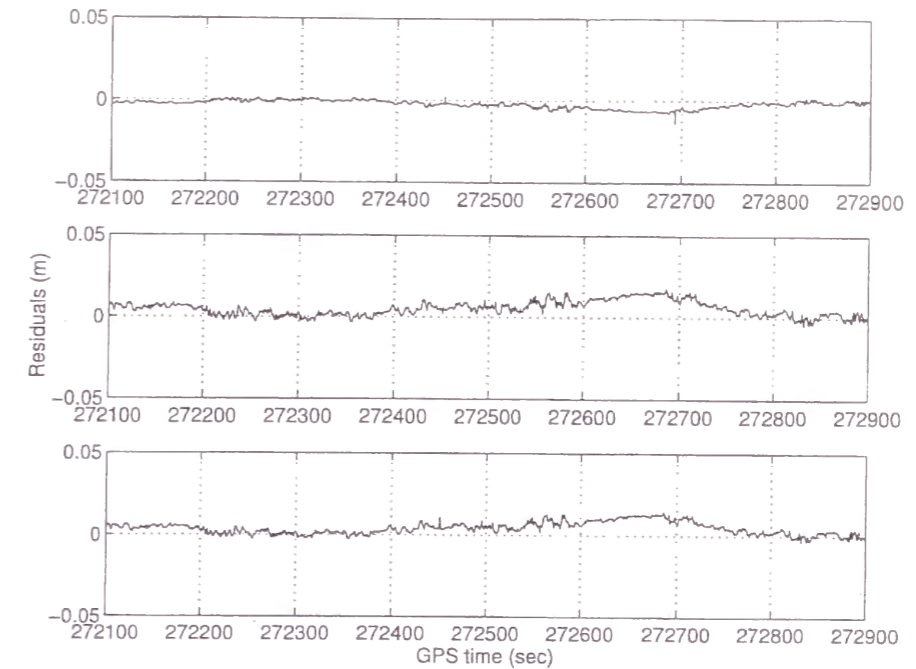


Fig.4-24 Residuals of double differenced L1 phase measurement with correct ambiguities (PRN16-6, 16-24, 16-26, 16-27)

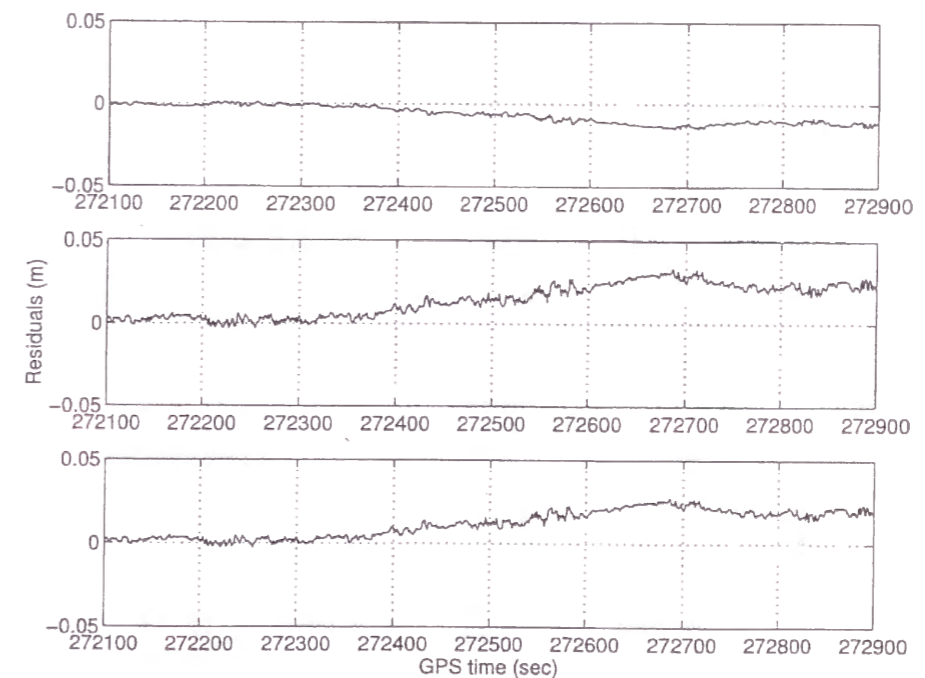


Fig.4-25 Residuals of double differenced L1 phase measurement with incorrect ambiguities (PRN16-6, 16-24, 16-26, 16-27)

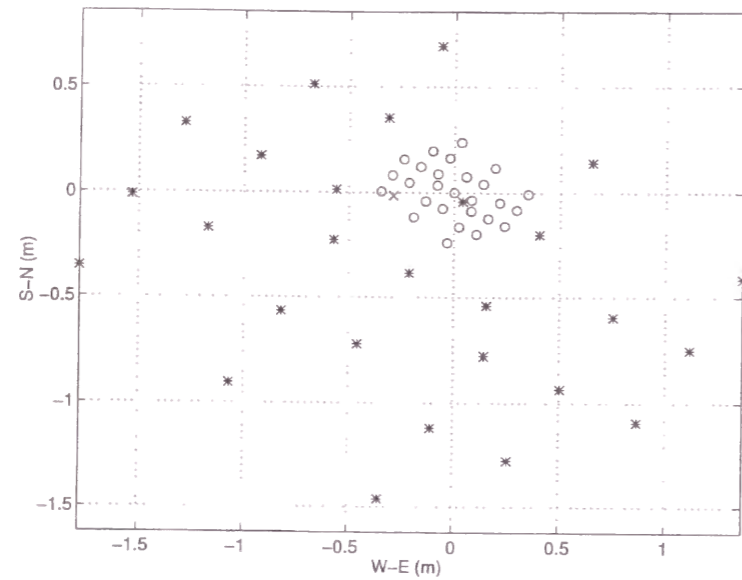


Fig.4-26 Horizontal position of the receiver using smoothed pseudorange (×), widelane ambiguity candidates (*), and L1 phase ambiguity candidates (O)

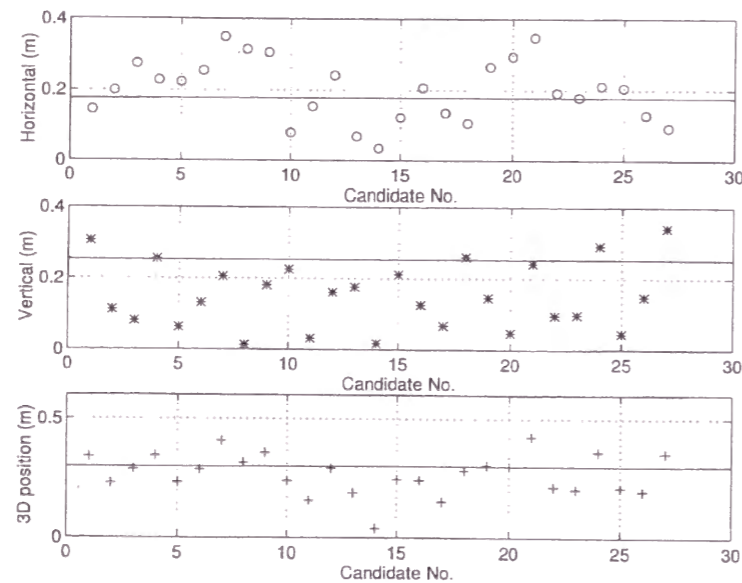


Fig.4-27 Difference between the position calculated using the correct widelane ambiguity and those using each candidate of L1 phase ambiguity

4.3 Attitude Determination

We will show the results of the attitude determination of an aircraft including the estimation of the structural flexures. Though the hardware of our attitude determination system is composed of several manufactures on the market such as GPS receivers, antennas, and PC, the algorithms has been developed by ourselves in which the KGPS algorithms is the fundamental technique (Tsujii et. al., 1996a, 1997a).

4.3.1 Flight Test Configuration

A flight test was conducted by NAL on 23 Oct. 1996 around Chofu airfield in Tokyo. Four L1 GPS antennas were mounted on the Do-228. The two on the aircraft fuselage were connected to Trimble 4000SSE receivers, while the two on the wing tips were connected to NovAtel GPSCards with each receiver controlled by a notebook computer (Toshiba Dynabook V486). The forward and aft antennas (Trimble 16248-20) are shown in Fig.4-28 and the left wing antenna (NovAtel 511) is shown in Fig.4-29. GPS L1 carrier phase measurements at 2Hz were recorded and analyzed after the flight.

A strapdown ring laser gyro INS (Litton LTN-92) was also aboard to provide an independent attitude at 64 Hz. The accuracy is 0.05 degrees in pitch and roll, and 0.4 degrees in the yaw axis. In order to synchronize the INS attitude measurements with GPS time, a one pulse per second timing signal from an Ashtech Z-12 GPS receiver was used. The Ashtech Z-12 connected to the dual frequency antenna is a regular piece of equipment of the Do-228 that gives the aircraft position. Data from the INS and the Ashtech Z-12 were recorded by a Flight Data Acquisition System (FDAS) which has been developed by NAL in order to record data from many kinds of sensors such as a laser altimeter, DME (Distance Measurement Equipment), MLS, and so on. The block diagram of the experimental system is shown in Fig.4-30.

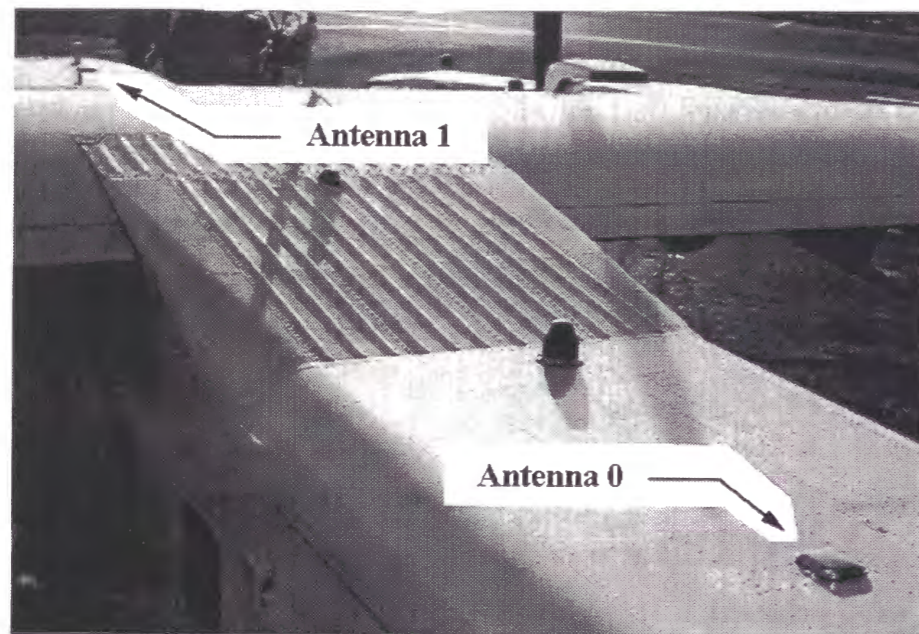


Fig.4-28 GPS L1 antennas (Trimble 16248-20) mounted on the fuselage

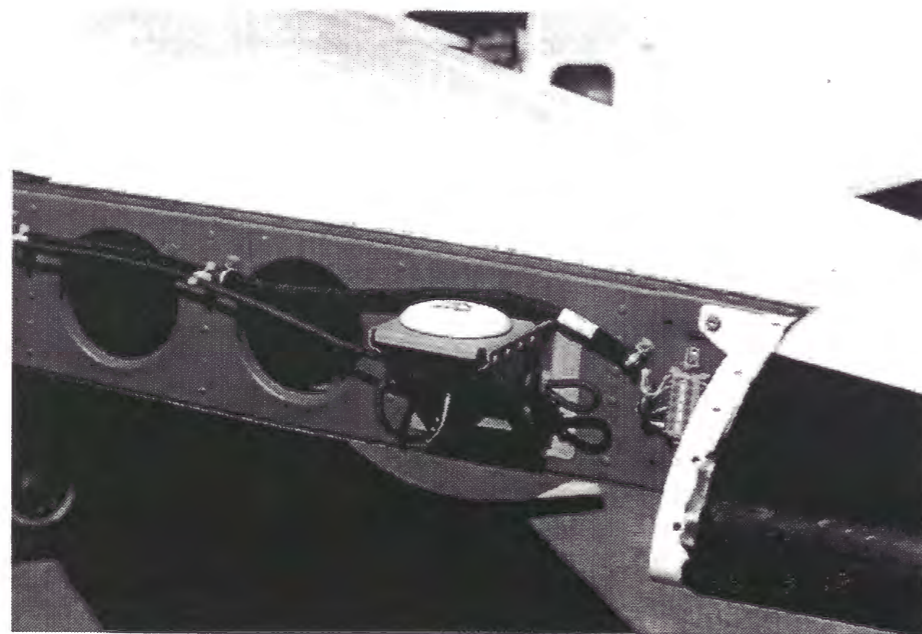


Fig.4-29 Left wing antenna (NovAtel 511). The wing tips were covered during the operations

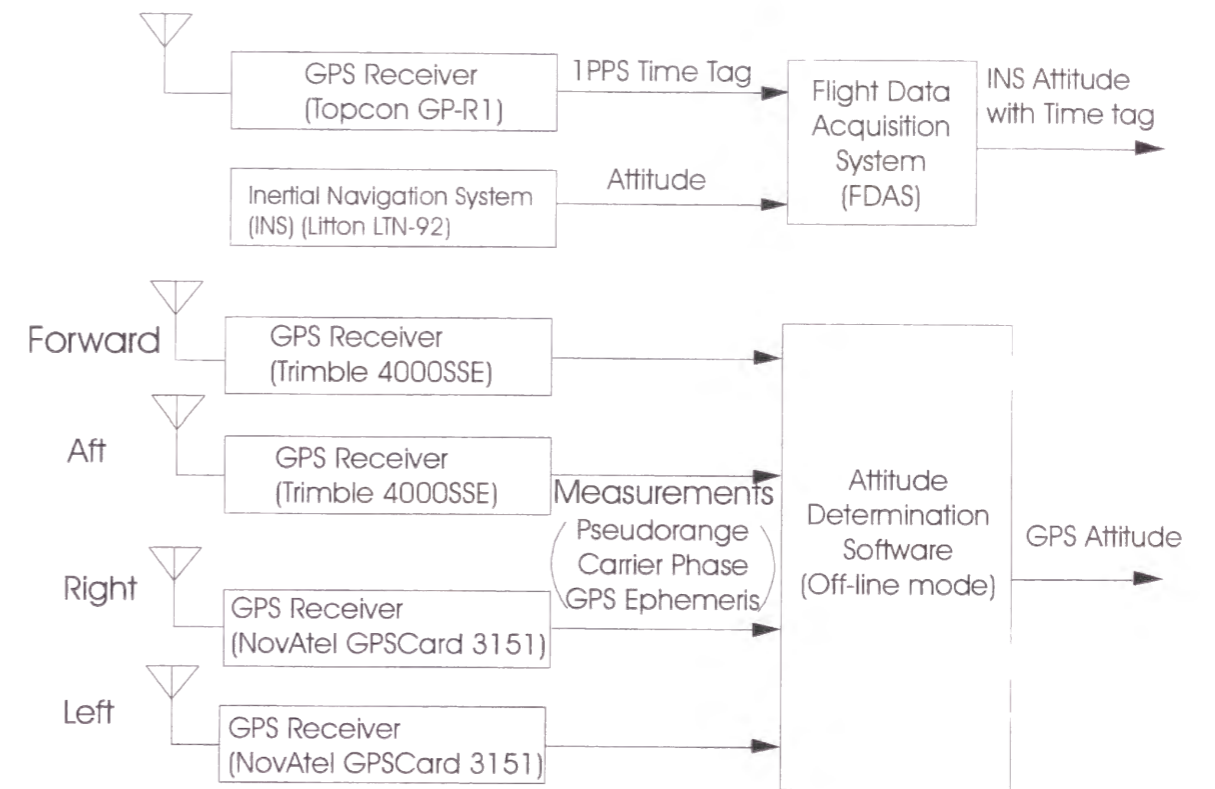


Fig.4-30 Block diagram of the experimental system

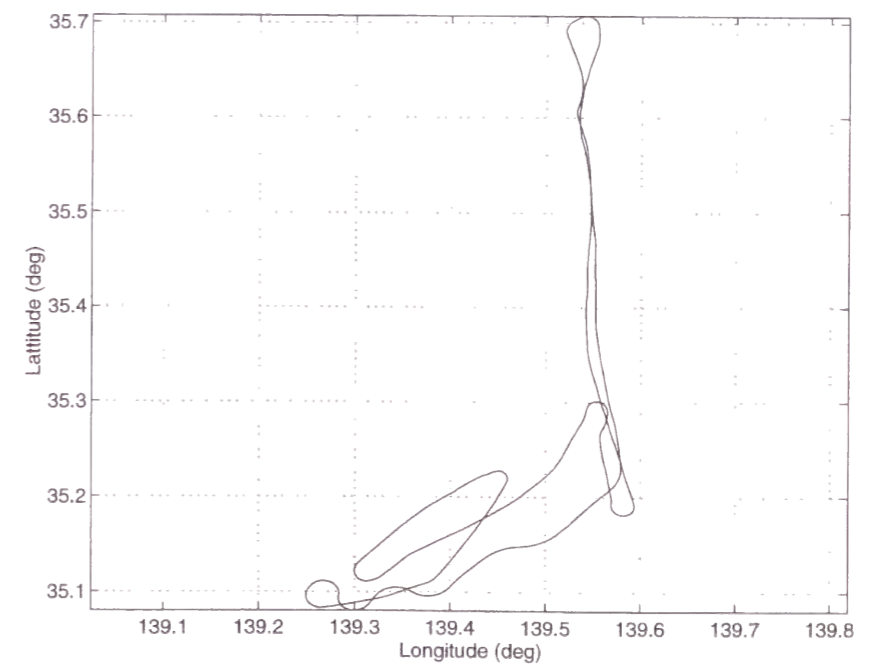


Fig.4-31 Flight trajectory during the experiment of attitude determination

The aircraft trajectory of approximately 50 minutes from GPS time 280000 to 283000 is shown in Fig.4-31. The aircraft took off a few minutes before the time 280000 and landed at around the time 283000. The GPS time 280000 is set to time zero hereafter for all figures. The roll angle ranged from -40 to +35 degrees and the pitch ranged from -5 to 16 degrees. During the flight, more than 6 satellites were normally observed, and the satellites with an elevation higher than 10 degrees were used for the processing.

4.3.2 GPS-Estimated Attitude

The least squares search method was adopted to resolve the ambiguity of the L1 carrier phase. In a kinematic positioning of a vehicle relative to a reference station, it is generally very difficult to resolve carrier phase ambiguities if L1 single frequency receivers are used. It requires some tens of minutes to resolve ambiguities since the GPS satellites positions relative to the baseline have to change significantly. On the other hand, directions of baseline vectors in the attitude determination system change dramatically relative to the satellites due to changes of attitude. In other words, the observability of the GPS carrier phase is very large for the attitude. Besides that, the known antenna separations are available as a constraint to reduce the number of ambiguity candidates. Thus, L1 ambiguities were resolved quite easily in a few seconds. Though El-Mowafy and Schwarz (1995) proposed an instantaneous ambiguity resolution method by installing more antennas collinear to the existing antenna vectors, this would not have much advantage because the OTF for attitude determination is not so difficult itself.

Fig.4-32 shows residuals of three antenna baseline lengths during the flight. Since the Root-mean-squares (RMS) of residuals are 0.5, 0.6, and 0.5 cm respectively, the relative positions of the slave antennas were estimated precisely during the flight. However, the residuals became a little larger in some periods (near the time 1000, 1500 and 2200) where the roll angle is large and cycle slips occur to the lowest satellite (see Fig.4-33).

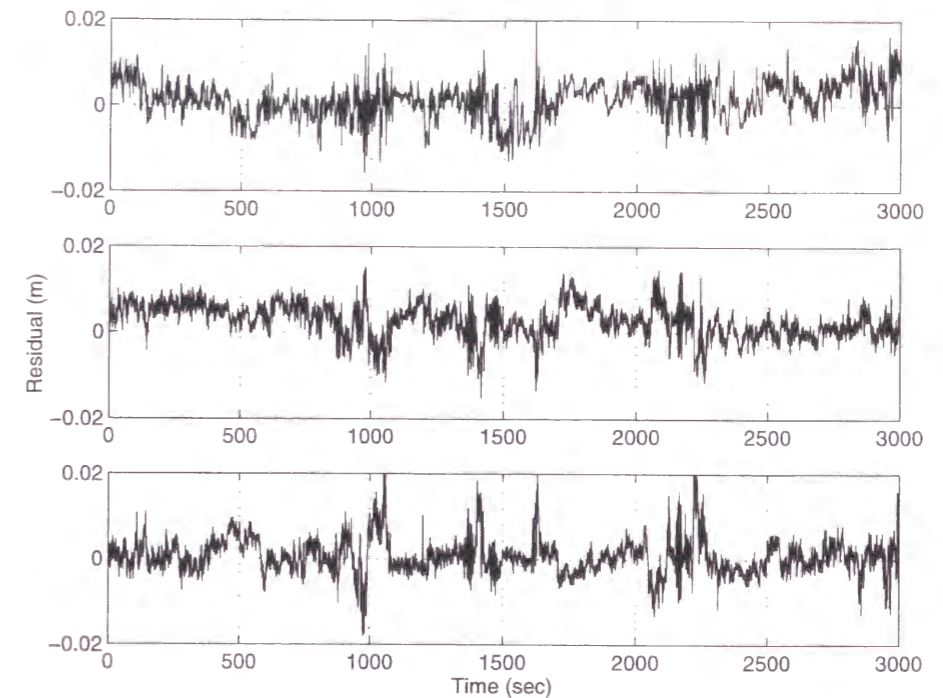


Fig.4-32 Residuals of three antenna baseline lengths during the flight

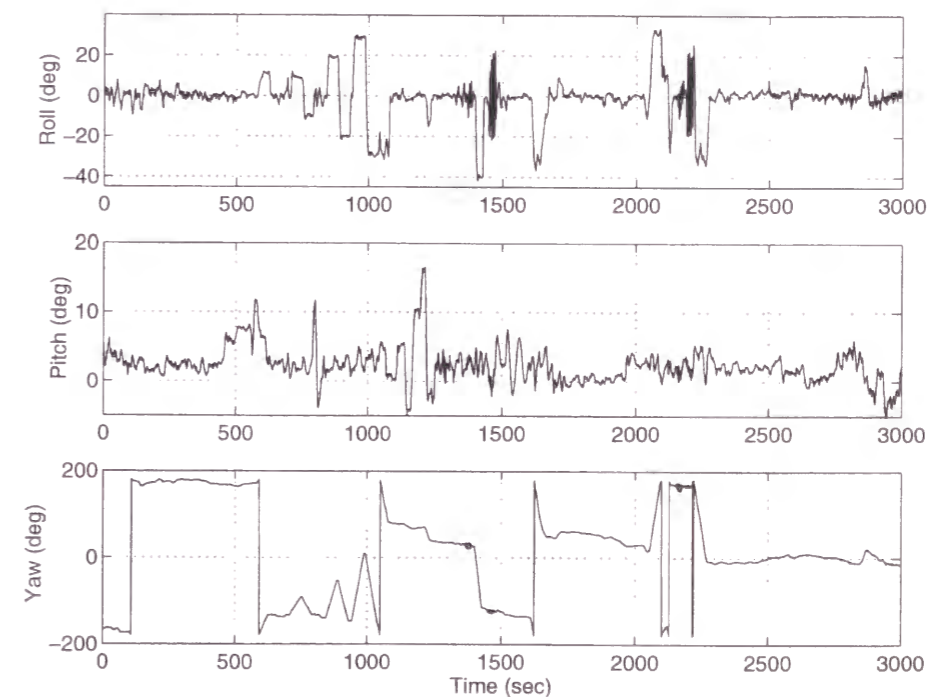


Fig.4-33 GPS-estimated attitude of the air

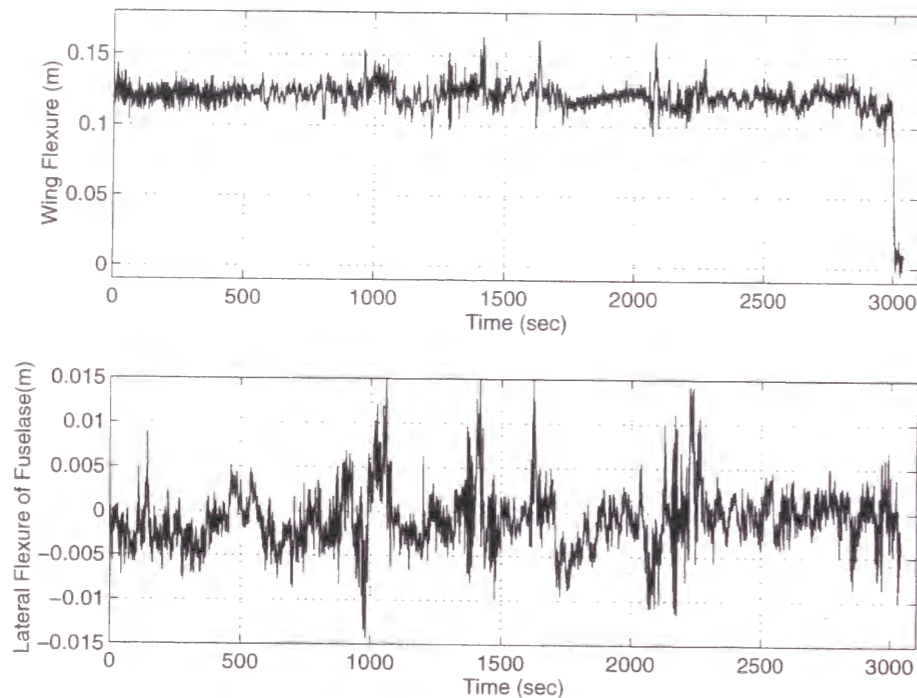


Fig.4-34 GPS-estimated flexures of wing and fuselage

GPS-estimated attitude and structural flexure is shown in Fig.4-33 and 4-34. The attitude receiver system never lost the lock of integer ambiguity throughout the flight; therefore, it was not necessary to perform the OTF after the first fixing of ambiguity. The wing flexure was nominally 12 cm in flight, and became near zero after landing (time 3000). The estimated lateral flexure of fuselage reached up to ± 1.5 cm due to the rapid maneuver of the aircraft.

4.3.3 Comparison with INS Attitude

GPS attitude was compared with the reference attitude that was provided by the INS, after the misalignment between the INS and the body frame was calibrated (Eq.2.5-13). Unfortunately, the INS measurements were recorded for only 700 seconds from time 2300 to 3000 because of a problem with the FDAS. Values of GPS minus INS attitude angles are presented in Fig.4-35, and the GPS estimated attitude and flexure are shown in Fig.4-36. The RMS of roll, pitch, and yaw differences were 0.052, 0.060, and 0.075 degrees, respectively.

The accuracy of attitude angle is approximately expressed by the value of the positioning accuracy divided by the baseline length. For example, when we adopt 0.5 cm as a nominal positioning accuracy and 6.41 m as a baseline length, the accuracy of angle will be 0.04 degrees. This value is slightly smaller than the computed RMS shown beforehand. However, considering that the calibrated INS attitude is described by the rotation angles from the local level to the nominal body frame and ignores the instantaneous structural flexure, this discrepancy can be thought to be acceptable. Though there is a fairly large discrepancy in yaw angle (time 2850 - 2870), this is thought to be caused by an instantaneous flexure of the fuselage due to a yaw maneuver. In this period, there is a correlation between the yaw difference in Fig.4-35 and the lateral flexure of the fuselage in Fig.4-36.

Table 4-5 summarizes the difference between GPS and INS attitude in three cases;

Case 1: Attitude and wing and lateral fuselage flexure were estimated,

Case 2: Attitude and wing flexure were estimated,

Case 3: Attitude was estimated.

It is apparent that modeling wing flexure is very important to achieve high attitude accuracy.

Table 4-5 Summary of attitude difference between GPS and INS

	CASE 1			CASE 2			CASE 3		
	mean	rms	s.t.d.	Mean	rms	s.t.d.	mean	rms	s.t.d.
ROLL	0	0.052	0.052	0	0.052	0.052	0.020	0.056	0.052
PITCH	-0.002	0.060	0.060	-0.002	0.060	0.060	0.721	0.725	0.073
YAW	0	0.075	0.075	0	0.073	0.073	0.010	0.098	0.098

(Unit: degrees)

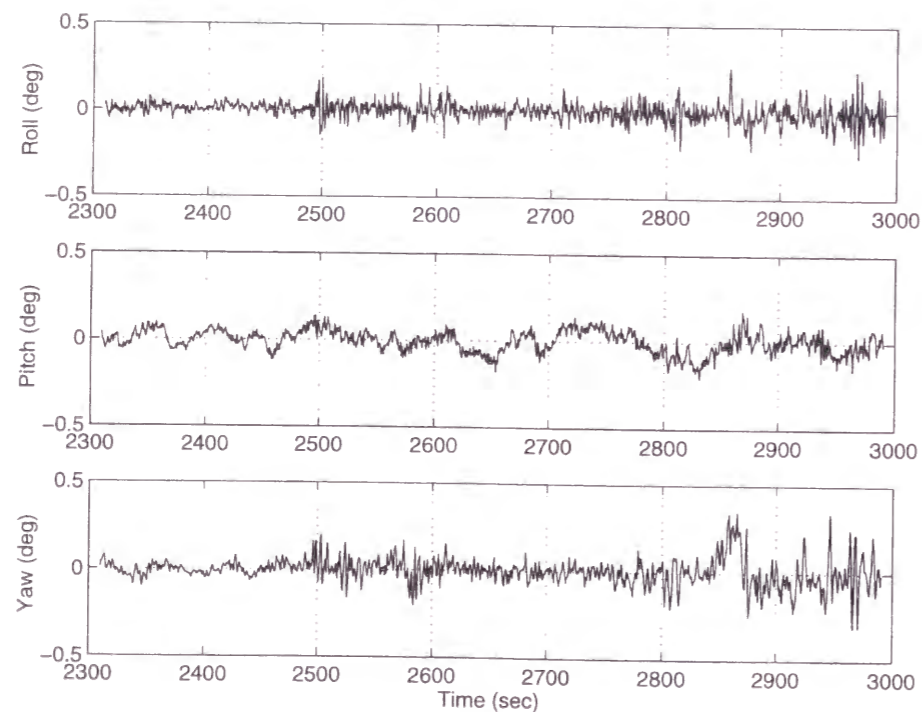


Fig.4-35 Difference between GPS and INS attitude angles

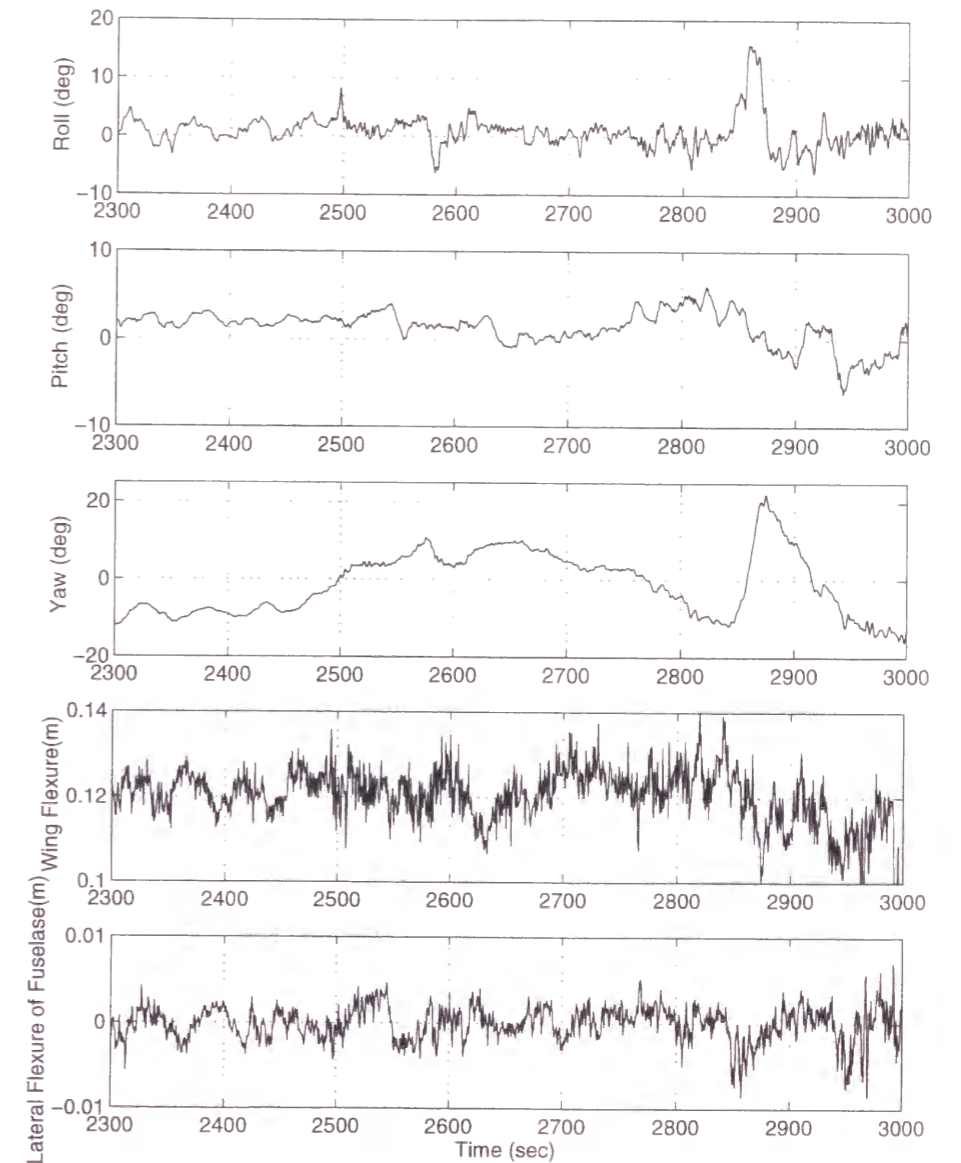


Fig.4-36 GPS estimated attitude and flexure

4.3.4 Structural Flexure

In order to demonstrate the effect of modeling the lateral flexure of the fuselage, we conducted yaw reversals, although INS reference attitude data could not be recorded. Fig.4-37 shows a change of yaw angle and the corresponding lateral flexure of fuselage during the yaw reversals. It is clear that the flexure strongly correlates with the change of yaw angle in the period of yaw maneuver. We also plot in Fig.4-38 the Root-Sum-Squares (RSS) of residuals in the estimation process for Cases 1 and 2. When the fuselage flexure is not modeled (Case 2, lower graph), the RSS is large and a trend appears during the strong maneuver. On the other hand, the trend could not be seen clearly when the flexure was modeled. We conclude that a large part of lateral fuselage flexure was correctly estimated by this simple modeling.

Finally, we show the estimated wing flexure during pitch and roll maneuvers. Fig.4-39 shows pitch, pitch rate, and the corresponding wing flexure when the aircraft pitch is held at 0, 5, -5, 10, 15 degrees. The change of wing flexure and pitch rate shows quite similar tendencies. The same result was obtained during pitch reversals, which are shown in Fig.40. Fig.4-41 shows the relation between the aircraft roll, roll rate, and the wing flexure during roll reversals. The frequency of wing flexure may be two times as large as that of roll angle, although this is not clear due to the low observation rate of GPS.

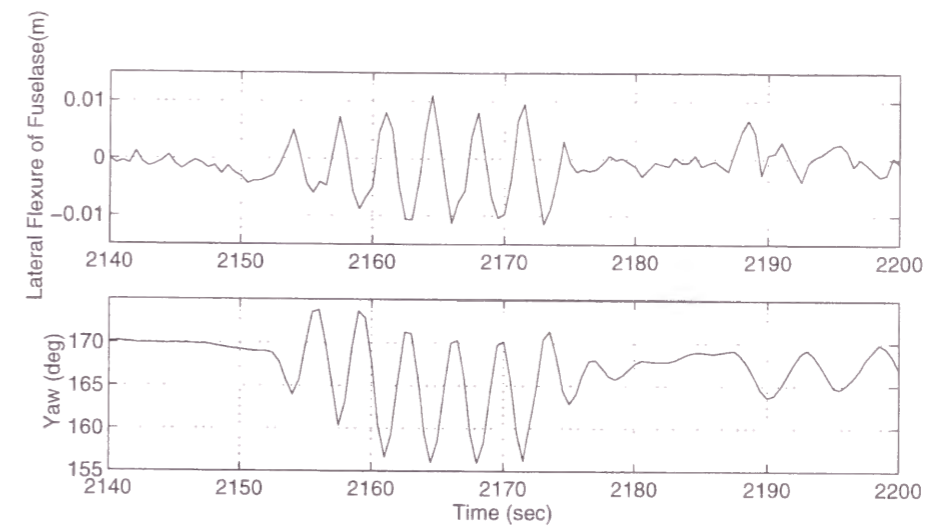


Fig.4-37 Change of yaw angle and the corresponding lateral flexure of fuselage during the yaw reversals

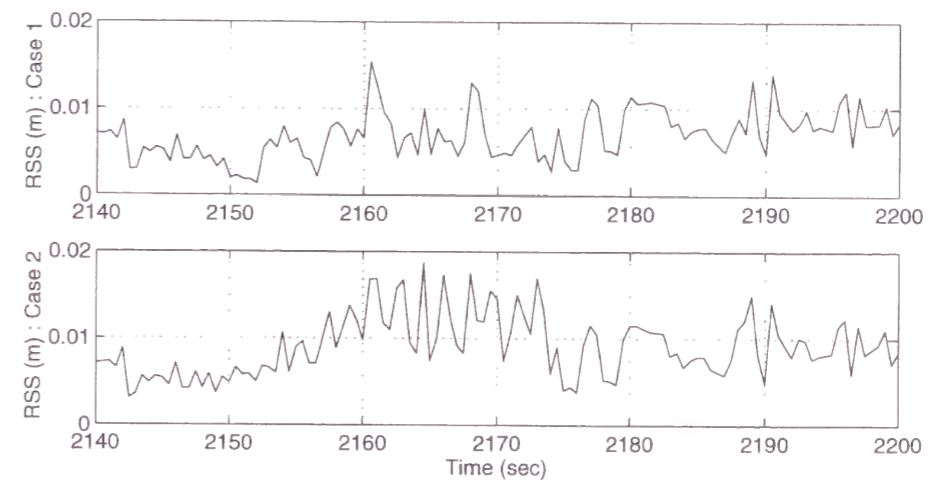


Fig.4-38 Root-Sum-Squares (RSS) of residuals in the estimation process for Case 1 (upper) and Case 2 (lower)

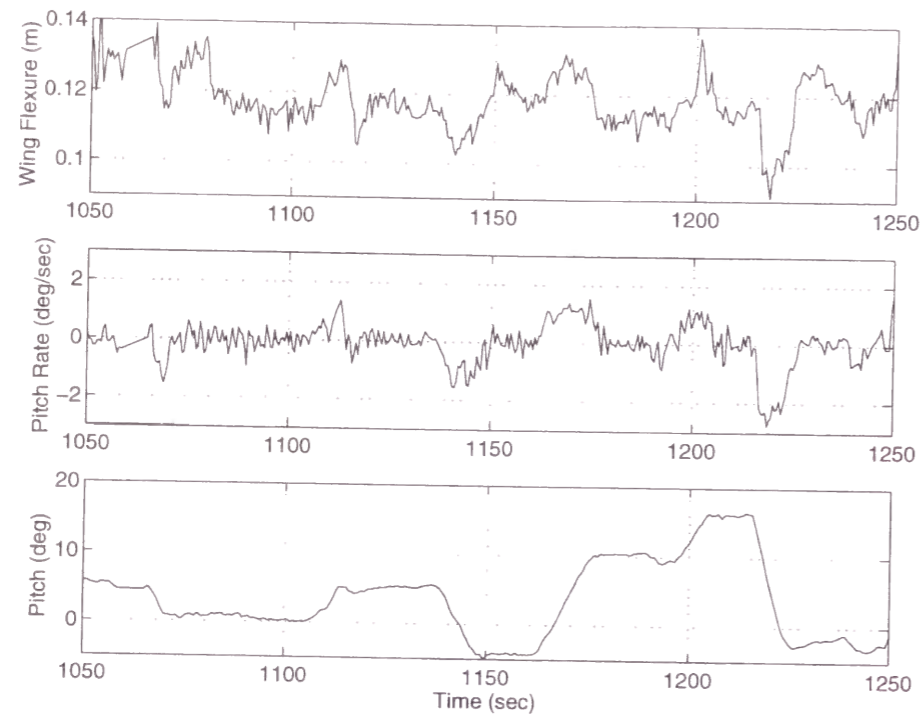


Fig.4-39 Pitch, pitch rate, and the corresponding wing flexure when the aircraft pitch is held at 0, 5, -5, 10, 15 degrees

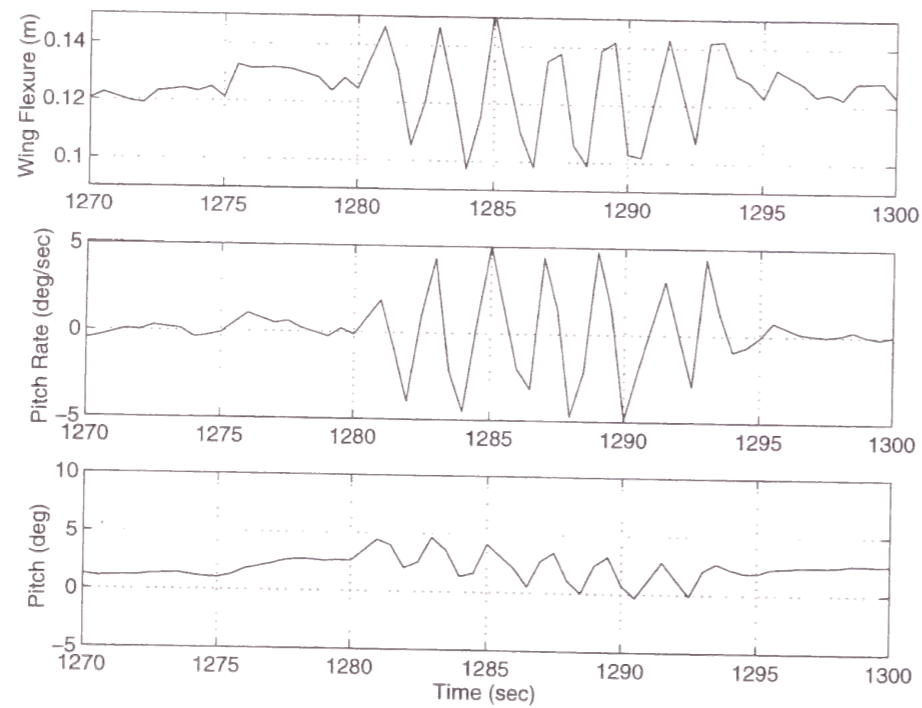


Fig.4-40 Change of wing flexure, pitch, and pitch rate during pitch reversals

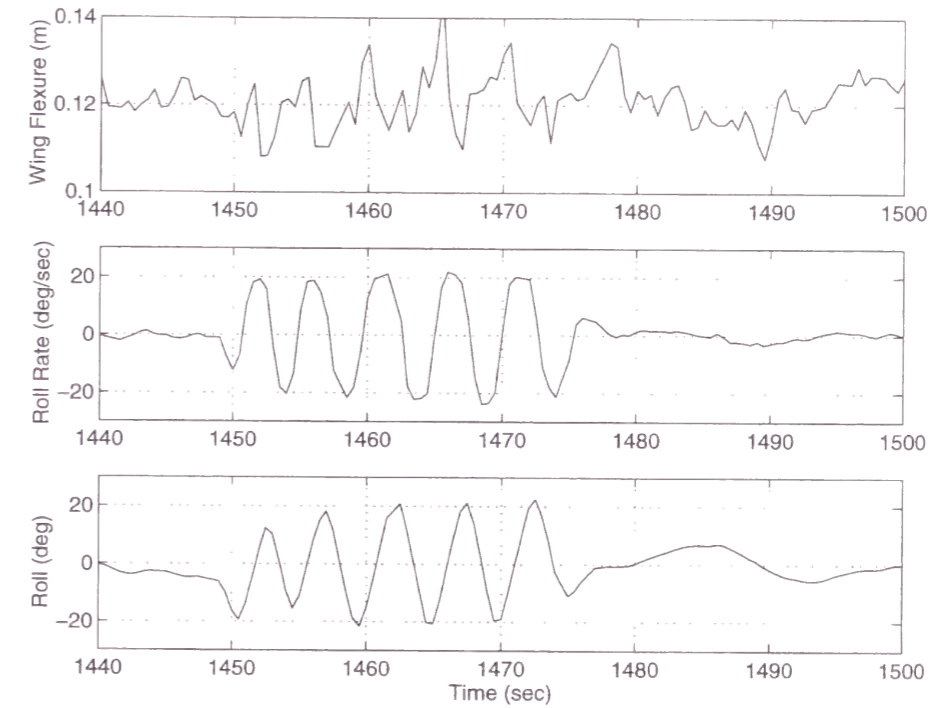


Fig.4-41 Change of wing flexure, roll, and roll rate during roll reversals

Chapter 5

Summary and Conclusions

5.1 Summary

In this thesis, we proposed a new criterion for the ambiguity resolution on-the-fly, and evaluated its performance using the real GPS measurement data of the geodetic surveys and flight experiments. Furthermore, we applied the OTF algorithm to the KGPS precise positioning and attitude determination of an aircraft, and showed the experimental results.

Conclusions (1)-(4) were obtained by the analyses of surveyed GPS data in the Izu-Islands area. These experiments were conducted in order to evaluate the accuracy of kinematic GPS. Although we used static data, the results of analyses would give supporting evidence for the accuracy of moving vehicles.

- (1) The horizontal positioning accuracy of kinematic GPS using the ionospheric-free observable was around 1.3cm (1σ) when the baseline length was shorter than 40km. The vertical positioning accuracy was up to 5cm for the same baselines because it is affected very much by the meteorological conditions. In order to improve the vertical positioning accuracy, detailed meteorological observations are necessary. Since the estimates of accuracy were obtained by the analyses of only one day's GPS data, the analyses of a greater number of data in various conditions will be necessary to obtain more reliable values.
- (2) The L1 ambiguity was correctly resolved with a baseline of up to 80km by using the OTF algorithm we proposed. It is noted that the experiments were conducted from 3p.m. to 3a.m. local time and the activity of the sun was intermediate. The

performance of OTF is much affected by the ionospheric propagation delay.

- (3) In the OTF algorithm, the test in measurement domain is mainly affected by both the ionospheric and tropospheric delay, while the test in positioning domain is affected by ionospheric delay. Therefore, if only the test in measurement domain was adopted, the correct ambiguity could not be resolved due to some severe meteorological conditions.
- (4) Crustal movement of a few centimeters level due to an earthquake was detected by the kinematic GPS. This result suggests the possibility of a real time monitoring of crustal movements in which the predicted precise ephemeris should be used.
Conclusions (5)-(8) were obtained by analyzing the GPS data of flight experiments conducted by NAL.
- (5) As a result of comparison between the KGPS trajectory calculated using double differenced observable and that using triple differenced observable, the positioning accuracy of the former trajectory was better than 10cm (RMS).
- (6) The KGPS trajectory of aircraft was compared with that calculated using the laser tracker. The RMS of position difference was 30cm, that is nearly equal to the accuracy of the tracker's range measurement. The KGPS is a very precise and useful technique for evaluating other kinds of positioning instruments such as the laser tracker and DGPS/INS navigation system.
- (7) The performance of the OTF algorithm was evaluated using the data of flight experiments where the distance from the reference site was shorter than 20km and the height did not exceed 800m. The test in positioning domain would be very effective in resolving the L1 ambiguity quickly and reliably. The ambiguity was correctly resolved in two epochs with better than 98% possibility even when only five satellites were observed. Furthermore, when six or more satellites were observed, the correct ambiguity was resolved almost instantaneously with better than 99.9% possibility.
- (8) In the experiment of attitude determination, the GPS receivers aboard always tracked more than four satellites and provided three axes attitude measurement in the normal flight operation (-5 to 15 degrees for pitch and -40 to 35 degrees for roll). The carrier phase ambiguities were correctly resolved within a few seconds. GPS-estimated

attitude agreed with the INS measurement at a level of 0.05 - 0.075 degrees (RMS). This value is consistent with the analytical prediction. The estimated wing flexure was 12 cm nominally and changed according to aircraft maneuvers. The lateral flexure of the fuselage could be detected during strong yaw maneuvers.

5.2 Conclusions and Future Prospects

The kinematic GPS is a technique useful in practice to provide very accurate position information without other kinds of equipment, and some examples of off-line applications were shown in this thesis. The dual frequency GPS receiver is better than a single frequency receiver because the latter has difficulty in resolving the ambiguity with baselines longer than 10km, and takes much time. In the aerial survey of the remote sensing such as SAR (Kimata, et. al., 1997), the baseline length easily exceeds 10 km. The dual frequency receiver can give the next best position solutions for long baselines by using the widelane observable. The positioning accuracy would be better than 10cm horizontally, and 30cm vertically with baselines up to 100km which are much more accurate than the pseudorange-position. Moreover, the L1 ambiguity could be resolved easily if the widelane ambiguity was known. The proposed OTF algorithm is suited for the dual frequency receivers, and effective for fairly long baseline applications.

The next step of this study on KGPS is to establish a real time kinematic GPS (RTK) system which can be useful not only for the precise positioning of vehicles but also for the agriculture and the construction industry. Though the RTK has been developed by some organizations (Floodge, et. al., 1994) or by some makers of GPS receivers (Topcon, 1994; Trimble, 1995), we have been developing the RTK for aircraft positioning using the OTF algorithm proposed above (Tsujii, et. al., 1996b). The RTK would also be applied to the aircraft navigation and A/L if its disadvantages concerning the integrity, continuity, and availability were overcome. Therefore, the real-time KGPS/INS hybrid system can be thought to be the next generation's navigation system following the DGPS/INS.

Attitude determination is one application of KGPS. The feasibility of a GPS attitude determination system was confirmed using the real data of flight experiments.

The algorithm developed here can be applied to all kinds of vehicles. Furthermore, such a system could be used to estimate the structural flexure as shown in this thesis. Therefore, if this system were used for a flexible structure like a space station, the structural flexure or deformation would be observed, as well as its attitude.

Especially, the GPS-based attitude determination system is of particular interest for near-Earth space applications such as Japan's non-manned space shuttle, HOPE, or several kinds of earth observation satellites because of the possibility of reducing the number of navigation and attitude sensors and increasing spacecraft autonomy. In fact, the GPS-based attitude determination system was aboard the U.S. Air Force RADCAL satellites, and flight tests were conducted showing that the precision was assessed to be at the level of 0.4 deg for pitch and roll, and 0.7 deg for yaw (Axlerad and Ward, 1996). However, in order to apply our algorithms to space applications, further studies on the satellite visibility and the reformulation of the algorithm in terms of EKF rather than the least squares method would be necessary.

References

- Abidin H. Z., D. E. Wells, and A. Kleusberg (1991): Multi-Monitor Station 'On the Fly' Ambiguity Resolution: Theory and Preliminary Results, Proceedings of DGPS'91, First International Symposium on Real Time Differential Applications of the Global Positioning System, 1, Sept. 16-20, 1991, Braunschweig, Federal Republic of Germany, pp44-56.
- Abidin H. Z. (1993): On the Construction of the Ambiguity Searching Space for On-the-Fly Ambiguity Resolution, Navigation, J. of the Institute of Navigation, **40**, No.3, pp321-338.
- Axelrad P. and L. M. Ward (1996): Spacecraft Attitude Estimation Using the Global Positioning System: Methodology and Results for RADCAL, J. of the Guidance, Control, and Dynamics, **19**, No.6, pp1201-1209.
- Bastos L. and H. Landau (1988): Fixing cycle slips in dual-frequency kinematic GPS-applications using Kalman filtering, manuscripta geodetica, **13**, pp249-256.
- Blewitt G. (1990): An Automatic Editing Algorithm for GPS Data, Geophysical Research Letters, **17**, No.3, pp199-202.
- Braasch S. (1996): Multipath Effects, in Global Positioning System Theory and Applications, Progress in Astronautics and Aeronautics 164, pp547-568.
- Cannon M. E. and H. Sun (1994): Assessment of a Non-dedicated GPS Receiver System for precise Airborne Attitude Determination, Proceedings of ION-94, Salt Lake City, Sept.20-23, pp645-654.
- Chen D. and G. Lachapelle (1994): A Comparison of the FASF and Least-Squares Search Algorithms for Ambiguity Resolution On-the-Fly, Proceedings of the International Symposium on Kinematic Systems in Geodesy, Geomatics and Navigation, Banff, August 30 - September 2, pp241-254.
- Cohen C. E. and B. W. Parkinson (1992): Aircraft applications of GPS-based attitude determination. Proceedings of ION GPS-92, Albuquerque, September 16-18, pp775-782.
- Cohen C. E., B. D. McNally, and B. W. Parkinson (1993): Flight Tests of Attitude Determination Using GPS Compared Against an Inertial Navigation Unit, Navigation, J. of the Institute of Navigation, **41**, No.1, pp83-97.

- El-Mowafy A., and K. P. Schwarz (1995): Epoch by Epoch Attitude Determination Using GPS Multi-Antenna System in Kinematic Mode, Proceedings of the International Symposium on Kinematic Systems in Geodesy, Geomatics and Navigation, Banff, August 30 - September 2, pp331-340.
- Flodge S. L., S. R. Deloach, B. Remondi, D. Lapucha, and R. A. Barker (1994): Real-Time on-the-Fly Kinematic GPS System Results, Navigation, J. of the Institute of Navigation, **41**, No.2, pp175-185.
- Ford T. L. and J. Neumann (1994): NovAtel's RT-20-A Real Time Floating Ambiguity Positioning System, Proceedings of ION GPS-94, Sept. 20-23, 1994, Salt Lake City, pp1067-1076.
- Harigae M., M. Murata, and T. Tsujii (1995): Flight Evaluation of the DGPS-INS Hybrid Navigation System for Category III Automatic Landing, Advances in the Astronautical Sciences, 91, AAS95-622, pp771-785.
- Harigae M., M. Murata, and T. Tsujii (1996): Orbit Determination of the Orbital Reentry Experiment (OREX) Spacecraft by GPS, Advances in the Astronautical Sciences, 93, AAS-96-179.
- Harigae M. (1997): Theoretical Accuracy Analysis and Flight Evaluation of DGPS/INS Hybrid Navigation System, Dr. thesis, Department of Aeronautics and Astronautics, University of Tokyo.
- Hatanaka Y. (1996a): Problem of real time GPS analysis, Proceedings of the Japan symposium on GPS (1996), Tsukuba City, July 17-19, pp71-74. (in Japanese)
- Hatanaka Y (1996b): A summary of GPS meteorology, Proceedings of the Japan symposium on GPS (1996), Tsukuba City, July 17-19, pp22-25. (in Japanese)
- Hatch R. (1991): Instantaneous Ambiguity Resolution, Proceedings of IAG International Symposium No.107 on Kinematic Systems in Geodesy, Surveying and Remote Sensing. New York: Springer Verlag, pp299-308.
- Hatch R. (1994): Comparison of Several AROF Kinematic Techniques, Proceedings of ION GPS-94, Sept. 20-23, 1994, Salt Lake City, pp363-370.
- Hofmann-Wellenhof B., H. Lichtenegger, and J. Collins (1992): GPS - Theory and Practice -, Springer-Verlag.
- Katayama T. (1983): Applied Kalman Filter, Asakura, Tokyo. (in Japanese)
- Kee C. and B. Parkinson (1995): Calibration of Multipath Errors on GPS Pseudorange Measurements, Proceedings of ION GPS-95, Sept. 12-15, 1995, Palm Springs, pp353-362.

- Kimata F., N. Fujii, Y. Yamaguchi, T. Okuda, R. Miyajima, K. Ogawa, S. Kobayashi, H. Nohmi, M. Murata, M. Miyawaki, M. Murata, M. Harigae, and T. Tsujii (1997): Japan Earth and Planetary Science Joint Meeting 1997, Nagoya City, March 35-28, pp310.
- Kleusberg A. (1986): Kinematic Relative Positioning Using GPS Code and Carrier Beat Phase Observations, Marine Geodesy, **10**, No.3, pp257-274
- Klobuchar J. A. (1996): Ionospheric Effects on GPS, in Global Positioning System Theory and Applications, Progress in Astronautics and Aeronautics 164, pp485-515.
- Knight D. (1994): A New Method of Instantaneous Ambiguity Resolution, Proceedings of ION GPS-94, Sept. 20-23, 1994, Salt Lake City, pp.707-716.
- Kusaba R., T. Tabei, T. Tsujii, and K. Matsushima (1997): Evaluation of GPS Kinematic Survey Using the KINGS and PNAV, Japan Earth and Planetary Science Joint Meeting 1997, Nagoya City, March 25-28, pp307.
- Lachapelle G., M. E. Cannon, and G. Lu (1992a): High-Precision GPS Navigation with Emphasis on Carrier-Phase Ambiguity Resolution, Marine Geodesy, **15**, pp253-269.
- Lachapelle G., M. E. Cannon, G. Lu (1992b): Ambiguity Resolution on the Fly -A Comparison of P Code and High Performance C/A Code Receiver Technologies, Proceedings of ION GPS-92, Albuquerque, September 16-18, pp1025-1032.
- Landau H. (1989): Precise Kinematic GPS Positioning, Bull. Geod., **63**, pp85-96.
- MacMillan C., G. Lachapelle, and G. Lu (1995): Dynamic GPS Attitude Performance Using INS/GPS Reference, Proceedings of ION GPS-95, Sept. 12-15, 1995, Palm Springs, pp675-682.
- Mader G., L. (1986): Dynamic positioning using GPS carrier phase measurements, Manuscripta Geodetica, **11**, pp272-277.
- Matsumoto S., H. Suzuki, T. Izumi, M. Harigae, T. Tsujii, K. Ishikawa, T. Ono, A. Itsukaichi, H. Maeda, H. Tomita, T. Miyano: System Design and Flight Experiment Results of the Pseudolite DGPS System for Automatic Landing Flight Experiment (ALFLEX), Proceedings of ION GPS-96, Sept. 17-20, 1996, Kansas City, pp87-94.
- MIT (Department of Earth, Atmospheric and Planetary Sciences) (1995): Documentation for the GAMIT GPS Analysis Software Release 9.40.
- Murata M. and M. Harigae (1992a) : The observations and Analysis of Selective Availability in GPS, Trans. Soc. of Instrument and Control Engineers, **28**, No.1, pp40-49. (in Japanese)

- Murata M., T. Tsujii, K. Matsushima, T. Ono, Y. Miyazawa, K. Ishikawa, T. Uchida, H. Hasegawa, S. Fukushima, H. Yokoyama, H. Tajima, H. Mineno, M. Ikeuchi, M. Harigae, H. Tomita (1992b): A GPS Surveying Method Applied to Approach/Landing Navigation Flight Experiments, *J. of the Geodetic Soc. Japan*, **38**, No.2, pp137-149.
- Murata M., T. Tsujii, and M. Harigae (1994): Flight Experiment Results for Aircraft Positioning with Carrier Phases, *Proceedings of ION GPS-94*, Sept. 20-23, 1994, Salt Lake City, pp1519-1526.
- Murata M., M. Harigae, and T. Tsujii (1996): Orbit Determination of the Orbital Reentry Experiment (OREX) Spacecraft by GPS, *Advances in the Astronautical Sciences*, 93, AAS-96-179.
- Nagoya University and Shizuoka University (1996): Horizontal displacement at Kozushima detected by GPS measurements in the period 1990-1995, *Rep. Coordinating Committee for Earthquake Prediction*, 56, pp298-300. (in Japanese)
- Newby S. and W. Corcoran (1995): What's New from NovAtel, *Proceedings of ION GPS-95*, Sept. 12-15, 1995, and Palm Springs, pp133-140.
- Ono T., N. Okada, T. Inagaki, H., Inokuchi, M. Harigae, T. Tsujii, T. Suito, Y. Suzaki, K. Murasawa: Development of the Laser Tracker and its Flight Evaluation Test, *Proceedings of the 34th Aircraft Symposium*, October 16-18, Tottori City, pp347-350. (in Japanese)
- Remondi B. W. (1985): Global Positioning System: Description and Use, *Bulletin Geodetique*, **59**, pp361-377.
- Remondi B. W. (1991): Pseudo-Kinematic GPS Results Using the Ambiguity Function Method, *Navigation, J. of the Institute of Navigation*, **38**, No.1, pp17-36.
- Seeber G. and G. Wübbena (1989): Kinematic Positioning with Carrier Phases and "On the Way" Ambiguity Solution, *Proceedings of 5th International Geodetic Symposium on Satellite Positioning*, Las Cruces, Vol.2 pp606-609.
- Seeber G. (1993): *Satellite Geodesy*, Walter de Gruyter.
- Spilker J. J. Jr. (1996a): Tropospheric Effects on GPS, in *Global Positioning System Theory and Applications*, *Progress in Astronautics and Aeronautics* 164, pp517-546.
- Spilker J. J. Jr. (1996b): GPS Navigation Data, in *Global Positioning System Theory and Applications*, *Progress in Astronautics and Aeronautics* 164, pp121-176.
- Sun H. (1994): Integration of INS with multiple GPS antennas for airborne applications, *Proceedings of ION GPS-94*, Sept. 20-23, 1994, Salt Lake City, pp1401-1409.

- Talbot N. C. (1991): High-Precision Real-Time GPS Positioning Concepts: Modeling and Results, *Navigation, J. of the Institute of Navigation*, **38**, No.2, pp147-161.
- Topcon (1994): Topcon GP-R1DY GPS Receiver Operating Manual, Topcon Document Number 600260, Revision A.
- Trimble (1995): Series 4000 Application Guide, Part Number 27249-00, Revision A.
- Tsuji H., Y. Hatanaka and S. Miyazaki (1996): Tremors! - Monitoring Crustal Deformation in Japan, *GPS World*, pp18-29, April.
- Uematsu H. and B. W. Parkinson (1994): Antenna Baseline and Line bias Estimation Using Pseudolites for GPS-Based Attitude Determination, *Proceedings of ION-94*, Salt Lake City, Sept.20-23, pp717-726.
- Van Graas, F. and M. Braash (1991): GPS Interferometric Attitude and Heading Determination: Initial Flight Test Results, *Navigation, J. of the Institute of Navigation*, **38**, No.4, pp297-316.
- Van Graas, F., D. W. Diggle, and R. M. Hueschen (1994): Interferometric GPS Flight Reference/Autoland System - Flight Test Results -, *Navigation, J. of the Institute of Navigation*, **41**, No.1, pp57-81.
- Wübbena G. (1989): The GPS adjustment software package GEONAP, concept and models. *Proceedings of 5th International Geodetic Symposium, Satellite Positioning*, 1, pp452-461.

List of Author's Papers Cited in This Thesis

- Tsujii T., M. Murata, T. Ono, and K. Ishikawa (1995a): Flight Evaluation of Differential GPS, *Trans. Soc. of Instrument and Control Engineers*, **31**, No.1, pp76-81. (in Japanese)
- Tsujii T., M. Murata, and M. Harigae (1997b): First Convergence Ambiguity Resolution On-the-Fly for Dual Frequency GPS Receivers and the Flight Evaluation, *Trans. Soc. of Instrument and Control Engineers*, **33**, No.8, pp743-751. (in Japanese)
- Tsujii T., M. Harigae, and M. Murata (1997c): The development of Kinematic GPS Software, KINGS, and its Application to Observations of the Crustal Movements, *J. of the Geodetic Soc. Japan*, **43**, No.2, pp91-105. (in Japanese)

Other Proceedings and Short Papers

- Tsujii T., M. Murata, T. Ono, K. Ishikawa, and Y. Miyazawa (1992): Flight Experiments of Differential GPS, *Proceedings of the 31st SICE Annual Conference*, July 22-24, Kumamoto City, pp789-790. (in Japanese)
- Tsujii T. and M. Murata (1993a): A Flight Experiment of Kinematic GPS, *Proceedings of the 37th Space Science and Technology Conference*, October 27-29, Kitakyushu City, pp371-372. (in Japanese)
- Tsujii T., M. Murata, T. Ono, and K. Ishikawa (1993b): Flight Evaluation of Differential GPS for Terminal Area Operations, *Technical Report of National Aerospace Laboratory*, TR-1210, pp1-24. (in Japanese)
- Tsujii T., M. Murata, and M. Harigae (1994a): GPS Carrier Phase Positioning and OTF algorithms - Flight Test Results -: *Proceedings of the Japan symposium on GPS (1994)*, December 15-16, Tokyo, pp85-90.
- Tsujii T., M. Murata, and M. Harigae (1994b): Preliminary Results of Ambiguity Resolution On-the-Fly, *Proceedings of the 32nd Aircraft Symposium*, October 5-7, Kitakyushu City, pp109-112.
- Tsujii T., M. Murata, M. Harigae (1995b): Kinematic GPS Flight Tests - Evaluation of OTF Algorithm, *Proceedings of the 34th SICE Annual Conference*, July 26-28, 1995, Sapporo, pp547-548. (in Japanese)
- Tsujii T., M. Murata, and M. Harigae (1995c): Airborne Kinematic Attitude Determination Using GPS Phase Interferometry, *Proceedings of the 33rd Aircraft Symposium*, November 8-11, Hiroshima City, pp595-598.

Tsujii T., M. Murata, and M. Harigae (1996a): Flight Tests of Attitude Determination Using GPS, *Proceedings of the 40th Space Science and Technology Conference*, October 28-30, Morioka City, pp49-50. (in Japanese)

Tsujii T., M. Harigae, and M. Murata (1996b): Development of RTK (Real Time Kinematic GPS) system, *13th Guidance and Control symposium*, Tokyo, Nov.7-8, pp39-46. (in Japanese)

Tsujii T., M. Murata, and M. Harigae (1996c): Airborne Kinematic Attitude Determination Using GPS Phase Interferometry, *J. Japan Soc. Aero. Space Sci.*, **44**, No.515, pp741-743. (in Japanese)

Tsujii T., M. Murata, and M. Harigae (1997a): Airborne Kinematic Attitude Determination Using GPS Phase Interferometry, *7th AAS/AIAA Space Flight Mechanics Meeting*, February 10-12, Huntsville, Alabama, AAS97-168, pp1-12.